Auger Electron Spectroscopy on Cylindrical Single Crystals

by James Stewart Arlow.

Submitted to the University of Warwick in June 1985 for the degree of Ph.D.

The research reported in this thesis was performed at the Physics Department,

The University of Warwick,

Coventry,

England.

DEDICATION

I would like to dedicate this work to my parents, grandparents, friends and relations, all of whom have given me much support throughout the course of this work.

ACKNOWLEDGEMENTS

I take great pleasure in thanking all those who have helped with this research and ask the forgiveness of all those who have helped who are not specifically mentioned here.

I would particulary like to thank Adrian and Roger of the University of Warwick electronics workshop for helping me to rebuild an Auger spectrometer, and Stan, Pete and Rob, the Surface Physics techincians for excellent technical support. I would also like to thank Les Keeling for many useful discussions about surface physics.

Without the help and support of my friends, this work would have been very much harder, and I would particularly like to thank Alan Toms and his family, Sue Burkitt, Les and Liz Keeling and Andrew Visser.

I would like to acknoledge the support of S.E.R.C. and of the University of Warwick.

Finally, I would like to thank Phil Woodruff (who has helped the most with this work), my research supervisor, for many very interesting discussions, and also for teaching me about surface physics.

"In the beginner's mind there are many possibilities, but in the expert's there are few."

Shunryu Suzuki

Zen Mind, Beginner's Mind

PUBLICATIONS

CHAPTER 5

The work presented in chapter 5 has been accepted for publication in Surface Science.

CHAPTERS 5, 6 AND 7

The work presented in these chapters has been submitted for presentation at ECOSS7.

Table of Contents

CHAPTER 1: INTRODUCTION
(1.1) Introduction p.1

CHAPTER 2: THEORETICAL BACKGROUND
(2.1) The Auger Effect p.1
(2.2) The nomenclature of Auger transitions p.10
(2.3) The energies of Auger electrons p.10
(2.4) Experimental Auger electron spectroscopy (AES) p.11
(2.5) Excitation p.12
(2.6) Electron energy analysers p.13
(2.7) The retarding field analyser (RFA) p.13
(2.8) The Cylindrical mirror analyser (CMA) p.18
(2.9) Quantitative AES p.22
(2.10) Adsorption on surfaces. p.23
(2.11) Physisorption p.23
(2.12) Chemisorption p.24
(2.13) The influence of surface crystallography on physisorption and chemisorption. . . . p.26
(2.14) The effect of adsorbate/adsorbate interactions. p.26
(2.15) Mechanisms for chemisorption and adsorption kinetics p.26
(2.16) The kinetics of reactions between two gases over metal surfaces p.28
(2.17) Segregation p.29

CHAPTER 3: THE AUGER SPECTROMETER
(3.1) Introduction to chapter 3. . . . . p.32
(3.2) The ultra high vacuum (UHV) chamber p.32
(3.3) The HCMA and ramp generator p.33
(3.4) The detection system p.35
(3.5) The electron gun and power supply p.35
(3.6) The physical imaging system. p.36
(3.7) The argon ion gun. p.37
(3.8) The cylindrical single crystals p.37
(3.9) Sample heating p.38
(3.10) The sample manipulator p.38
(3.11) Sample holders for cylindrical crystals. p.39
(3.12) The computer interface. p.43
(3.13) The software. p.46
(3.14) Digital smoothing filters p.47

CHAPTER 4: SURFACE CRYSTALLOGRAPHY OF THE CYLINDRICAL SINGLE CRYSTALS AND PRELIMINARY EXPERIMENTS
(4.1) Introduction. p.53

(4.2) Cylindrical single crystals p.53
(4.3) The <110> axis cylinder p.54
(4.4) Vicinal surfaces p.56
(4.5) The stability of vicinal surfaces p.56
(4.6) Nomenclature of vicinal surfaces. p.58
(4.7) Crystallographic incident beam effects in AES p.61
(4.8) Preliminary studies of cylindrical single crystal surfaces. p.64
(4.8.1) The thermal decomposition of carbon monoxide on the vicinal surfaces of nickel: Previous work. p.64
(4.8.2) CO decomposition on Ni: Experimental procedure, results and discussion p.66
(4.8.3) Carbon and sulphur segregation in nickel: Previous work. p.68
(4.8.4) Carbon segregation in nickel: Experimental procedure p.73
(4.8.5) Results and discussion p.75
(4.8.6) Conclusions p.82

CHAPTER 5: THE INTERACTION OF OXYGEN AND NITROUS OXIDE WITH COPPER SINGLE CRYSTAL PLANES
(5.1) Introduction to chapter 5. . . . . p.87
(5.2) Oxygen adsorption on copper: Previous work. p.87
(5.3) Oxygen adsorption on Cu(111) p.88
(5.4) Oxygen adsorption on Cu(110) p.89
(5.5) Oxygen adsorption on Cu(100) p.91
(5.6) Oxygen adsorption on copper vicinal surfaces. p.93
(5.7) Previous work on oxygen adsorption on the copper cylindrical single crystal p.95
(5.8) The diffusion free model. p.97
(5.9) The fast diffusion model. p.100
(5.10) Oxygen adsorption on copper cylindrical single crystals: Experimental procedure. p.101
(5.11) Results and discussion p.103
(5.12) The decomposition of nitrous oxide on copper surfaces: Previous work p.109
(5.13) Nitrous oxide adsorption on Cu(111) p.110
(5.14) Nitrous oxide adsorption on Cu(110) p.111
(5.15) Nitrous oxide adsorption on Cu(100) p.111
(5.16) Nitrous oxide adsorption on copper: Experimental procedure p.112
(5.17) Results and discussion p.112

CHAPTER 6: THE OXIDATION OF HYDROGEN AND CARBON MONOXIDE BY OXYGEN CHEMISORBED ON COPPER
(6.1) Introduction to chapter 6. . . . . p.125
(6.2) CO adsorption on copper surfaces p.125
(6.3) Oxygen adsorption on copper: The thermal stability of chemisorbed oxygen films. . p.127
(6.4) The oxidation of carbon monoxide by oxygen chemisorbed on copper single crystal surfaces. p.128
(6.5) The oxidation of CO by oxygen chemisorbed on Cu(111) p.129
(6.6) The oxidation of CO by oxygen chemisorbed on Cu(110) p.130
(6.7) The oxidation of CO by oxygen chemisorbed on Cu(100) p.131
(6.8) CO oxidation by oxygen adsorbed on copper single crystal planes: Experimental procedure. p.132

(6.9) Results and discussion p.133
(6.10) The oxidation of CO in a CO/oxygen gas mixture over copper single crystal surfaces. p.142
(6.11) Results and discussion p.149
(6.12) The oxidation of hydrogen by oxygen chemisorbed on copper surfaces p.156
(6.13) Hydrogen adsorption on copper surfaces. p.156
(6.14) The oxidation of hydrogen by oxygen chemisorbed on Cu(110). p.157
(6.15) The oxidation of hydrogen by oxygen chemisorbed on copper surfaces: Experimental procedure. p.158
(6.16) Results and discussion p.159

CHAPTER 7: FINAL CONCLUSIONS AND FURTHER WORK
(7.1) Final Conclusions p.168
(7.2) Further work p.169

APPENDIX: UNITS COMMONLY USED IN SURFACE PHYSICS

FIGURES

(2.1) The Auger effect. p.7
(2.2) The relative probabilities of Auger electron emission and X-ray emission. p.9
(2.3) Typical spectra run on the apparatus p.13
(2.4) LEED/Auger optics p.16
(2.5) The HCMA. p.19
(2.6) Chemisorption and physisorption potentials p.25

(3.1) The apparatus p.34
(3.2) The effects of eccentric sample rotation p.40
(3.3) A sample manipulator for cylindrical single crystals p.42
(3.4) Sample holders for cylindrical single crystals. p.44
(3.5) Diagram of the Auger spectrometer electronics p.45
(3.6) Typical Auger spectra smoothed by an extended Savitsky/Golay digital smoothing filter. p.49

(4.1) The <110> axis cylinder. p.55
(4.2) Vicinal planes generated by progressive misorientations of 5° from the (001) plane. . p.59
(4.3) Crystallographic anisotropy in the sample current p.62
(4.4) The kinetics of carbon segregation to Ni(001) p.76
(4.5) The anisotropy in the segregation of carbon to nickel crystal planes in the <110> zone p.79
(4.6) The anisotropy in the segregation of sulphur to nickel planes in the <110> zone . . . p.81

(5.1) The anisotropy in the dissociative adsorption of oxygen on the copper cylinder . . p.104

(5.2) The kinetics of oxygen adsorption on Cu(001), (111), (110) and (113) p.105
(5.3) A comparison of the predictions of the fast diffusion and the diffusion free models with the experimental data. p.107
(5.4) The anisotropy in the adsorption of nitrous oxide on the copper cylinder. p.113
(5.5) The kinetics of nitrous oxide adsorption on Cu(001), (111), (110) and (113) and the predictions of the 'work function' model. p.114

(6.1) The crystallographic anisotropy in the reduction of the oxygen saturated copper cylinder by CO at 570, 610, and 700K . . . . . p.134..136
(6.2) The kinetics of the reduction of the chemisorbed oxygen films on the copper cylinder by CO. p.139
(6.3) Smoothed and differentiated experimental data. p.145
(6.4) The oxidation of CO in a CO/oxygen gas mixture over copper surfaces p.150
(6.5) A prediction of the rate of the CO oxidation reaction on different crystal planes. p.153
(6.6) The variation in the 'steady state' oxygen coverage with the ratio of oxygen to CO in the gas mixture p.155
(6.7) The anisotropy in the reduction of the copper cylinder by hydrogen at 570 and 630K. p.160
(6.8) The kinetics of the hydrogen oxidation reaction. p.162

(7.1) The anisotropy in the dissociative adsorption of chloroform with copper single crystal planes p.170

TABLES

(5.1) Values of the initial sticking factor for oxygen on copper low index planes p.99

(6.1) The coefficients for equation 6.9 which describes the reduction of oxygen chemisorbed on copper by CO, and the 'K' values for the oxygen adsorption equations 6.15 and 6.16 . p.146

Chapter 1

INTRODUCTION

(1.1) Introduction.

Surface defects have, within recent years, come to be identified with the 'active sites' first proposed by Taylor[1] in his theory of catalysis. There have been many investigations into the role of surface defects such as steps, kinks and dislocations in surface reactivity, and in many instances such defects are indeed found to be associated with an enhanced reactivity. The reader's attention is directed to references 2 and 3 in which some of this work has been reviewed. Surface defects are by no means the only source of the reactivity of metal surfaces however, and the low index planes of a crystal each exhibit a reactivity which is often found to be markedly dependent on the surface orientation.

The aim of this work is to investigate the effect of surface crystallography, and in particular the effect of a certain type of surface defect, the monatomic step, on the chemical reactivity of surfaces. There are basically two approaches to this problem. The most common approach is to investigate a particular reaction on several different samples all with different surface orientations. An alternative approach (the one used in this work) is to investigate a given chemical reaction on a sample which exhibits a range of surface crystallographies. This latter approach has many advantages and some disadvantages as will become apparent in the work which follows.

For this investigation, copper and nickel cylindrical single crystals were used which had been cut with a <110> axis. Thus, all three low index planes (001), (111) and (110) were made available as well as the (113) face and a continuum of vicinal surfaces. A unique property of <110> axis cylindrical single crystals of face centered cubic metals is that all step ledges run parallel to the cylinder axis, and this means that for a perfect crystal, the kink density is zero. Furthermore, the step density varies in a linear manner between the planes (113) and (001), (113) and (111) and between (110) and (111). This

allows the investigation of the effect of monatomic steps, and in particular, variations in step density, on the chemical reactivity of surfaces. Such a sample also allows rather accurate comparisons to be made of the properties of the various low index planes.

The analytic technique used in this work was Auger electron spectroscopy which allowed accurate determination of surface coverages in the sub-monolayer regime with good spatial resolution. The reactions studied are carbon and sulphur segregation in nickel (chapter 4), and the redox properties of the copper cylinder (chapters 5 and 6). In chapter 5 oxidation experiments on the copper cylinder are described in which two different oxidizing agents, oxygen and N_2O, are used, and the reactions are compared and contrasted. The oxygen adsorption experiments also provide a basis for the re-evaluation of two models proposed by Armitage[4] describing the kinetics of adsorption on all the surfaces provided by the <110> axis copper cylinder. A simple model describing the crystallographic variation of the initial reaction probability of N_2O decomposition on copper surfaces is also described in this chapter, and it is found that the initial reaction probability shows a dependence on step density which is non-linear.

In chapter 6, the reduction of chemisorbed oxygen films on copper single crystal surfaces is studied using two different reducing agents, CO and hydrogen, and it is shown that even such classically non-plane-specific reactions as these do, in fact, exhibit an observable crystallographic anisotropy. Also in chapter 6, the results of the oxygen adsorption and CO oxidation experiments are extrapolated in a theoretical investigation of the oxidation of CO in a CO/oxygen gas mixture over copper single crystal planes. The theoretical treatment allows the calculation of the rate of CO oxidation, and the stationary oxygen coverage in the 'steady state' reaction where the rate of reduction of the surface is exactly equal to it's rate of oxidation. In the final chapter, some preliminary data are presented on the reaction of chloroform with copper single crystal

allows the investigation of the effect of monatomic steps, and in particular, variations in step density, on the chemical reactivity of surfaces. Such a sample also allows rather accurate comparisons to be made of the properties of the various low index planes.

The analytic technique used in this work was Auger electron spectroscopy which allowed accurate determination of surface coverages in the sub-monolayer regime with good spatial resolution. The reactions studied are carbon and sulphur segregation in nickel (chapter 4), and the redox properties of the copper cylinder (chapters 5 and 6). In chapter 5 oxidation experiments on the copper cylinder are described in which two different oxidizing agents, oxygen and N_2O, are used, and the reactions are compared and contrasted. The oxygen adsorption experiments also provide a basis for the re-evaluation of two models proposed by Armitage[4] describing the kinetics of adsorption on all the surfaces provided by the <110> axis copper cylinder. A simple model describing the crystallographic variation of the initial reaction probability of N_2O decomposition on copper surfaces is also described in this chapter, and it is found that the initial reaction probability shows a dependence on step density which is non-linear.

In chapter 6, the reduction of chemisorbed oxygen films on copper single crystal surfaces is studied using two different reducing agents, CO and hydrogen, and it is shown that even such classically non-plane-specific reactions as these do, in fact, exhibit an observable crystallographic anisotropy. Also in chapter 6, the results of the oxygen adsorption and CO oxidation experiments are extrapolated in a theoretical investigation of the oxidation of CO in a CO/oxygen gas mixture over copper single crystal planes. The theoretical treatment allows the calculation of the rate of CO oxidation, and the stationary oxygen coverage in the 'steady state' reaction where the rate of reduction of the surface is exactly equal to it's rate of oxidation. In the final chapter, some preliminary data are presented on the reaction of chloroform with copper single crystal

planes, a reaction which also is found to exhibit a slight crystallographic anisotropy, and the previous work is summarized.

Chapter 1..... References

(1) Taylor H.S., *Proc. Roy. Soc.* A (1925) 108 p.105.

(2) Rhead G.E., *Surf. Sci.* 68 p.20-38 (1977); a review article on surface defects.

(3) Wagner H., Springer Tracts in Modern Physics vol. 85, Solid Surface Physics, Springer-Verlag Berlin, Hiedelberg, New York, (1979).

(4) Armitage A.F., Ph.d Thesis, the University of Warwick, 1982.

Chapter 2

THEORETICAL BACKGROUND

Chapter 2..... Contents

(2.1) The Auger Effect.

(2.2) The nomenclature of Auger transitions.

(2.3) The energies of Auger electrons.

(2.4) Experimental Auger electron spectroscopy (AES).

(2.5) Excitation.

(2.6) Electron energy analysers.

(2.7) The retarding field analyser (RFA).

(2.8) The Cylindrical mirror analyser (CMA).

(2.9) Quantitative AES.

(2.10) Adsorption on surfaces.

(2.11) Physisorption.

(2.12) Chemisorption.

(2.13) The influence of surface crystallography on physisorption and chemisorption.

(2.14) The effect of adsorbate/adsorbate interactions.

(2.15) Mechanisms for chemisorption and adsorption kinetics.

(2.16) The kinetics of reactions between two gases over metal surfaces.

(2.17) Segregation.

(2.1) The Auger Effect.

The Auger effect, discovered by Pierre Auger[1] in 1925, occurs when an atom is ionized in an inner shell and the excited species so produced decays by the emission of an electron. Fig. 2.1 shows the formation of a core hole by incident ionizing energy and its subsequent decay by one of two competing processes ; Auger emission or X-ray fluorescence.

Both phenomena may be explained in terms of an internal rearrangement of electrons within the atom[2]. An electron of higher energy makes a downward transition to fill the core hole (the 'down' electron) and imparts its excess kinetic energy to either an X-ray photon (X-ray fluorescence) or via a Coulombic interaction to an electron of similar or higher energy (the 'up' electron) which is ejected from the atom as an Auger electron. It should perhaps be noted by the reader that although the 'up' and 'down' electrons in the Auger process have been distinguished for the sake of this discussion, in reality both electrons are indistinguishable as they enter symmetrically into the quantum mechanical description of the process. It can be seen that for a K shell core hole of energy E_K and for a 'down' electron of energy E_{L_1} that the X-ray photon emitted during X-ray fluorescence will have an energy given by:

$$h\nu = E_K - E_{L_1} \qquad (2.1)$$

The energy of the Auger electron however, depends on the energy of the initial state core hole, E_K, the energy of the 'down' electron, E_{L_1}, and the energy of the 'up' electron $E_{L_{2,3}}$. Thus, if the kinetic energy of the emitted Auger electron is $E_{KL_1,L_{2,3}}$ then it can be seen from conservation of energy that

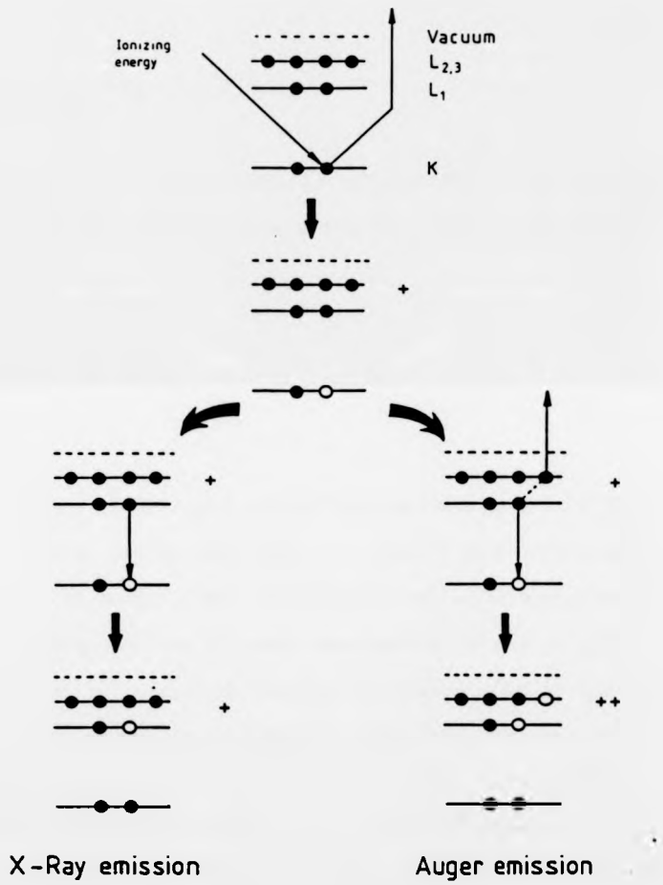

Fig. 2.1 This figure shows the formation of an atomic core-hole and it's subsequent decay by either X-ray emission (XRE) or Auger electron emission. In the case of X-ray emission, an electron from a higher energy level makes a downward transition to fill the core-hole, and in the process emits an X-ray photon. In the case of Auger electron emission, however, the decay is radiationless and the electron from the higher energy level imparts it's excess energy to another electron which is ejected from the atom as an Auger electron.

$$E_{KL_1,L_{2,3}} = E_K - E_{L_1} - E_{L_{2,3}} \quad (2.2)$$

where $E_{L_{2,3}}$ is the ionization potential of an atom which is already ionized in the inner shell, K. Conservation of energy also tells us that only those transitions which obey the inequality

$$E_{L_{2,3}} \leq E_K - E_{L_1} \quad (2.3)$$

will be allowed.

As the energy of the Auger electron is observed to be a function of atomic binding energies only, then it can be seen that each element must have a unique set of possible Auger transitions (a unique Auger spectrum) as no two elements have the same set of atomic binding energies. Thus, an Auger spectrum can be used as a 'fingerprint' by which a given element may be identified. The use of electron excited AES to identify surface impurities was first suggested by Lander[3] in 1953. X-ray fluorescence and Auger emission are the two competing de-excitation processes after the formation of an initial state core hole and fig. 2.2 shows the relative probabilities for de-excitation after the formation of a K shell core hole as a function of atomic number for both processes. It can be seen that for elements with atomic number less than about 25, that Auger emission is the dominant process, and this is also true for core holes in higher atomic levels. X-ray fluorescence spectroscopy is also a very valuable tool for elemental analysis, and because of it's inherently higher signal to background ratio exhibits a sensitivity similar to Auger electron spectroscopy even for light elements. X-ray emission spectroscopy (XRE) does not however exhibit the high degree of surface sensitivity exhibited by AES as

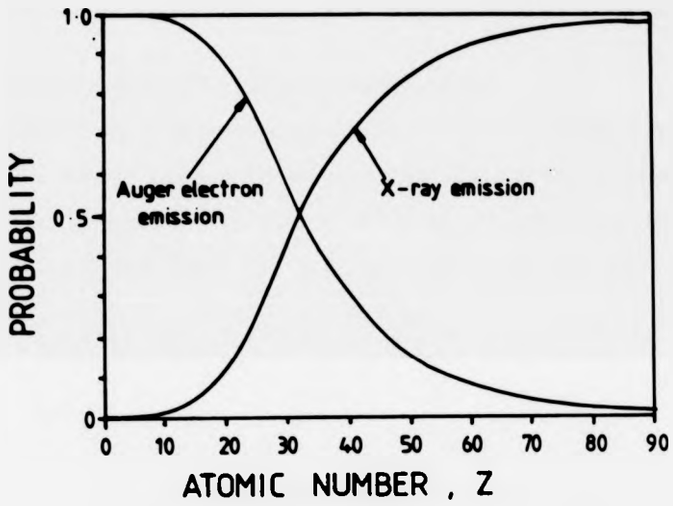

Fig. 2.2 This figure shows the relative probabilities of Auger electron and X-ray photon emission as a function of atomic number, Z.

The probability of photon emission (the fluorescence yeild, ω) has been calculated from[17]:

$$\omega = (1 + aZ^{-4})^{-1}$$

Where $a=1.12\times10^{6}$ for a K-shell core hole.

The probability of Auger emission is given by $(1-\omega)$.

Although the probability of X-ray emission is seen to be very small compared to the probability of Auger emission for light elements (Z<25), a consideration of signal to background ratios in X-ray and Auger emission spectroscopies clearly shows that the two techniques actually have very similar sensitivities.

the escape depth of the emitted X-rays is much larger than that of low energy electrons.

(2.2) The nomenclature of Auger transitions.

An Auger emission process involves at least three energy levels W,X and Y which may be used to specify the transition unambiguously. W is the energy level of the initial state core hole, X is the energy level from which the down electron originates and Y is the energy level from which the up electron is emitted. An Auger transition may thus be denoted by

$$W_pX_qY_r \tag{2.4}$$

where p,q and r denote sub shells within the atomic energy levels W,X and Y. This notation has already been used in equations 2.2 and 2.3. If X or Y is in the conduction band of a metallic sample, then the convention is to use the symbol V for valence band.
All Auger electrons resulting from a primary vacancy in the K shell are known as K Auger electrons, and by grouping together processes involving final vacancies in subshells of X and Y, then it becomes possible to refer to the KLL or KLM Auger spectrum for example.

(2.3) The energies of Auger electrons.

Chung and Jenkins[4] have derived an empirical approximation to the energy of an Auger transition E_{abc} in an element of atomic number Z.

$$E_{abc}(Z)=E(Z)-0.5[E_b(Z)+E_b(Z+1)]-0.5[E_c(Z)+E_c(Z+1)] \tag{2.5}$$

The $E_i(Z)$ terms denote the binding energies of the ith levels and the $0.5[E_i(Z)+E_i(Z+1)]$ terms take into account the increase in effective nuclear charge on formation of the initial state core hole.

The energy of an Auger transition may be more correctly expressed in terms of the binding energies of the initial state levels E_A,E_B and E_C, the interaction energy of the two final state holes f(BC:x) (where x denotes the final state) and the intra and extra atomic relaxation energies $R_{IN}x$ and $R_{EX}x$. These two relaxation energies arise from the inward collapse of the outer electrons towards the core on the formation of the core hole, and this leads to an increased Coulombic interaction between the core and the valence electrons. The intra atomic relaxation energy arises from the relaxation of electrons within the atom, whilst the extra atomic relaxation energy arises from the relaxation of electrons originating from other atoms but which are in the vicinity of the atom in question. The relationship between the Auger energy and these parameters is expressed in equation 2.6

$$E_{ABC}=E_A-E_B-E_C-f(BC:x)+R_{IN}x+R_{EX}x \qquad (2.6)$$

(2.4) Experimental Auger electron spectroscopy (AES).

Two initial requirements for experimental AES are :

(1) Some form of excitation energy to form the initial core hole.

(2) Some form of electron energy analyser to energy analyse the backscattered electrons.

(2.5) Excitation.

The initial excitation of the system may be accomplished by beams of ions, photons or electrons incident on the sample. Electron beams are in most common usage as they can be easily generated in well focussed high intensity beams in just the right energy range for AES. A main disadvantage of electron beams is that focussed high intensity beams, which may be desirable for high spatial resolution, can cause electron beam damage to the surface overlayer. Also, electron beams give a rather small signal to background ratio as inelastic interactions generate a large background of secondary electrons.

Fig. 2.3 shows a typical secondary electron spectrum run on the Auger spectrometer used in the current work. The x-ordinate is the electron energy in eV and the y-ordinate is E.N(E) where E is the spectrometer pass energy and N(E) is the number of electrons detected at that pass energy.

Obviously, there is a great deal of information contained in the secondary electrons, and for convenience, the secondaries may be classified as follows.

1) TRUE SECONDARIES

True secondaries include the Auger electrons, but by far the greatest number of true secondaries are found at low energies in the 'slow' peak ; a smooth hump in the spectrum comprising of electrons which exhibit a continuum of energies over a range. These 'slow' electrons arise primarily from plasmon creation processes or electron/hole pair production when a true secondary undergoes an energy loss. The originally well defined energy of the true secondary becomes distributed in a random manner amongst many electrons, and this randomizing process continues until the electrons have insufficient energy interact further. This results in a cascade of low energy electrons which exhibit a finite continuum of energies. As far as the Auger spectroscopist is concerned, the information content of these

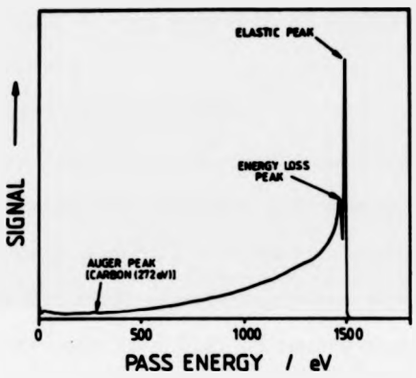

(a)

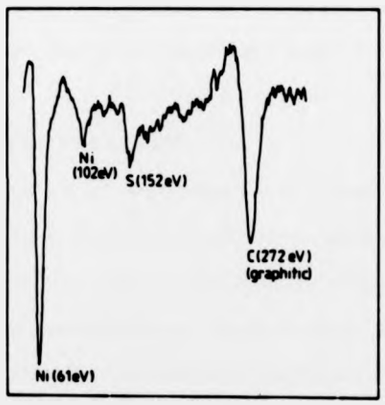

(b)

Fig. 2.3 This figure shows *(a)* a typical secondary electron spectrum and *(b)* a typical derivative mode Auger spectrum run on the apparatus used in this investigation.

slow electrons is zero, and they are the cause of the low signal to background ratios found in AES as they form a large background on which the small Auger peaks are superimposed.

2) INELASTICALLY SCATTERED ELECTRONS

Inelastically scattered electrons are generally found at higher energies and are those electrons which have been back-scattered from the surface after undergoing some sort of quantized energy loss. Energy losses may occur to create molecular vibrational and electronic excitations in the adsorbate and plasmon and phonon excitations in the adsorbent. Fig. 2.3 clearly shows a plasmon energy loss peak in nickel which is situated about 20eV below the elastic peak. Electron energy loss spectroscopy, (EELS), which is the spectroscopy of these inelastically backscattered electrons, is an important tool in the investigation of adsorbate-adsorbent bonding.

3) ELASTICALLY SCATTERED ELECTRONS

The elastically scattered electrons are those electrons which have been backscattered without undergoing any energy losses, and in the secondary electron spectrum they form a huge spike at the primary beam energy. If the surface exhibits order over a range comparable to the coherence width of the incident electron beam, then the elastically backscattered electrons, which have all undergone Bragg reflections from the first few atomic layers, may be made (with the aid of suitable optics) to form an electron diffraction pattern. This technique is known as low energy electron diffraction (LEED) and is perhaps the most important technique in surface science for the elucidation of surface crystallography as the diffraction pattern observed is the image of the surface net in wavevector (k) space.

(2.6) Electron energy analysers.

Many different electron energy analysers are in common usage and a useful review of the more common types may be found in Sevier[5]. Only two types of electron energy analyser will be discussed here, the retarding field analyser (RFA)[6], and the hemi-cylindrical mirror analyser (HCMA) which was used in the current work. The RFA will be discussed in some detail as it is still the most common electron energy analyser used for AES as it has the advantage that it may also be used for LEED.

(2.7) The retarding field analyser (RFA).

A typical set of LEED/Auger optics is shown schematically in Fig. 2.4. The optics consist of three concentric grids (or four if higher resolution is required) and a fluorescent screen. Generally, the primary electron beam will be generated by a low energy electron gun which will be situated so as to pass the beam across the face of the grids to strike the sample at grazing incidence, or, alternatively, to pass the beam along the axis of the grids through an earthed drift tube (see Fig. 2.4). The beam will then strike a grounded sample positioned accurately at the centre of curvature of the grids. Grazing incidence is generally preferred as this increases the sensitivity. Electrons from the grounded sample then travel radially outwards in the field free region between the sample and the first of the grids which is also grounded. The phosphor screen is biased a few hundred volts positive with respect to earth in order to act as an electron collector, and the second and third grids are connected to a ramp generator which supplies a ramp voltage, V. An isolating transformer is used to impress a small modulating voltage $r\sin(\omega t)$ on this ramp. If the optics also have a fourth grid , then this is usually tied to earth in order to prevent A.C. coupling between the collector and grids two and three.

(2.6) Electron energy analysers.

Many different electron energy analysers are in common usage and a useful review of the more common types may be found in Sevier[5]. Only two types of electron energy analyser will be discussed here, the retarding field analyser (RFA)[6], and the hemi-cylindrical mirror analyser (HCMA) which was used in the current work. The RFA will be discussed in some detail as it is still the most common electron energy analyser used for AES as it has the advantage that it may also be used for LEED.

(2.7) The retarding field analyser (RFA).

A typical set of LEED/Auger optics is shown schematically in Fig. 2.4. The optics consist of three concentric grids (or four if higher resolution is required) and a fluorescent screen. Generally, the primary electron beam will be generated by a low energy electron gun which will be situated so as to pass the beam across the face of the grids to strike the sample at grazing incidence, or, alternatively, to pass the beam along the axis of the grids through an earthed drift tube (see Fig. 2.4). The beam will then strike a grounded sample positioned accurately at the centre of curvature of the grids. Grazing incidence is generally preferred as this increases the sensitivity. Electrons from the grounded sample then travel radially outwards in the field free region between the sample and the first of the grids which is also grounded. The phosphor screen is biased a few hundred volts positive with respect to earth in order to act as an electron collector, and the second and third grids are connected to a ramp generator which supplies a ramp voltage, V. An isolating transformer is used to impress a small modulating voltage $r\sin(\omega t)$ on this ramp. If the optics also have a fourth grid , then this is usually tied to earth in order to prevent A.C. coupling between the collector and grids two and three.

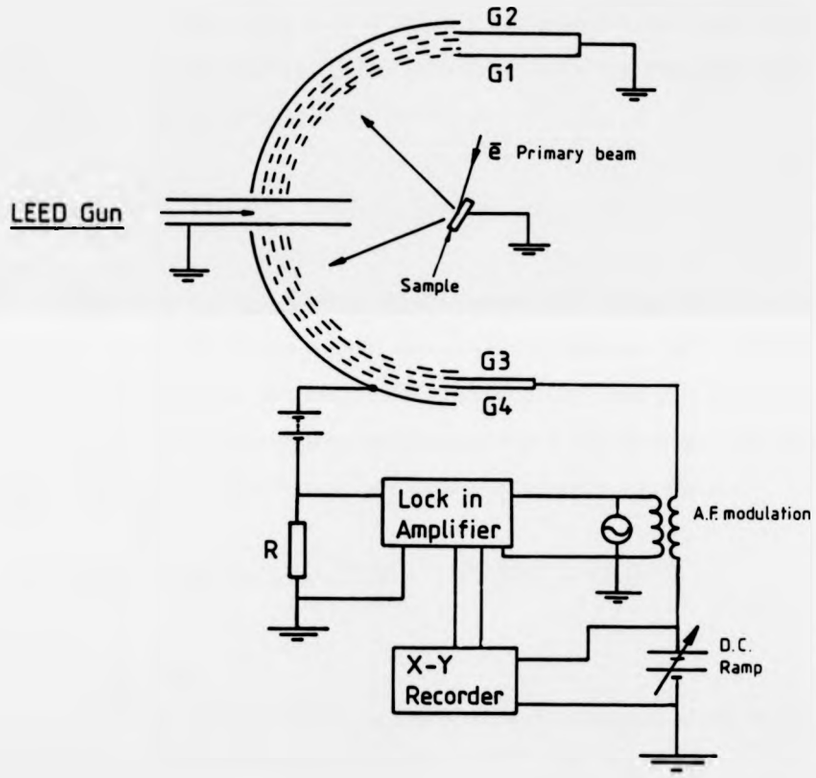

Fig. 2.4 This is a schematic of a typical retarding field analyser which may be used for either LEED or Auger. In Auger mode, the analyser collects all electrons with energy greater than eV, where V is the retarding potential applied to G3 and G4.

If the retarding voltage is V, and the charge on the electron is e, then only those electrons with energy greater than eV will be able to overcome the potential barrier generated by the second and third grids and reach the collector. Thus, the current at the collector is given by :

$$I(V) \propto \int_{E}^{E_{max}} N(E')dE' \tag{2.7}$$

Where N(E') is the number of electrons with energy E'. It can be seen that in order to acquire the energy distribution of the electrons N(E') from I(V), the signal at the collector must be differentiated. Fortunately, this can easily be accomplished electronically using modulation techniques. For a ramp voltage V+dV where dV=ksin(ωt), the collector current, I(V+dV) may be expanded as a Taylor polynomial :

$$I(V+dV) = I(V) + I'(V)dV + \frac{I''(V)dV^2}{2!} + \frac{I'''(V)dV^3}{3!} + \frac{I''''(V)dV^4}{4!} + \ldots \tag{2.8}$$

Where I'(V)=dI/dV etc.

The terms corresponding to the different harmonics of the modulating frequency may be collected together, and so;

$$I(V+dV) = I_0(V) + [I'(V)k + \frac{I'''(V)k^3}{8} + \ldots]\sin\omega t - [\frac{I''(V)k^2}{4} + \frac{I''''(V)k^4}{48} + \ldots]\cos 2\omega t$$

$$\approx I_0(V) + I'(V)k\sin\omega t - \frac{I''(V)k^2\cos 2\omega t}{4} \tag{2.9}$$

assuming that k^3 and higher terms can be neglected. It can be seen that for small k, the fundamental frequency term is proportional to I'(V) and hence to N(E'). The second

harmonic is proportional to N'(E'), and this is true even for larger k values as the next higher k term is k^4. In practice almost all Auger spectra are recorded in the N'(E') mode by using a lock-in amplifier which is tuned to the second harmonic.

The resolution of the RFA is limited by local variations in the potential at the first grid and the retarding grid, deviations of the grids from spherical geometry, finite beam sizes and poor sample positioning. Variation in the work function of the grids may also present problems as may stray magnetic fields. In practice, retarding field analysers generally exhibit a resolution (ρ) of between 60 and 500. ρ is defined as the pass energy of the analyser, E, divided by the energy spread, ΔE_A, of the electrons transmitted by the analyser at that pass energy.

(2.8) The Cylindrical mirror analyser (CMA).

This device was first used by Blauth[7] and was later drawn attention to by Palmberg et al[8] who showed that the CMA was particularly suitable for AES because of its high signal to noise ratio and high transmission. The CMA, in contrast to the RFA (which acts as a high pass filter), acts similarly to a band pass filter rejecting all electrons outside of an energy window ΔE at a given pass energy, E. As the irreducible shot-noise in an analyser is proportional to the square root of the collector current, this means that the CMA will have an intrinsically higher signal to noise ratio than the RFA which collects many more electrons at a given pass energy which contribute nothing to the signal.

The CMA is a deflection type analyser consisting of two coaxial cylinders of radii r1 and r2 with annular entrance and exit slits cut in the inner cylinder. In operation, the inner cylinder is earthed and a deflecting potential V, is applied to the outer cylinder. Fig. 2.5 shows schematically the analyser used in the current work. This analyser was

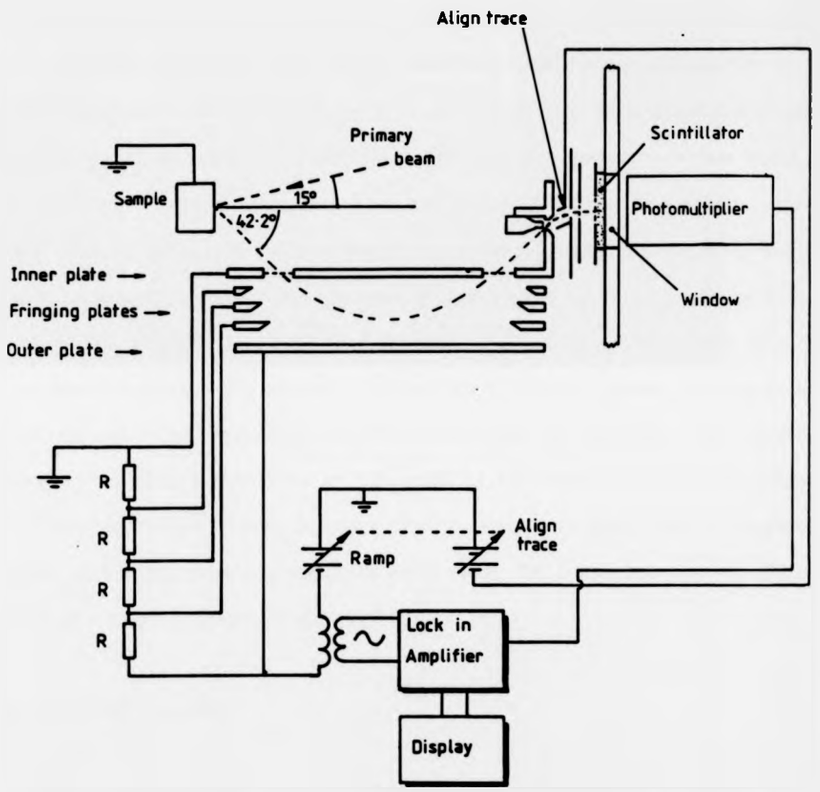

Fig. 2.5 This is a diagram of the hemi-cylindrical mirror analyser (HCMA) used in the current investigation. Electrons with the right energy travel through the analyser as shown and strike the scintillator. The main advantage of the HCMA as compared to the RFA is the fact the HCMA only collects those electrons in an energy window $\pm\Delta E$ about the analyser pass energy, E. This leads to a much higher sensitivity.

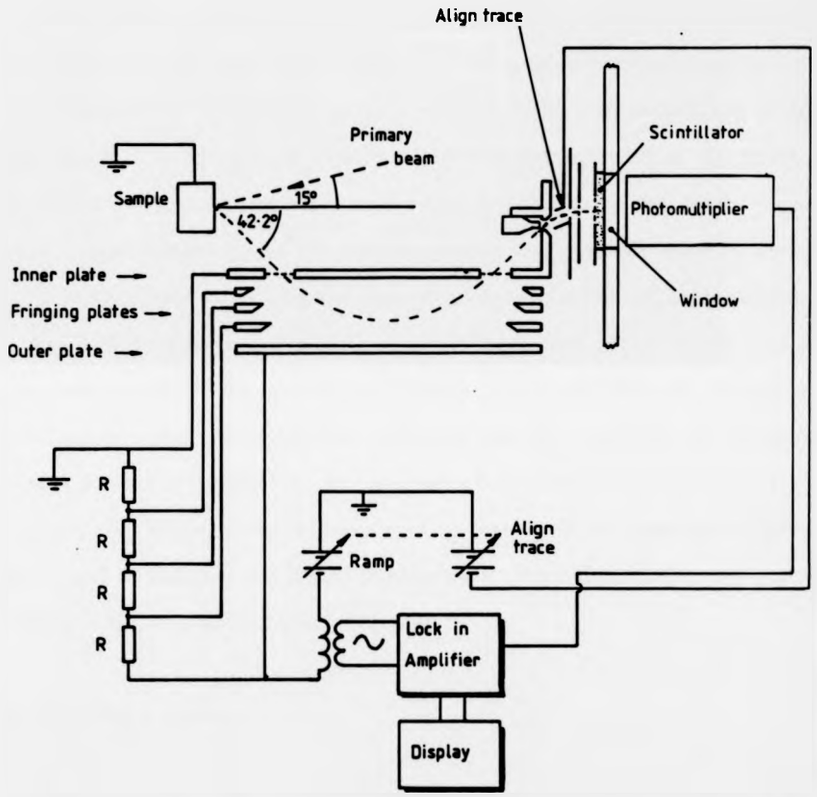

Fig. 2.5 This is a diagram of the hemi-cylindrical mirror analyser (HCMA) used in the current investigation. Electrons with the right energy travel through the analyser as shown and strike the scintillator. The main advantage of the HCMA as compared to the RFA is the fact the HCMA only collects those electrons in an energy window $\pm\Delta E$ about the analyser pass energy, E. This leads to a much higher sensitivity.

a V.G. hemi-CMA (HCMA), and differed from the more conventional devices only in that the coaxial cylinders had been sliced axially and the upper halves replaced by an electron gun. Conventional CMAs will usually have an axial gun or a separate electron gun which is arranged to be at grazing incidence to the sample. The geometry of the HCMA happens to be well suited to work on cylindrical crystals as the beam can easily be arranged to be at off-normal incidence to the sample (giving a slight increase in sensitivity in AES) and also in the plane containing the axis of the crystal and the sample normal.

In the CMA, electrons travel in a toroidal path and are brought to a focus on the axis. A small annular slit placed just before the focal plane is usually employed in order to increase the resolution. The V.G. HCMA was also equipped with fringing plates to compensate for field distorsions at the ends of the hemicylinders, and a post energy analysis filter, the 'align trace', whose function was to reject secondaries generated in the analyser, and so increase the signal to noise ratio. The current reaching the collector, I(E), in a CMA or a HCMA is given by equation (2.10)

$$I(E) = K\Delta EN(E) = KREN(E) \qquad (2.10)$$

Where K is a constant for a particular analyser and geometry, R is the resolution $\Delta E/E$ which is a constant, E is the pass energy and N(E) is the number of electrons collected at that pass energy.

In the case of the V.G.HCMA, the electrons leaving the align trace region were then accelerated to a scintillator which was kept at a high potential of 6 to 10 kV with respect to earth. The flashes of light produced at the phosphor then passed through a glass window and impinged on a photomultiplier situated externally to the vacuum. This device produced a large current proportional to the signal.

One of the advantages of the CMA (and HCMA) is that it is a double focussing analyser and has second order focussing for electrons leaving an axial source and entering the analyser at the ideal entrance angle of 42.3° to the analyser axis. Consider the Taylor series for the focal distance L about the ideal entrance angle α_o :

$$L(\alpha_o + \Delta\alpha) = L(\alpha_o) + \frac{\partial L}{\partial \alpha}_{\alpha_o} \Delta\alpha + \frac{\partial^2 L}{\partial \alpha^2}_{\alpha_o} \frac{(\Delta\alpha)^2}{2!} + \frac{\partial^3 L}{\alpha^3}_{\alpha_o} \frac{(\Delta\alpha)^3}{3!} + ... \quad (2.11)$$

Where $\Delta\alpha$ is the deviation of the secondary electron beam angle from the ideal angle. At $\alpha=\alpha_o=42.3°$, the first non vanishing partial derivative is $(\partial^3 L/\partial\alpha^3)|_{\alpha_o}$. It follows from this that for electrons leaving the source at angle $\alpha_o \pm \Delta\alpha$ to the CMA axis, the image of the source is at a distance proportional to $\Delta\alpha^3$ from the focal point. This means that larger deviations from the ideal angle for a given resolution are possible than would be the case if the focussing were first order where the first non vanishing integral is the second.

As with the RFA, the output current of the CMA may be differentiated electronically. This is done by applying small sinusoidal modulating voltage, $k\sin\omega t$, to the outer plate usually via an isolating transformer. This causes a modulation of the output current $I[E+ek\sin(\omega t)]$ which may be expanded as follows :

$$I(E + ek\sin\omega t) = I(E) + eI'(E)k\sin\omega t + \frac{e^2 I''(E)k^2 \sin^2\omega t}{2!} + ... \quad (2.12)$$

The amplitude of the I'(E) term corresponds to the first harmonic, and using equation (2.10) this may be written as :

$$I(\omega) = ekI'(E) = ekK\frac{\Delta[REN(E)]}{\Delta E} = ekKR[N(E) + EN'(E)] \qquad (2.13)$$

It can be seen that the first harmonic (which may be detected by using a lock-in amplifier) is not the pure derivative of the output current as it also contains an N(E) term. This term only becomes important at low energies however as EN(E) becomes small.

(2.9) Quantitative AES.

Consider the expression derived by Prutton[9] for the total Auger current observed i_A, in an experiment.

$$i_A = \frac{\Omega}{4\pi} I_0 \tau r(1-\omega)\Phi\sec\phi \qquad (2.14)$$

Where I_0 is the incident electron current, r is the backscattering factor (which increases the effective value of I_0), Φ is the ionization cross-section of the atom, ϕ is the angle of the incident beam to the surface normal, τ is the escape depth, ω is the fluorescence yield (the proportion of the decays lost to the competing process of X-ray fluorescence), and Ω is the solid angle accepted by the analyser. Also, the current actually measured will have been modified by the instrumental response function of the analyser plus electronics. It can be seen then, that quantification of AES will be rather difficult and indeed, the difficulty involved in determining all of these parameters is prohibitive to most workers. Generally, AES is quantified by using calibration techniques based on prepared standards. This will be the approach used in the present investigation.

(2.10) Adsorption on surfaces.

Any free surface has associated with it a surface energy which may be considered as arising from the bond breaking necessary to form the surface by cleaving the bulk solid[9,10,11]. The newly formed surface will undergo intrinsic relaxation processes such as surface relaxation and reconstruction, faceting and defect formation and change in band structure, but will be unable to completely eliminate the effect of the bonds lost at the surface. Thus a free relaxed surface may be likened in reactivity to a free radical or to an unsaturated molecule and will readily undergo chemical reactions in order to bring about a reduction in its excess surface energy. This minimization of surface energy is the driving force for all segregation and adsorption phenomena.

The forces binding adsorbate to adsorbent are the same as those which operate between two atoms or molecules except that the situation is made more complex by the fact that one of the species is also bound in a solid matrix. The forces comprising the adsorbate/adsorbent interaction may be summarised as follows ;

(a) Attractive Van der Waals forces.

(b) Repulsive overlap forces arising from the Pauli exclusion principle.

(c) Dipole interactions.

(d) Valency forces (responsible for chemisorption).

(e) Adsorbate/adsorbate interactions.

(2.11) Physisorption.

This is considered to be due to the superposition of the attractive, long range Van der Waals forces and the rather shorter range repulsive overlap forces. Generally, a Lennard-Jones type expression for the resultant force will be applicable. Thus, for two isolated gas atoms we may write :

$$E = \frac{a}{r^m} + \frac{b}{r^n} \qquad (2.15)$$

Where E is the energy of the interaction, r is the separation of the atoms and a,b,m and n are suitable constants. The adsorbate/adsorbent interaction is much more complicated than this however, as the adsorbate will interact in a complex manner with many adsorbent atoms. The required interaction potential will thus be the superposition of many such potential equations. Fig. 2.6 shows a hypothetical potential curve (curve P) for the physisorption of an atom onto a surface. The heat of physisorption is the depth of the potential well, E_p. Physisorption energies are typically less than about 0.25eV and the physisorption bond is weak.

(2.12) Chemisorption.

In contrast to physisorption, chemisorption represents a much stronger bond between adsorbate and adsorbent, typically of the order of several eV in energy. Fig. 2.6 shows simplified potential curves for the approach of a molecule Y-Y to a surface and its subsequent dissociative chemisorption. The height of the energy barrier E_a relative to the energy zero represents the magnitude of the activation energy for chemisorption, and it is this energy barrier which controls the rate of the chemisorption reaction. The depth of the potential well, E_c, is the energy of chemisorption, and the energy well E_p is the energy of adsorption into the precursor state which is in this case identified with a physisorbed state. If E_a is greater than zero, then the process is said to be activated. The energy D is the dissociation energy of the species Y-Y.

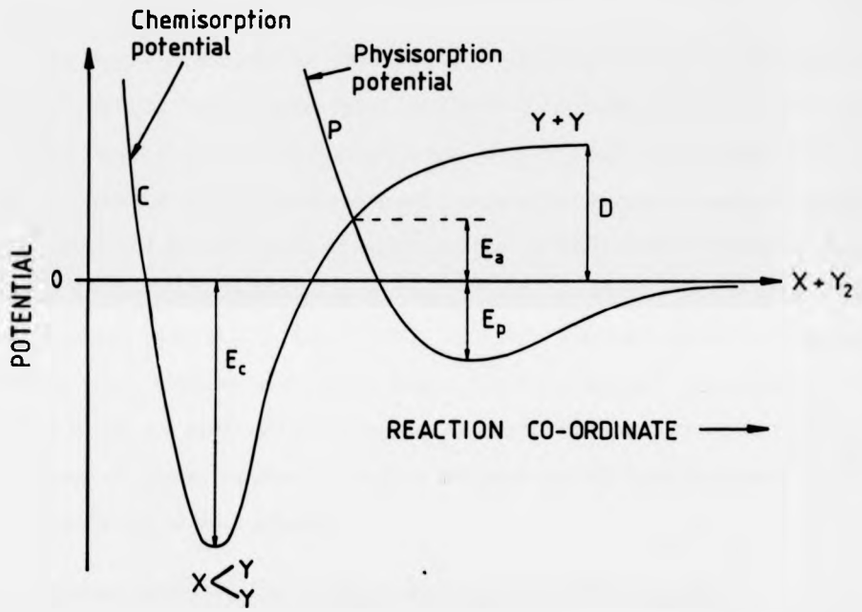

Fig. 2.6 This figure shows the hypothetical potential experienced by a molecule Y-Y approaching a surface along a reaction co-ordinate which is normal to the surface. X represents the surface, Y-Y is a diatomic molecule and D is the dissociation energy of Y-Y. The energies E_p and E_c are the energies for physisorption and chemisorption respectively, where curve P represents the physisorption potential and curve C represents the chemisorption potential. E_a is the activation energy barrier associated with the chemisorbed state, and (E_a-E_p) is the energy barrier between the physisorbed and chemisorbed states.

(2.13) The influence of surface crystallography on physisorption and chemisorption.

The above discussions of physisorption and chemisorption are simplistic in many ways, particularly in that they ignore the surface crystallography and assume perfectly planar surfaces. For real crystallographies, there are many energetically distinguishable adsorption sites and so the adsorbate may reside on the surface in many different states. These states will be separated in energy by energy barriers determined by the crossing points of complex physisorption and chemisorption potentials and it is these potential barriers which control the rate of transition from one state to another. Because of the relatively short chemisorption bond length, the local surface crystallography can be expected to have a profound influence on the chemisorption potential. The physisorbed state, however, can be expected to be much less aware of the local surface crystallography as the bond length is much greater.

(2.14) The effect of adsorbate/adsorbate interactions.

When two adsorbate molecules come into close proximity on a surface, interactions of a repulsive or attractive nature will come into play between them. These adsorbate/adsorbate interactions can have a profound effect on the chemisorption potential well. These interactions may cause an increase or decrease in *(a)* the depth of the chemisorption potential well, *(b)* the activation energy for adsorption or *(c)* the equilibrium distance of the adsorbates from the surface.

(2.15) Mechanisms for chemisorption and adsorption kinetics.

King[12] (see also ref.11) has proposed two mechanisms for chemisorption; the *trapping free* mechanism and the *trapping dominated* mechanism.

In the trapping free mechanism there is no accommodation in the physisorption well prior to chemisorption. This is characterized for chemisorption on adjacent sites with a random distribution of filled sites by a sticking coefficient which is proportional to the square of the number of vacant sites. Thus for saturation defined as $\theta = 1$:

$$s(\theta) = s_0(1-\theta)^2 \qquad (2.16)$$

Where s_0 is the sticking factor at zero coverage. Because there is no energy barrier to adsorption, the temperature dependence of $s(\theta)$ will tend to be small.

In the trapping dominated mechanism (the precursor state model), chemisorption is preceded by accommodation of the adsorbate into the physisorption well. These precursor state species may then undergo surface diffusion prior to either desorption or chemisorption. The transition from the physisorbed to the chemisorbed state is controlled by the energy barrier between the two states (E_a-E_p) and also by the degree of thermal accommodation of the physisorbed molecules to the surface. This latter temperature dependence is expressed in a pre-exponential factor which contains the ratio of the translational, rotational and vibrational partition functions for the activated complexes for desorption and adsorption, q_d/q_a, and the initial sticking coefficient may be written as :

$$s_0 = P_0[1 + \frac{q_d}{q_a} \exp \frac{(E_a-E_p)}{kt}]^{-1} \qquad (2.17)$$

Where P_0 is the probability of forming a precursor state species at zero coverage. If, as may be expected, q_d is greater than q_a and the temperature dependence of the pre-exponential term is substantially less than that of the exponential, then if $P_0\theta\theta s_0$, equation

2.17 may be written as :

$$s_0 = A\exp[-(E_a-E_p)/kT] \qquad (2.18)$$

This equation does, however, make the assumption of a fully thermally accommodated precursor state. it can be seen from this equation that an Arrhenius plot of $\log_e s_0$ vs. 1/T will have a slope equal to (E_a-E_p) and an intercept equal to $\log_e A$. If the precursor is not fully accommodated however, then the slope will be somewhat less than (E_a-E_p).

(2.16) The kinetics of reactions between two gases over metal surfaces.

Consider the catalytic oxidation of CO by oxygen atoms chemisorbed on a copper surface. Langmuir[13] has pointed out that there are essentially two extreme mechanisms for such a reaction :

(a) Both molecules are accommodated on the surface prior to reaction.

(b) Only one molecule is accommodated on the surface, and reaction occurs when the other species, impinging from the gas phase, makes a collision with an accommodated molecule.

The two possible mechanisms will obviously be characterized by rather different kinetics. Mechanism *(a)*, known as the Langmuir-Hinshelwood mechanism, will be characterized by a low initial rate of reaction as the surface is initially saturated with oxygen and there are no available sites for the accommodation of CO. The reaction rate will go through a maximum as oxygen is removed by CO as CO_2 (which is desorbed), and the number of vacancies for the CO molecule increases. Finally, the reaction rate becomes limited by the low concentration of chemisorbed oxygen and begins to fall to zero. In

contrast, mechanism *(b)*, the Eley-Rideal mechanism, predicts a high initial rate which falls off as the number of chemisorbed oxygen atoms decreases. This is because the chances of a suitable collision with a gas phase species depends on the number of oxygen atoms on the surface. Both these reactions will be discussed in much more detail in chapter 6.

(2.17) Segregation.

The driving force for all adsorption phenomena is the lowering of the excess free energy of the surface. This force may also cause diffusion of impurities from the bulk to occupy surface sites and so lower the surface energy. This phenomenon is known as segregation, and its equivalence to adsorption was first highlighted by Gibbs[14]. In segregation, the chemical potential of the system is controlled by the bulk concentration rather than by the gas pressure as in adsorption, and at a given chemical potential, the same state would be reached by either experiment once equilibrium had been attained. Whilst thermodynamically the two processes may be considered equivalent, it is obvious that the kinetics of segregation and adsorption will be very different as in the case of segregation the segregant diffuses from the bulk, whilst in the case of adsorption, the adsorbates impinge from the gas phase. There are many discussions of the thermodynamics of segregation eg. Oudar[10] and Blakely[15], and the readers attention is directed to a recent discussion of the kinetics of segregation by Rowlands and Woodruff[16]. As well as kinetic differences between the two processes, there is another very real experimental difference in that chemical potentials accessible by one experiment are often not readily accessible by the other. It is often the case that the low coverages often found in segregation experiments would require impossibly low gas partial pressures to realise in an adsorption experiment.

Chapter 2..... References

(1) Auger P., *J.Phys. Radium* 6 (1925) p.205

(2) Chattarji D., "The Theory of Auger Transitions", Academic Press, London, (1976)

(3) Lander, *Phys. Rev.* 91 (1953) p.1382

(4) Chung M.F., Jenkins L.H., *Surface Science* 22 (1970) p.479

(5) Sevier K.D., "Low energy electron spectrometry", Wiley-Interscience (1972) New York

(6) Weber R.E., Peria W.T., *J.Appl.Phys.* 38 (1967) p.4355

(7) Blauth E., *Z. Phys.* 160 (1957) p.228.

(8) Palmberg P.W., Bohn G.K., Tracey J.C., *Appl. Phys. Lett.* 15 (1969) p.254.

(9) Prutton M., "Surface Physics", Oxford Physics Series, Clarendon Press, Oxford (1975).

(10) Oudar J., "Physics and Chemistry of Surfaces", Blackie and Son Ltd. London (1975).

(11) Trapnell B.M.W., Hayward D.O., "Chemisorption", Butterworths, London

(12) King D.A., *Proc. 7th International Vacuum Congress & 3rd International Conference on Solid Surfaces* vol.ii p.769, Vienna (1977).

(13) Langmuir I., *Trans. Faraday Soc.* 17 (1921) p.621.

(14) Gibbs J.W., see "J.W.Gibbs, The scientific papers", Dover, New York (1961).

(15) Blakely J.M., "Introduction to the properties of crystal surfaces", Pergamon Press, Oxford, New York, Toronto, Sydney, Braunshweig.

(16) Rowlands G., Woodruff D.P., *Philosophical Magazine* A, (1979) vol.40 no.4 p.459-476.

(17) Burhop E.S.H., *The Auger Effect and Other Radiationless Transitions*, University Press, Cambridge, 1952.

Chapter 3

THE AUGER SPECTROMETER

Chapter 3..... Contents

(3.1) Introduction to chapter 3.

(3.2) The ultra high vacuum (UHV) chamber.

(3.3) The HCMA and ramp generator.

(3.4) The detection system.

(3.5) The electron gun and power supply.

(3.6) The physical imaging system.

(3.7) The argon ion gun.

(3.8) The cylindrical single crystals.

(3.9) Sample heating.

(3.10) The sample manipulator.

(3.11) Sample holders for cylindrical crystals.

(3.12) The computer interface.

(3.13) The software.

(3.14) Digital smoothing filters.

(3.1) Introduction to chapter 3.

This chapter describes the equipment used in the present investigation. The Vacuum Generators Auger electron spectrometer which was used throughout the course of this work will be described in some detail, with particular reference to some major enhancements made by the Author which allowed the device to be computer controlled. The cylindrical single crystals (prepared by Armitage[1]) will be described along with a novel method of mounting cylindrical samples which allows for sample heating as well as accurate axial rotation. The operating programs and related software for the computer controlled spectrometer will be briefly described, along with a brief discussion of the application of digital smoothing filters to Auger electron spectroscopy.

(3.2) The ultra high vacuum (UHV) chamber.

The apparatus consisted of a conventional stainless steel UHV chamber which was fitted with titanium sublimation and ion pumps, and which had a base pressure after bakeout of better than 5×10^{-10} torr. The chamber was equipped with a sample manipulator, a Vacuum Generators (V.G.) HCMA, a V.G. high intensity argon ion gun for sample cleaning, and a nude Bayard-Alphert type ionization gauge head for pressure measurement. Gas from the gas handling line could be admitted into the main chamber via the argon ion gun which was equipped with a V.G. leak valve, and the chamber could be isolated from the main pumping line by using a baffle valve. The main pumping line consisted of a polyphenyl ether diffusion pump which was separated from the experimental chamber by a liquid nitrogen cold trap to prevent back streaming of oil vapour. The diffusion pump was backed by an Edwards ED100 type rotary pump which was fitted with a molecular sieve foreline trap to prevent any back streaming of rotary pump oil vapours into the diffusion pump. Pressures in the backing line were measured with a Pirani gauge head

situated between the foreline trap and the diffusion pump. The main chamber with pumping and gas handling lines is shown schematically in fig. 3.1.

(3.3) The HCMA and ramp generator.

The electron energy analysis system comprised of a V.G. HCMA (described in section 2.8) and associated electronics. The voltages for the HCMA outer plate and align trace were provided by a V.G. fast scan ramp generator which had been modified by the Author to accept a 0 to 10V programming voltage from an external source. Thus, as well as manual operation, the ramp generator could be computer controlled. The slew rate of the internal high tension supplies could be as high as 1V/millisecond, and so if a large enough signal was available, Auger spectra could be observed in real time on an oscilloscope. The fast scan rate also allowed real time observation of the elastic peak in both E.N(E) and derivative modes and this facilitated the setting up procedure which involved maximizing the elastic peak by adjusting the HCMA to sample distance. An external modulating voltage from a Brookdeal lock-in amplifier was internally amplified by the ramp generator electronics and impressed on the outer plate ramp via an isolating transformer. The fast scan mode of the spectrometer necessitated a rather high modulation frequency of about 40kHz, and care had to be taken to ensure that capacitive loss of the modulation voltage in the connecting cables was not significant. The modulation voltage could be manually varied from 0 to 25V peak-to-peak. A digital volt meter was added to the ramp generator and was calibrated to display the pass energy of the analyser. The calibration point taken was the carbon peak at 272eV, and the ramp was found to be reasonably linear up to about 800eV.

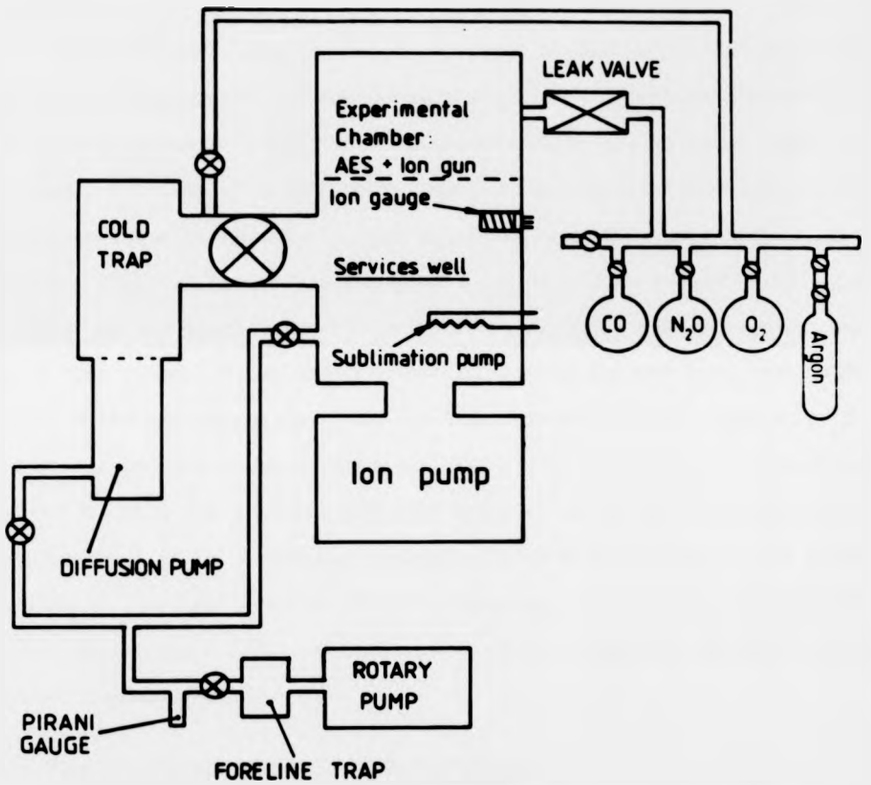

Fig. 3.1 This figure shows the main pumping line and the gas handling line of the apparatus used throughout this investigation. Gas from the gas handling line was admitted to the main chamber via a leak valve attached to the argon ion gun.

(3.4) The detection system.

As described in section 2.8, the detection system of the V.G. HCMA consisted of a scintillator and an external high sensitivity photomultiplier tube. The scintillator power supply was originally a V.G.IP80 programmable high tension power supply which was internally programmed to 4.5kV. Replacement of the original phosphor by the Author also necessitated the modification of this supply to be continuously variable between a few volts and 10kV as the new V.G. phosphor required a much higher operating voltage. In practice, the new scintillator was operated at as high a voltage as was possible (about 8.5kV), this voltage being limited by coronal discharges and insulator breakdown. The output of the photomultiplier tube was taken directly to the input of an XY display to allow monitoring of the spectra in the E.N(E) mode and also to the input of a Brookdeal lock-in amplifier for analogue differentiation by the phase sensitive detection of the first harmonic of the modulated signal (section 2.8). The output of the Brookdeal was taken to an auxiliary input on the XY display and also via a x10 buffering D.C. amplifier to a 12 bit analogue to digital (AD) input port on a GEC 4080 computer which was used for experimental control.

(3.5) The electron gun and power supply.

The electron gun used in this work was a Superior Electronics type SE-3K-5U low energy gun which was equipped with XY electrostatic deflection plates and which had been modified to take thoriated tungsten hairpin filaments. The gun is shown schematically in fig. 3.6 (p.45). For Auger use at a constant primary beam energy, the A1 and A3 electrodes were earthed and focusing was accomplished by applying a suitable voltage to the A2 electrode. The gun was capable of producing a maximum beam current at the sample of about 4 microamps, and by using a physical imaging system, the spot

size was estimated to be between 0.25 and 0.5 square millimetres. The electron gun power supply was designed and made by the University of Warwick Physics Department electronics workshop, and proved to be both highly stable and reliable.

(3.6) The physical imaging system.

The imaging system comprised of a control box to drive the XY deflection plates of the electron gun, a high impedance, low noise head amplifier to amplify the crystal current and an XYZ display to display the image. Both the head amplifier and the control box were designed and built by the electronics workshop. The box provided both X and Y shift and raster facilities and by feeding the raster to the X and Y inputs of the display and the amplified crystal current to the Z input, an image of the sample could be displayed. Because of the rather stringent focal requirements of the HCMA and the unusual geometry of the sample, electron beam imaging was found to be essential to the correct alignment of the system for AES. The imaging system also provided a useful diagnostic for any faults in the electron gun. The head amplifier could be used with several signal sources:

(a) The crystal current. This was the usual signal source for the head amplifier, and was utilised by connecting the head amplifier to the thermocouple wires which were spot welded to the top of the cylindrical samples.

(b) The output of the photomultiplier tube. Because of the high noise content of this source, the resultant image was virtually useless. This precluded any useful attempts at scanning AES.

(c) A copper gasket which had been coated with colloidal graphite and suspended in the vacuum chamber. By biasing the gasket a few hundred volts positive and connecting the head amplifier, a secondary electron image of the sample could be

obtained.

(3.7) The argon ion gun.

Sample cleaning was accomplished by a combination of argon ion bombardment while the crystal was rotated under computer control (typically, for the copper sample, 40 minutes of continuous rotation at a beam density of $5\mu Acm^{-2}$ and a beam energy of 0.5 to 1.5kV) followed by annealing to a suitable temperature. Because of the rather large surface area of the cylindrical samples, a V.G. high intensity ion gun was used. The ion gun was equipped with a large permanent magnet for ion beam focusing, and this was always removed prior to AES as it was found to bend the electron beam.

(3.8) The cylindrical single crystals.

The copper and nickel cylindrical single crystals used in this investigation had been prepared previously by Armitage[1]. The samples were accurately aligned by X-ray diffraction and then spark machined using brass tubes to form hollow cylinders. The crystals were then mechanically polished, using diamond paste (down to 0.25 microns), and given a brief electropolish. The samples were cut from 99.99% pure nickel and 99.999% pure copper (Metals Research Ltd.).

The method of preparation outlined above has several drawbacks; the surface finish after spark machining is quite poor, and the samples invariably have a small taper from top to bottom due to erosion of the brass tube. The Author has found, in some preliminary investigations into the preparation of cylindrical single crystals, that a more satisfactory method of preparing such samples is to mount the aligned single crystal rod axially on a rotating chuck, and spark machine parallel to the required axis using the square edge of a brass plate. The plate can be easily replaced if any signs of erosion occur. This method was found to produce well aligned samples of almost perfect cylindrical geometry

obtained.

(3.7) The argon ion gun.

Sample cleaning was accomplished by a combination of argon ion bombardment while the crystal was rotated under computer control (typically, for the copper sample, 40 minutes of continuous rotation at a beam density of $5\mu Acm^{-2}$ and a beam energy of 0.5 to 1.5kV) followed by annealing to a suitable temperature. Because of the rather large surface area of the cylindrical samples, a V.G. high intensity ion gun was used. The ion gun was equipped with a large permanent magnet for ion beam focusing, and this was always removed prior to AES as it was found to bend the electron beam.

(3.8) The cylindrical single crystals.

The copper and nickel cylindrical single crystals used in this investigation had been prepared previously by Armitage[1]. The samples were accurately aligned by X-ray diffraction and then spark machined using brass tubes to form hollow cylinders. The crystals were then mechanically polished, using diamond paste (down to 0.25 microns), and given a brief electropolish. The samples were cut from 99.99% pure nickel and 99.999% pure copper (Metals Research Ltd.).

The method of preparation outlined above has several drawbacks; the surface finish after spark machining is quite poor, and the samples invariably have a small taper from top to bottom due to erosion of the brass tube. The Author has found, in some preliminary investigations into the preparation of cylindrical single crystals, that a more satisfactory method of preparing such samples is to mount the aligned single crystal rod axially on a rotating chuck, and spark machine parallel to the required axis using the square edge of a brass plate. The plate can be easily replaced if any signs of erosion occur. This method was found to produce well aligned samples of almost perfect cylindrical geometry

with an excellent, almost mirror-like, surface finish. A brass tube may be used to cut out the centre of the cylinder. Unfortunately, lack of time prevented the Author from pursuing this method, and the samples prepared by Armitage were used throughout this work.

(3.9) Sample heating.

All the samples used in the current investigation were equipped with chromel-alumel T1/T2 type thermocouples and, after initial unsuccessful attempts at electron bombardment heating, heated radiatively by means of an axial tungsten filament. The temperature of the sample was originally controlled by adjusting the filament current using a Variac which was supplied with a stable input voltage from a Voltstat, but for later temperature controlled work a temperature control unit was built by the electronics workshop which could maintain the sample temperature to an accuracy of about ± 4°C.

(3.10) The sample manipulator.

The sample manipulator consisted of a V.G. universal motion drive type UMD1 which provided translations in the XY plane of 2 cm, a vertical translation in the Z direction of up to 5 cm and a polar rotation about the sample axis (the Z axis). Initially, work was done using the RD1 rotary motion drive supplied with the UMD1 which was turned by hand. However, because of the inherent inaccuracies of the old RD1 drive (non axial rotation and poor angular reproducibility) and also the large amount of time taken to collect Auger spectra every 5° of arc around the sample circumference, the drive was eventually replaced by a V.G. RD6 rotary motion drive which was then fitted with a W.D. Technologies stepper motor. This enabled the drive to be computer controlled, and provided an angular resolution of 0.5° with a quoted angular reproducibility of ±0.25° (the half step angle of the motor). This compared very favourably with the estimated

reproducibility of ±2° of arc provided by the RD1. The UMD1 XYZ motions were more than adequate to position the sample accurately at the CMA focal plane.

(3.11) Sample holders for cylindrical crystals.

The stringent focal requirements of the HCMA require that the sample be accurately positioned at the focal plane, and any small deviations from this position lead to large variations in the output signal. Indeed, deviations as little as 1mm can cause shifts in the Auger peak energies of a few eV and variations in the Auger peak intensities of up to 20%. This presents a problem when Auger peaks are to be recorded around the circumference of a cylindrical sample, as any eccentricity in the sample rotation will cause the point of analysis to move to and fro along the HCMA axis and so cause significant Auger peak position and intensity changes. This is not too important a problem however, as the net effect of this is to cause a single smooth sinusoidal oscillation of the Auger peak amplitudes around the 360 degrees of crystal rotation. The crystallographically dependent effects are superimposed on this oscillation and may be easily distinguished from it by their 2mm point group symmetry (derived from that of the <110> axis cylinder) and the much smaller angles of arc over which the features occur.

A much more important effect of eccentricity in rotation is the angular distortion it produces in the data. As fig. 3.2 shows, the angular rotation of the sample about its axis, Φ, is not identical to nor linearly related to, the surface plane rotation, θ. The effect of this is that on one side of the crystal more than 180° of θ is bunched into 180° of Φ whilst on the other side of the sample the reverse is true. For a crystal of approximately 12mm diameter as used in these experiments, an eccentricity of just 1mm will produce a worst case angular error of 10°. Without crystal symmetries this would be a very severe source of error. Obviously, for convenience and accuracy, the crystal

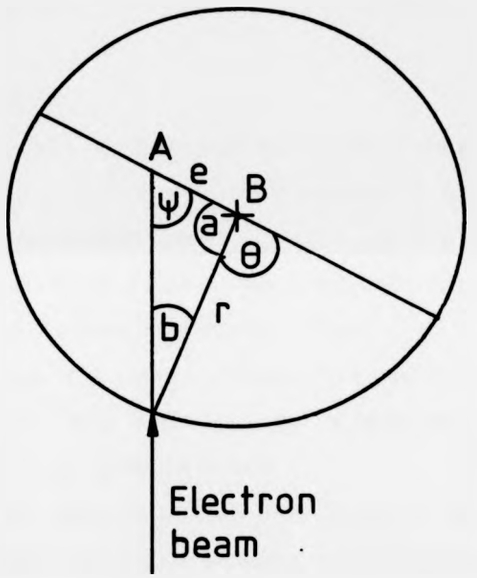

Fig. 3.2 This figure shows a plan view of an eccentrically mounted cylindrical single crystal. **A** is the axis of rotation of the sample and **B** is the axis of the cylindrical single crystal. **e** is the eccentricity, which is the linear distance between the axis of rotation and the cylinder axis, and **r** is the radius of the cylindrical single crystal. It is easily seen that for such an eccentrically mounted sample, the surface plane rotation, θ, is not equal to nor linearly related to the rotation about the axis of rotation, ψ. Indeed, it may be easily shown that:

$$\theta = \psi + \sin^{-1}\left[\frac{e\sin\psi}{r}\right]$$

should rotate with the minimum eccentricity and so a special sample holder was designed to facilitate 'centering' of the sample on the axis of rotation.

Fig. 3.3 is a diagram of the centering device, which consisted of the following components :

(i) The sample mount S.

(ii) 10BA mounting bolts a, which could be adjusted in the ceramic disk A to provide an azimuthal tilt for the crystal. The ceramic disk, A, served to isolate the sample from the earthed rotary drive shaft.

(iii) A disc D which sits in a hole in plate C and which can be accurately positioned in the XY plane by adjusting the centering bolts c.

(iv) A disk E which is mounted on the shaft of the rotary drive and which can be clamped by bolts e to disk C in order to lock disc D in position and thus allow the removal of the centering bolts c.

Centering was accomplished by observing the side of the crystal in an optical microscope and then adjusting bolts c to minimize the excursion of the sample across the field of view on rotation of the rotary drive. The sample was then clamped in position by tightening bolts e, using plate E as a friction lock. This meant that the bolts c could be safely removed. A small amount of azimuthal tilt could also be accommodated for by adjusting bolts a. This device proved to be exceedingly reliable, and allowed the centering of the crystal to an eccentricity of less than 0.25mm. Unfortunately, as the samples used in the current work were not perfectly cylindrical (tapering very slightly from top to bottom), the angular distortions could not be fully eliminated, but were, however, reduced to only 1 or 2 degrees.

The sample mount itself provided many problems due to the small size of the cylinders (inner and outer diameters of 8mm and 12mm respectively) and the necessity of an axial

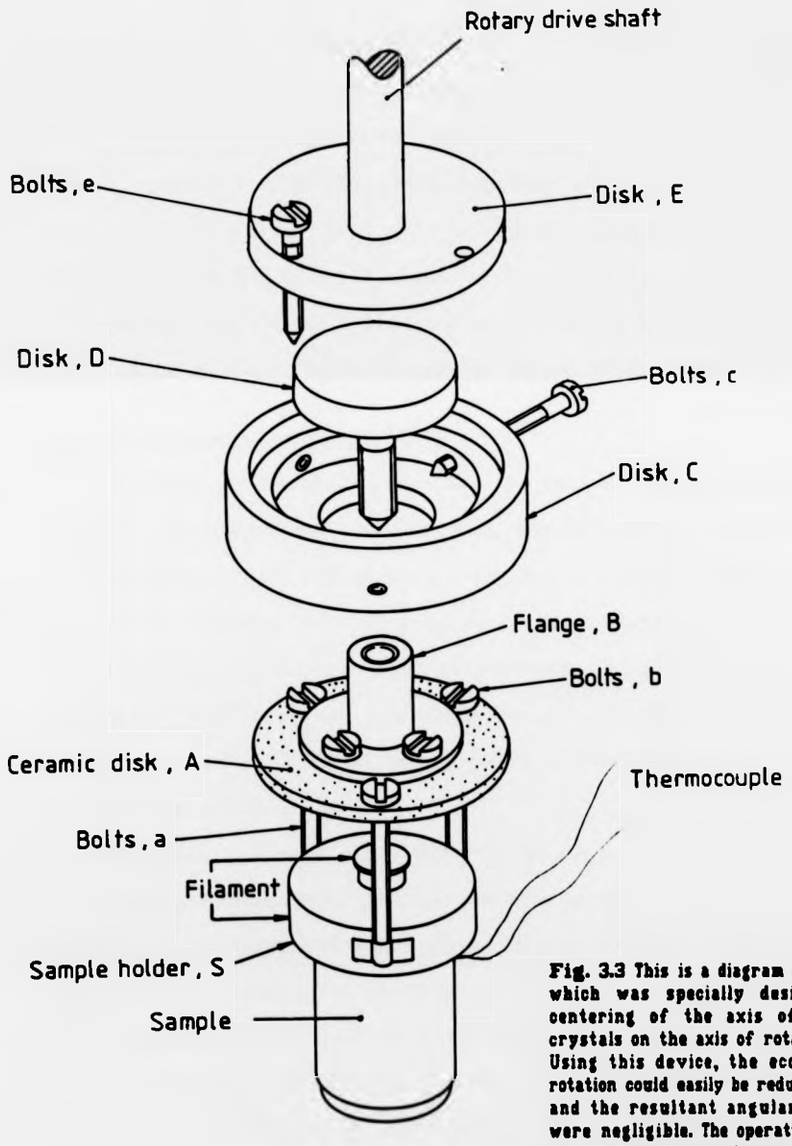

Fig. 3.3 This is a diagram of the sample manipulator which was specially designed to facilitate the centering of the axis of the cylindrical single crystals on the axis of rotation of the rotary drive. Using this device, the eccentricity in the sample rotation could easily be reduced to as little as 0.25mm, and the resultant angular distortions in the data were negligible. The operation of this device is fully described on the previous page.

tungsten filament for radiative heating. Armitage[1] had clamped the samples between stainless steel plates, but this was found to be rather unsatisfactory in the present investigation as the samples had a tendency to move on heating. The problem seemed to lie in the axial (rather than radial) expansion of the cylinders on annealing to 700-800°C after argon ion bombardment. A special sample holder was designed which permitted some longitudinal expansion of the crystal whilst preventing any motion off axis. Two variants of the design are shown in fig. 3.4a and b. Sample holder a was used for the copper crystal whilst sample holder b was used for the nickel crystal.

(3.12) The computer interface.

Initially, all the data were taken by recording Auger spectra in the derivative mode on a chart recorder and measuring the peak-to-peak heights. As an experiment in which spectra were taken every 5 degrees of arc around the sample circumference entailed the recording of 74 spectra, and the spectrometer had to be reset and the crystal turned by 5 degrees between each datum, experimental time would seldom be less than three and a half hours and the subsequent processing of the data could easily take as long as two. This procedure was very slow, tedious and inaccurate and so it was decided to computerize the experiment.

The computer used was a GEC 4080 which is a multi user system equipped with digital, digital to analogue (DA), and analogue to digital (AD) ports with 12 bit resolution. A schematic of the computer interfacing is shown in fig. 3.5. Basically, one 12 bit AD port was used to sample the analogue output of the Brookdeal lock-in amplifier, one 12 bit DA port was used to provide a programming voltage for the modified ramp generator, and two 8 bit DACs were used to provide TTL compatible control outputs for the stepper motor control unit (which was built by the Author from a schematic by WD Technologies).

tungsten filament for radiative heating. Armitage[1] had clamped the samples between stainless steel plates, but this was found to be rather unsatisfactory in the present investigation as the samples had a tendency to move on heating. The problem seemed to lie in the axial (rather than radial) expansion of the cylinders on annealing to 700-800°C after argon ion bombardment. A special sample holder was designed which permitted some longitudinal expansion of the crystal whilst preventing any motion off axis. Two variants of the design are shown in fig. 3.4a and b. Sample holder a was used for the copper crystal whilst sample holder b was used for the nickel crystal.

(3.12) The computer interface.

Initially, all the data were taken by recording Auger spectra in the derivative mode on a chart recorder and measuring the peak-to-peak heights. As an experiment in which spectra were taken every 5 degrees of arc around the sample circumference entailed the recording of 74 spectra, and the spectrometer had to be reset and the crystal turned by 5 degrees between each datum, experimental time would seldom be less than three and a half hours and the subsequent processing of the data could easily take as long as two. This procedure was very slow, tedious and inaccurate and so it was decided to computerize the experiment.

The computer used was a GEC 4080 which is a multi user system equipped with digital, digital to analogue (DA), and analogue to digital (AD) ports with 12 bit resolution. A schematic of the computer interfacing is shown in fig. 3.5. Basically, one 12 bit AD port was used to sample the analogue output of the Brookdeal lock-in amplifier, one 12 bit DA port was used to provide a programming voltage for the modified ramp generator, and two 8 bit DACs were used to provide TTL compatible control outputs for the stepper motor control unit (which was built by the Author from a schematic by WD Technologies).

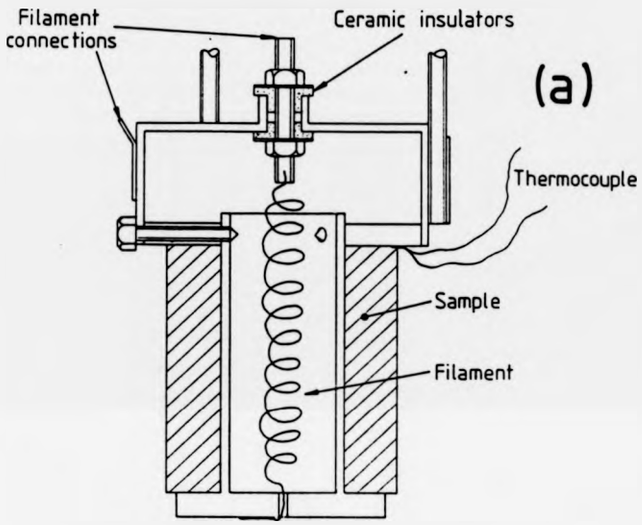

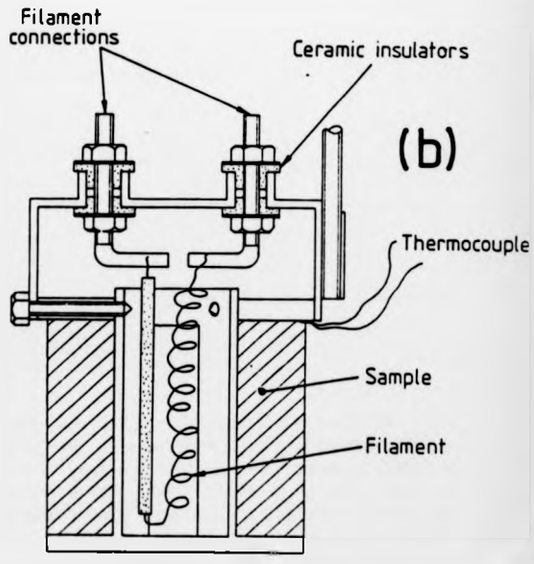

Fig. 3.4 This figure shows the two sample holders used in this investigation in cross-section. The hollow cylindrical samples are pushed onto hollow cylindrical tubes as shown, and clamped between the two end plates. This completely eliminated the problem of the samples moving off axis during annealing.

Sample holder (a) was used for the copper sample, and it can be seen that the current to the filament travels down through the cylindrical sample which is part of the circuit.
Sample holder (b) was used for the nickel sample, and in this sample holder sample and filament are completely isolated.

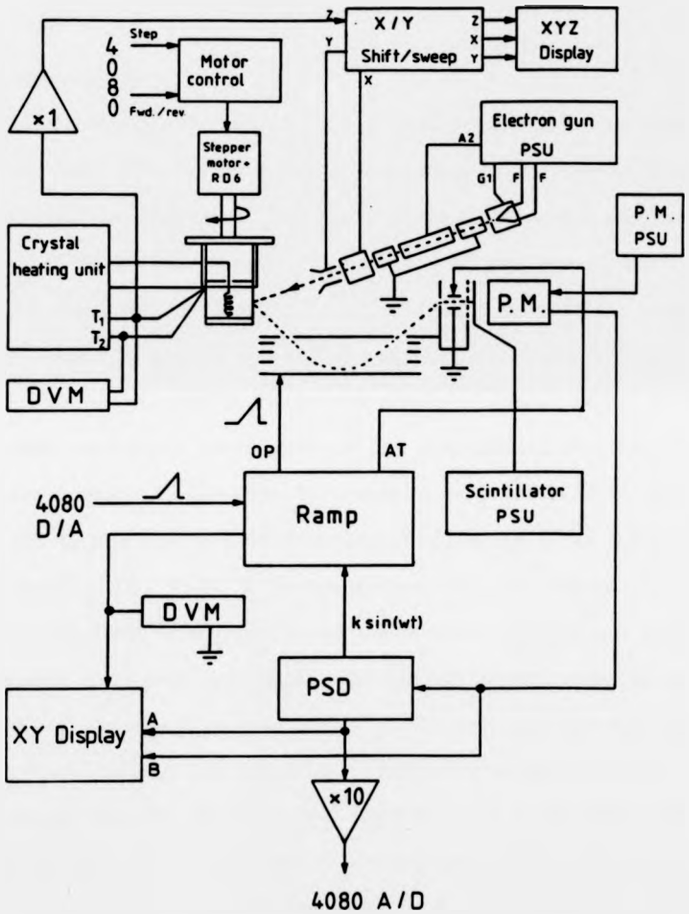

Fig. 3.5 This figure is a functional diagram of the apparatus used in this investigation. The letters P.M. stand for photomultiplier, the letters DVM stand for digital volt meter and the GEC4080 computer to which the apparatus was interfaced is denoted simply as 4080. The PSD used throughout this work was a Brookdeal lock-in amplifier, and the spectra were digitized to 12 bit resolution using analog to digital converters attached to the computer.

(3.13) The software.

All the operating software for the computer controlled spectrometer was written in FORTRAN on the GEC 4080 computer in the physics department. The program ASPEC8 was the main control program for the spectrometer and this was supplemented by several simple utilities. BOMBARD was a simple program which allowed the crystal to be continuously rotated during argon ion bombardment and gas dosing whilst XTALC measured the sample current at 1° intervals around the 360° of sample rotation. JPLOT2 was used to normalize the Auger peak-to-peak heights to the average peak-to-peak height of a reference peak recorded around the sample circumference and JIMPLOT simply plotted out previously recorded Auger spectra. A Televideo 912C terminal with Graffix 4010 emulation interfaced to an Epson FX-80 dot matrix printer provided the plots. When hard copy of the data was not required, a BBC model B microcomputer with the Sussex University terminal emulation ROM was used as a graphics terminal. Several programs were written on the BBC microcomputer and also on a Sinclair Spectrum 48K microcomputer to allow file transfer from the 4080 for further data processing and archiving as space on the GEC cartridge drives was often limited. Two programs, SLICE18 and 110CYL were written on the microcomputers to plot out an arbitrary crystal plane in an arbitrary lattice (of not more than 128 atoms) and to plot out all the crystal planes at 5 degree intervals around the crystal circumference. All the diagrams of crystal planes in this thesis were generated using one of these programs. All the calculations for the models presented in the later chapters of this thesis were performed on Spectrum and AppleX+ microcomputers.

(3.14) Digital smoothing filters.

One of the major advantages gained by computerizing the experiment was the ability to apply digital signal processing techniques to the digitized spectra. Digital smoothing filters can markedly increase the signal to noise ratio of a noisy signal (as demonstrated for AES by Prutton[2]), and are much more versatile, accurate and controllable than their analogue counterparts. Two digital filters were considered for use in the current work, each of which fitted a smoothing third order polynomial to the data. The smoothing spline algorithm (Reinsch[3]) has been recommended by Prutton[2] and was already implemented on the GEC 4080 at Warwick. The smoothing spline gives a very good subjective smooth to the data, but has the disadvantage of being a long and slow algorithm, and requires the input of two parameters by the operator, the 'stiffness' and the 'signal to noise ratio', which control the amount of smoothing. The stiffness should be in the interval $N \pm \sqrt{N}$, where N is the number of points in the peak to be fitted, and the signal to noise ratio should be estimated from the scatter on the data. The problem encountered with this routine was that for a given Auger peak, spectra of different intensities seemed to require widely different signal to noise ratios or stiffnesses for a good fit. In the present work on cylindrical single crystals where there is a large anisotropy in Auger peak-to-peak heights around the sample, this necessitated input from the operator after every spectrum, and often several guesses had to be made to find the correct signal to noise ratio. Prutton has approached this problem by estimating the signal to noise ratio from least squares straight lines fitted to the beginnings and ends of the spectra and has had great success. This approach was tried in the present work, but still seemed incapable of coping with the marked variations in Auger intensity observed around the cylinders. The reasons for this were never fully understood.

The digital smoothing filter finally chosen was a variation of the Savitsky/Golay sliding least squares digital smoothing algorithm[4]. This algorithm is based on equation 3.1, where the smoothed point y(0) is in the centre of an odd number interval of points P, where P=2m+1 and m is any integer. The experimental data points in the interval, $f(t)$, are convoluted with appropriate integers C_t and normalized by the factor NORM.

$$y(0) = \sum_{t=-m}^{m} \frac{C_t f(t)}{NORM} \qquad (3.1)$$

The simplest case is with C_t=1 (for all t) and NORM=P when the equation reduces to a sliding average. A least squares fit of an n^{th} order polynomial to the data over the interval will allow the calculation of the integers and of NORM to give an exact least squares fit of y(0). Values of C_t and NORM for polynomials of order 2 to 5 and intervals in the range 1 to 25 points are given in reference 4, and corrections to some of these by Steinier et al can be found in reference 5.

An unfortunate aspect of this central point smoothing mechanism is that m points are of necessity lost from each end of the spectrum after each smooth. In the extended sliding least squares fit used in the current work, Proctor and Sherwood[6] fit the first and last m spectral points with a smoothing parabola and add this to the smoothed data. This approximation works extremely well in practice, producing only very small end distortions, and it also makes possible iteration of the smooth as the number of spectral points is conserved. Savitsky and Golay state that iteration of the smooth, such as a 2a+1 followed by a 2b+1 point smooth, should be exactly the same as a smooth with an interval of 2(a+b)+1 points. Proctor and Sherwood clearly demonstrate that this is not the case, and indeed recommend the use of the smallest smoothing interval possible with many iterations. In the present work, perhaps due to the low number of points per spectrum

The digital smoothing filter finally chosen was a variation of the Savitsky/Golay sliding least squares digital smoothing algorithm[4]. This algorithm is based on equation 3.1, where the smoothed point y(0) is in the centre of an odd number interval of points P, where P=2m+1 and m is any integer. The experimental data points in the interval, $f(t)$, are convoluted with appropriate integers C_t and normalized by the factor NORM.

$$y(0) = \sum_{t=-m}^{m} \frac{C_t f(t)}{NORM} \qquad (3.1)$$

The simplest case is with C_t=1 (for all t) and NORM=P when the equation reduces to a sliding average. A least squares fit of an n^{th} order polynomial to the data over the interval will allow the calculation of the integers and of NORM to give an exact least squares fit of y(0). Values of C_t and NORM for polynomials of order 2 to 5 and intervals in the range 1 to 25 points are given in reference 4, and corrections to some of these by Steinier et al can be found in reference 5.

An unfortunate aspect of this central point smoothing mechanism is that m points are of necessity lost from each end of the spectrum after each smooth. In the extended sliding least squares fit used in the current work, Proctor and Sherwood[6] fit the first and last m spectral points with a smoothing parabola and add this to the smoothed data. This approximation works extremely well in practice, producing only very small end distortions, and it also makes possible iteration of the smooth as the number of spectral points is conserved. Savitsky and Golay state that iteration of the smooth, such as a 2a+1 followed by a 2b+1 point smooth, should be exactly the same as a smooth with an interval of 2(a+b)+1 points. Proctor and Sherwood clearly demonstrate that this is not the case, and indeed recommend the use of the smallest smoothing interval possible with many iterations. In the present work, perhaps due to the low number of points per spectrum

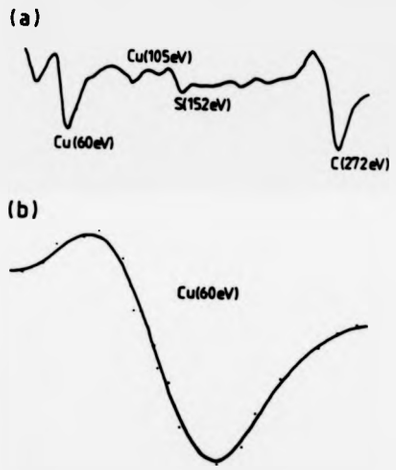

Fig. 3.6 This figure shows (a) an Auger survey of a carbon and sulphur contaminated copper surface and (b) a low-energy copper (60eV) peak. Both spectra have been digitized and then smoothed using a Savitsky-Golay digital smoothing filter. For the Auger survey, 99 points were collected over the spectrum at a rate of 1 second per point, and the data were smoothed using a 5 point smoothing interval. For the low-energy copper peak, the spectrum was recorded at the rate of approximately 3ms/point, and a nine point smoothing interval was used. The beam current at the sample was about 4μA, and the beam energy was 1.7keV.

(about thirty), it was found that there was little advantage to be gained by iterating, and so a single smooth was used with an interval of twice the peak width at half maximum as suggested by Edwards and Willson[7]. For a 30 point oxygen or copper peak, a single 9 point smooth consistently gave excellent results. An example of a smoothed copper peak is shown in fig.3.6.

Chapter 3..... References

(1) Armitage A.F., Ph.D. thesis, the University of Warwick (1981).

(2) Prutton M., to be published in *Appl. Spectrosc.*.

(3) Reinsch C.H., *Numerische Mathematik* 10 (1967) p.177.

(4) Savitsky A., Golay M.J.E., *Anal. Chem.* 36 (1964) p.1627-1639

(5) Steinier J., Termonia Y., Deltour J., *Anal. Chem.* 44 (1972) p.1900-1909.

(6) Proctor A., Sherwood M.A., *Anal. Chem.* 52 (1980) p.2315-2321.

(7) Edwards T.H., Willson P.D., *Appl. Spectrosc.* 28 (1974) p.541-545.

Chapter 3..... References

(1) Armitage A.F., Ph.D. thesis, the University of Warwick (1981).

(2) Prutton M., to be published in *Appl. Spectrosc.*.

(3) Reinsch C.H., *Numerische Mathematik* 10 (1967) p.177.

(4) Savitsky A., Golay M.J.E., *Anal. Chem.* 36 (1964) p.1627-1639

(5) Steinier J., Termonia Y., Deltour J., *Anal. Chem.* 44 (1972) p.1900-1909.

(6) Proctor A., Sherwood M.A., *Anal. Chem.* 52 (1980) p.2315-2321.

(7) Edwards T.H., Willson P.D., *Appl. Spectrosc.* 28 (1974) p.541-545.

Chapter 4

SURFACE CRYSTALLOGRAPHY OF THE CYLINDRICAL SINGLE CRYSTALS AND PRELIMINARY EXPERIMENTS

Chapter 4..... Contents

(4.1) Introduction.

(4.2) Cylindrical single crystals.

(4.3) The <110> axis cylinder.

(4.4) Vicinal surfaces.

(4.5) The stability of vicinal surfaces.

(4.6) Nomenclature of vicinal surfaces.

(4.7) Crystallographic incident beam effects in AES.

(4.8.1) The thermal decomposition of carbon monoxide on the vicinal surfaces of nickel: Previous work.

(4.8.2) CO decomposition on Ni: Experimental procedure, results and discussion.

(4.8.3) Carbon and sulphur segregation in nickel: Previous work.

(4.8.4) Carbon segregation in nickel: Experimental procedure.

(4.8.5) Results and discussion.

(4.8.6) Conclusions.

(4.1) Introduction.

This chapter will describe the features of the <110> axis cylinders that have been used throughout this work. Particular emphasis will be placed on the surface crystallography of the samples, and on the stability of the vicinal surfaces expected from the terrace, ledge, kink (TLK) model under adsorption. No technique of surface crystallography was made available for the present study and so assumptions about the surface crystallography of the cylinder must be made based on the available evidence in the literature.

The chapter will go on to present some preliminary work on carbon monoxide adsorption and carbon and sulphur segregation in nickel which was done prior to the computerization of the experiment. Whilst the results of these preliminary investigations cannot be considered conclusive, they do, however, serve to highlight certain experimental difficulties, and also illustrate clearly the importance of sample purity in adsorption experiments. The design of the computerized experiment and the later work on the copper cylinder relyed heavily on the experience gained in this preliminary investigation.

(4.2) Cylindrical single crystals.

In order to investigate the influence of surface crystallography on adsorption and segregation experiments, the experiment must be repeated several times on different crystal planes. One way of approaching this problem is to prepare many different single crystal samples each of which exhibits a different surface orientation. Many such comparisons have been made in the past, but it is difficult to rule out spurious effects due to differences in sample preparation and purity, and to ensure identical experimental conditions for each sample. Also, the range of orientations investigated tends to be limited by experimental time. These problems may be solved by using a sample which has been specially cut to

(4.1) Introduction.

This chapter will describe the features of the <110> axis cylinders that have been used throughout this work. Particular emphasis will be placed on the surface crystallography of the samples, and on the stability of the vicinal surfaces expected from the terrace, ledge, kink (TLK) model under adsorption. No technique of surface crystallography was made available for the present study and so assumptions about the surface crystallography of the cylinder must be made based on the available evidence in the literature.

The chapter will go on to present some preliminary work on carbon monoxide adsorption and carbon and sulphur segregation in nickel which was done prior to the computerization of the experiment. Whilst the results of these preliminary investigations cannot be considered conclusive, they do, however, serve to highlight certain experimental difficulties, and also illustrate clearly the importance of sample purity in adsorption experiments. The design of the computerized experiment and the later work on the copper cylinder relyed heavily on the experience gained in this preliminary investigation.

(4.2) Cylindrical single crystals.

In order to investigate the influence of surface crystallography on adsorption and segregation experiments, the experiment must be repeated several times on different crystal planes. One way of approaching this problem is to prepare many different single crystal samples each of which exhibits a different surface orientation. Many such comparisons have been made in the past, but it is difficult to rule out spurious effects due to differences in sample preparation and purity, and to ensure identical experimental conditions for each sample. Also, the range of orientations investigated tends to be limited by experimental time. These problems may be solved by using a sample which has been specially cut to

display a range of surface crystallographies.

A spherical single crystal would exhibit all possible orientations, and indeed Gwathmey and co-workers have performed many experiments on such samples (see reference 1 for a review of this work). For the current work, spherical single crystals were rejected in favour of cylindrical single crystals which exhibit a smaller range of surface orientations, but have a geometry which is much more suitable for AES. Armitage[2] has attempted AES on hemispherical single crystals, but has had little sucess due to an inability to identify the particular orientation at the point of analysis. If a cylindrical crystal is used, however, the crystal may be rotated axially causing the point of analysis to move around the circumference of the cylinder, and by use of crystal symmetries in the data, the orientation may be identified unambiguosly.

(4.3) The <110> axis cylinder.

If the axis of the cylindrical single crystal is defined as [1$\bar{1}$0], then the crystal surface presents all orientations (h,k,l) for which h=k. This means that the three low index faces (001), (110) and (111) are available for study as the (113) face and a continuum of vicinal orientations. Fig. 4.1a shows the relationship of the <110> axis cylinder to the FCC lattice and a plan view of the cylinder looking down the <110> axis, showing the main low index orientations (001), (111), (113) and (110). The three low index planes (001), (111), (113) and (110) are well characterized for both copper and nickel, and much is known about their physical and chamical properties. A particular attraction of cylindrical single crystals is that they present a range of vicinal surfaces for study which have received little or no previous attention.

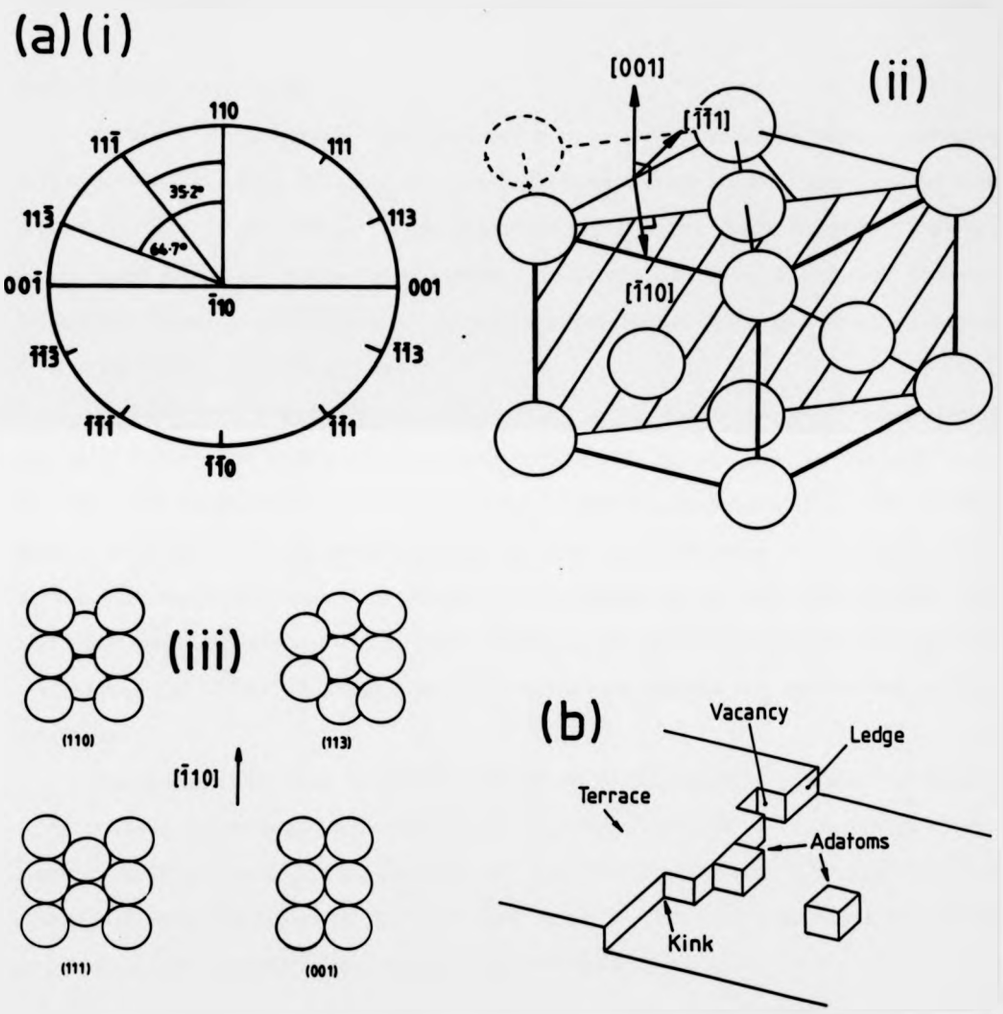

Fig. 4.1a shows (i) a plan view of the <110> axis cylinder with the cylindrical axis defined as [$\bar{1}$10], (ii) the relationship of the <110> axis cylindrical single crystals to the FCC lattice, and (iii) the four low index planes (110), (113), (111) and (001).

Fig. 4.1b shows schematically the T.L.K. (terrace, ledge, kink) model of a monatomically stepped surface.

(4.4) Vicinal surfaces

Kossel[3] and Stranski[39] have proposed a model for vicinal surfaces, the terrace, ledge, kink (TLK) model. This model assumes that any surface slightly misorientated from a low index plane is composed of low index terraces separated by monatomic steps. Curvature of the steps may be accounted for by assuming the presence of kinks in the steps produced by missing atoms. A vicinal surface is shown schematically in fig. 4.1b as a combination of monatomic steps, terraces and kinks.

An important property of the <110> axis cylinder is that if the surface is perfectly TLK, and the crystal well aligned, all step ledges will run parallel to the <110> axis, and the kink density will be zero. Furthermore, the TLK model predicts that the step density will vary linearly around the crystal circumference from local maxima on the atomically 'rough' (110) and (113) faces, to local minima on the atomically 'smooth' (111) and (001) faces[2,4,5]. Thus, the <110> axis cylinders present an excellent opportunity to investigate the effect of monatomic steps and differences in step density on surface reactivity.

There are many observations of stepped surfaces described in the literature and many different techniques have been applied to their study: LEED, reflection high energy electron diffraction (RHEED), transmission electron microscopy (TEM) and field ion microscopy (FIM) observations have all been reported. The reader's attention is directed to reference 6 for a useful summary of some of this work.

(4.5) The stability of vicinal surfaces.

If a Wulff construction is done in the <110> zone, then it is seen that the cusps in the surface energy occur on the low index planes (110), (111) and (001). The equilibrium shape of a cylindrical <110> axis single crystal is thus a polygonal prism with (110),

(001) and (111) type facets. However, the difference in surface energy between the different orientations is only of the order of 1%, and the faceting is severely kinetically limited by the rate of mass transport.

It is not suprising then, that clean metal surfaces are not known to exhibit such macroscopic faceting except after long periods at high temperatures. It has been shown by various workers that clean vicinal surfaces of platinum[7,8,9] and copper[10,11,12], for example, exhibit the expected TLK morphology even at high temperatures, whilst nickel vicinals which are close to either (111) or (001) have been shown to undergo a reversible step rearrangement with temperature which may or may not be linked with impurities[13,14,15]. Blakely and Somorjai[9] have also observed faceting of atomically clean platinum surfaces in the (100) and (110) zones to 'hill and valley' structures with multiple height steps. Under chemisorption, the situation is complicated still further as the adsorbate modifies the surface energy. Adsorbates may cause faceting of a surface or may enhance the stability of the TLK morphology as may be seen in the work on carbon and sulphur segregation in nickel by Thapliyal and Blakely[14].

To summarize this section then, it is not possible to generalize about the stability of metal vicinal surfaces. In the following experimental sections, there will be a detailed summary of previous work done on the vicinal surfaces presented by the copper and nickel cylinders, and their expected morphologies under the influence of the various adsorbates and reaction conditions encountered in this work. It will be seen that the copper cylinder can be expected to exhibit standard TLK vicinals under all of the conditions studied, whilst there is good evidence that the nickel cylinder facets under carbon segregation.

(4.6) Nomenclature of vicinal surfaces.

An arbitrary crystal plane may be uniquely identified by its Miller indices. This notation, whilst concise, does not give any idea as to the actual surface morphology however. Lang et al.[7] have devised a much more descriptive notation for stepped surfaces in which the surfaces are specified in terms of the terrace orientation and width and the step orientation and height. A stepped surface is denoted in this notation by :

$$E(S)\text{-}[m(h,k,l) \times n(h',k',l')] \qquad (4.1)$$

Where;

E denotes the element or compound.

S denotes a stepped surface.

m is the average number of atom rows comprising a terrace.

n is the average number of atom layers in a step.

(h,k,l) are the Miller indices of the terrace.

(h',k',l') are the Miller indices of the ledge.

Thus, the stepped surface shown in fig. 4.2b is denoted by Cu(S)-[4(111)x1(001)] and has the approximate Miller indices (117). Fig. 4.2a shows the TLK model of the vicinal surfaces generated by progressive misorientations of 5° from (001) to (110) around the circumference of the cylinder. These diagrams were generated by the program 110CYL (see section 3.13).

Eizenberg and Blakely[16] have proposed an alternative notation for stepped surfaces, which, whilst less descriptive than that of Lang, is often useful for its brevity. A surface which is misorientated from a low index plane (h,k,l) by a rotation Φ in a zone [h',k',l'] is denoted by;

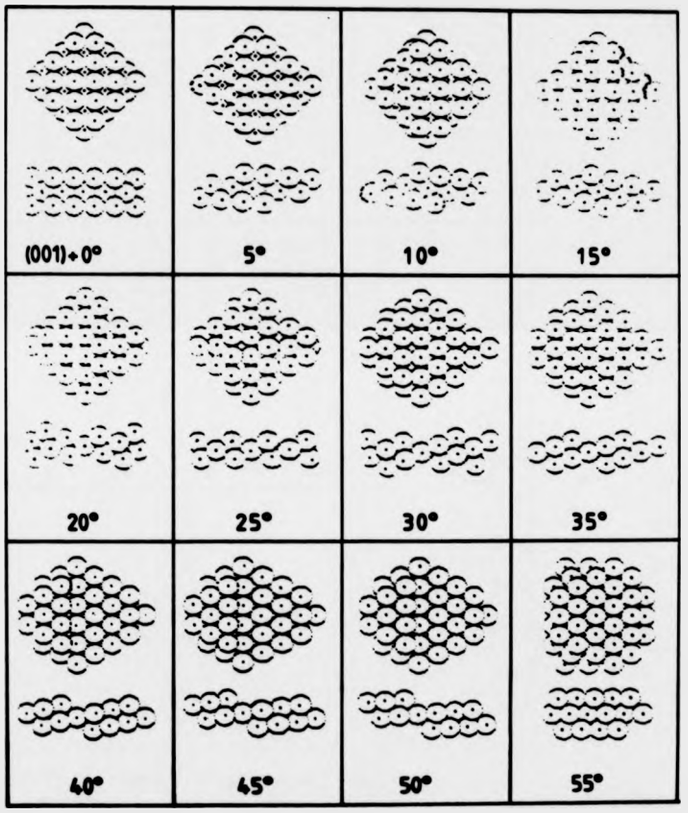

Fig. 4.2a This figure shows all the vicinal planes generated by progressive misorientations of 5° from (001) to (110) around the circumference of the cylindrical single crystal samples. The figure clearly shows the evolution of monatomic steps, and the regular variation of step density with misorientation from (001) in the <110> zone.

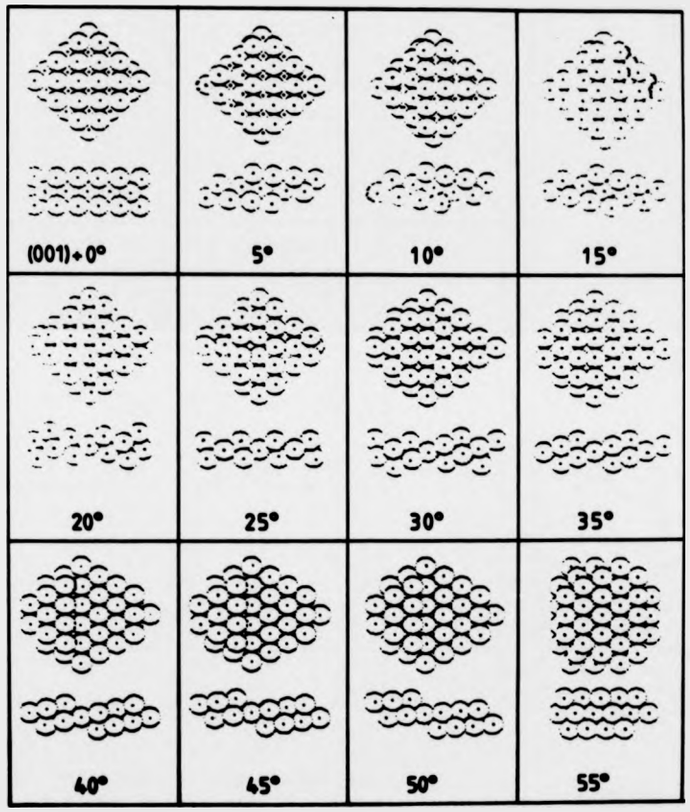

Fig. 4.2a This figure shows all the vicinal planes generated by progressive misorientations of 5° from (001) to (110) around the circumference of the cylindrical single crystal samples. The figure clearly shows the evolution of monatomic steps, and the regular variation of step density with misorientation from (001) in the <110> zone.

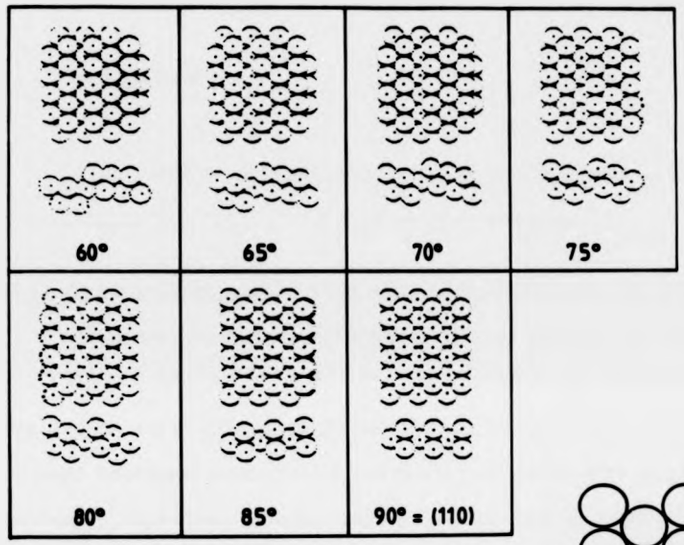

(a)

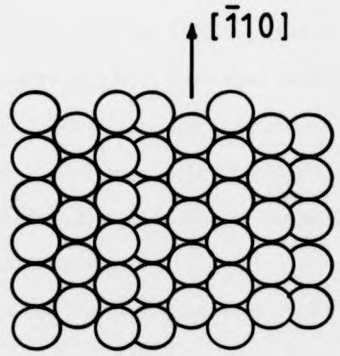

(b)

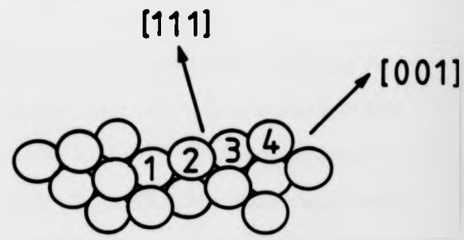

Cu(S) - [4(111)×1(001)]

Fig. 4.2b This figure illustrates the notation of Lang et al[7] for a stepped surface in the <110> zone. The surface has the Miller indices (117).

$$(h,k,l)\otimes^{*}[h',k',l'] \qquad (4.2)$$

This notation is particularly useful for vicinals in any one of the three major zones [00i], [i$\bar{1}$0] or [0i$\bar{1}$] of the stereographic triangle.

(4.7) Crystallographic incident beam effects in AES.

It is well known that Auger emissions exhibit an angular anisotropy that is crystallographic in origin[17]. The effect of this anisotropy on quantitative and semiquantitative AES is small however, as the angular width of the features (at least at high energies) tends to be less than the acceptance angle of the most widely used analysers, and also the adsorbate backscattering is weak. A much more important effect, which has been highlighted by Armitage[18], is the anisotropy in the backscattering coefficient which is dependent on the crystallographic direction of the incident beam. This effect has been known for a long time[19], and has two causes;

(a) the variation of the penetration depth of the incident beam with its direction with respect to the crystal lattice, and

(b) the variation of the intensity of the diffraction pattern of the internal source (Kikuchi pattern) with surface orientation.

The internally diffracted elastically or inelastically backscattered electrons may excite Auger transitions, and this is the mechanism whereby these crystallographic incident beam effects become impressed on the Auger intensities and other secondary electron phenomena. This is illustrated in fig. 4.3 which shows the crystallographic dependence of the crystal current as the nickel sample was rotated through 360° in front of the electron gun. The beam energy was 1.7kV, and the beam was incident at 15° to the sample

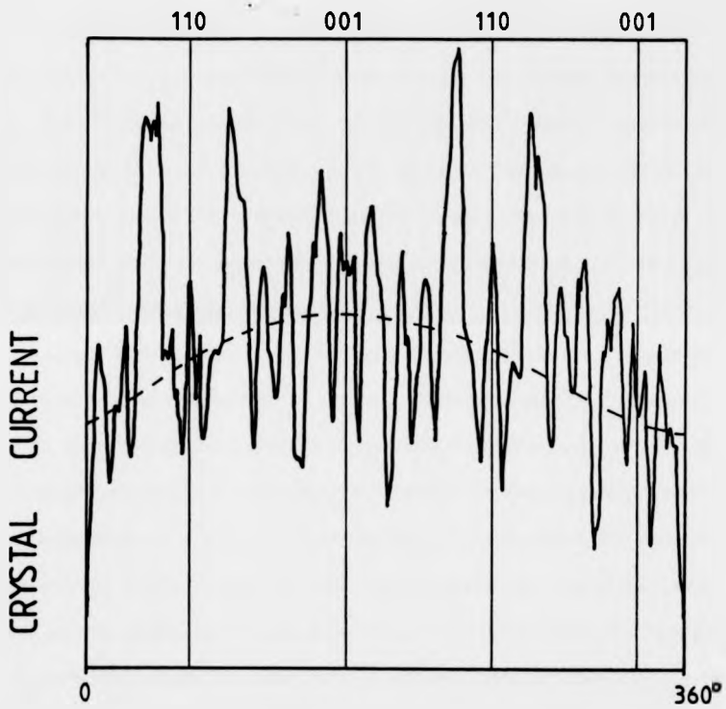

Fig. 4.3 This figure shows the crystallographic variation in the sample current as the cylindrical single crystal was rotated axially in front of an electron beam. The beam was incident at 15° to the sample normal in the plane containing the sample axis, and the beam energy was 1.7kV. The single smooth oscillation of period 360° which is impressed on the data is an artifact due to a slight eccentricity in the sample rotation.

normal in the plane containing the sample axis. Identical patterns were readily obtainable using the copper sample. The data clearly show the 2mm point group symmetry of the sample about it's axis, and were useful in identifying the various crystal planes.

The single smooth oscillation of period 360° which is impressed on the data is an artifact generated by a large eccentricity in the sample rotation, and the figure clearly shows that such effects may be easily separated from the data. These crystallographic incident beam effects have been the subject of two recent investigations by Armitage et al[18] and Gardiner et al[20].

Armitage[2] has shown that for oxygen adsorption on the cylindrical samples used in the current work, variations of up to 15% may be seen in the Auger intensities which are directly attributable to crystallographic incident beam effects. Normalization to a substrate Auger emission (which will also show crystallographic incident beam effects) has been suggested as a way of removing the features which are not coverage dependent, but this tends to either under or over compensate for the effect and is generally not very satisfactory. Gardiner et al, however, have found that for oxygen adsorbed on a <110> axis tungsten cylinder, that the incident beam effects may be removed from the data by normalizing the adsorbate Auger signal to the total exciting electron current at the sample.

In the present work, no attempt has been made to correct the data for these incident beam effects as the variation in the Auger signal due to coverage differences alone was generally much greater than the 15% or so variation due to the crystallographic incident beam effects. Also features due to incident beam effects generally had a much lower angular extent around the crystal circumference than did the coverage dependent effects and so the two effects could be readily distinguished in the data.

(4.8) Preliminary studies of cylindrical single crystal surfaces

The remainder of this chapter is devoted to some preliminary work which was performed on the nickel crystal prior to the computerization of the experiment and the main work which was performed on the copper sample.

(4.8.1) The thermal decomposition of carbon monoxide on the vicinal surfaces of nickel: Previous work.

The interaction of carbon monoxide with nickel surfaces is of great industrial significance, and much work has been done on the system. Araki and Ponec[21] have recently found that the methanation of CO on Ni proceeds via the decomposition of adsorbed CO molecules followed by the hydrogenation of chemisorbed carbon atoms, and so a study of the conditions under which CO dissociates on nickel surfaces has great importance.

The adsorption of CO on the low index planes of nickel has been widely studied, and it is well established that room temperature adsorption on the three low index planes of nickel Ni(001), (111) and (110) leads to a molecularly adsorbed species[22,23,24,25] which is characterized by a single thermally stimulated desorption (TSD) peak (the α state) at about 330K. Onchi and Farnsworth[26] have also observed molecularly adsorbed CO by ultra violet and X-ray photoemission spectroscopies (UPS and XPS). Adsorption at higher temperatures is known to lead to a carbon build up due to the thermal decomposition of CO molecules, and also to additional peaks at higher temperatures in the TSD spectrum which correspond to the associative desorption of oxygen and carbon atoms as CO[25,26]. UPS and XPS have also been used to investigate the interaction of CO with Ni surfaces which exhibit a high density of surface defects[27,28].

Joyner and Roberts[27] have investigated CO adsorption on a polycrystalline nickel film, whilst Eastman et al[28] have investigated CO adsorption on a sputter damaged Ni(111)

surface. Both authors observed molecular adsorption at room temperature, with thermal decomposition occuring at about 300K for the Ni film, and at 350K for the sputter damaged surface.

The conclusion from these results is that surface defects in some way decrease the activation energy for CO decomposition on Ni. Erley and Wagner[29] have verified this by studying the interaction of CO with a stepped Ni(111) surface. The surface studied was inclined at 10.3° to the (111) plane in the [001] zone and had Miller indices (7,9,11). Such a surface may be described as Ni(S)-[5(111)x(110)] in the notation of Lang et al[7] (see section 4.6), and will be fully kinked.

As well as the α state at 330K, Erley and Wagner observed a β_2 state at 700K which was attributed to the associative thermal desorption of carbon and oxygen atoms as CO, where the reaction occured at the step/kink sites. It was already known that associative desorption from the terraces occured at 520K (the β_1 state). The conclusion from this work was that step kink sites lower the activation energy for CO decomposition whilst raising the activation energy for the associative desorption of C and O as CO. More recently, Erley et al[30] have used electron energy loss spectroscopy (EELS) to investigate CO adsorption on the same sample and have found preferential binding on adsorption sites close to the step edges and an exceptionally low frequency C-O stretching vibration which is associated with these sites. This lowering of the C-O bond energy at the step sites is wholly consistent with the lowering in the activation energy for decomposition at these sites which was observed in the TSD experiments.

The work of Erley et al[29,30], whilst clearly demonstrating the special reactivity of step/kink sites, could in no way decide whether the reactivity was confined to the steps, the kinks or indeed to a combination of them both. As the cylindrical nickel single crystal had a zero kink density, it was decided to perform some experiments to investigate

the effects of monatomic steps alone on the decomposition reaction.

(4.8.2) CO decomposition on Ni: Experimental procedure, results and discussion.

The sample was cleaned by argon ion bombardment during continuous rotation (5kV, 1.5μAcm^{-2}) and then briefly annealed to 1000K to re-order the surface. The surface so produced was completely clean except for a small trace (about 0.01 monolayers) of carbon. The crystal was then saturated with CO at room temperature (400L) and heated to about 600K for a few seconds in order to thermally desorb all of the molecular species. This meant that any carbon or oxygen found on the surface on analysis by AES must be isolated C and O atoms generated by thermal decomposition of CO molecules at the step sites.

Initial results looked quite promising in as much as some anisotropy could be seen in the oxygen and carbon signals recorded around the sample after the experiment. The data were not reproducible however, and this was due in part to equipment problems and in part to the rapid contamination of the nickel crystal by carbon. The contamination may well have arisen from the heating of the CO saturated surface causing CO decomposition and diffusion of the resultant carbon atoms into the bulk. High temperature annealing (1000K) in the relatively poor residual vacuum (2x10^{-9} torr) may also have contributed to the contamination by a similar decomposition mechanism as the residual vacuum would certainly contain CO and methane as major components. The Author can provide no concrete explanation for the relatively sudden appearance of such high levels of carbon as those observed in this work as the crystal used had been cut from 99.99% pure Ni and had been found to be largely carbon free by a previous worker[5].

The presence of carbon seemed to prevent the adsorption of molecular CO as no oxygen could be seen on the surface using AES even prior to heating. This was not conclusive evidence that the CO was not sticking however, as it is known that CO interacts strongly with electron beams and perhaps the relatively high beam densities used in the investigation ($1.5\mu Amm^{-2}$) caused electron stimulated desorption of the molecular CO. A raster facility was available for the electron beam, and this reduced the beam density by a factor of 10. Even so, oxygen could not be detected on the surface. The Author thinks it very likely that some oxygen fragments would be seen on the surface due to electron beam cracking of the adsorbed CO even if most of the species were desorbed. It seems then, that the most likely conclusion from the available data is that the levels of carbon contamination observed on the crystal surface were sufficient to completely inhibit the adsorption of CO.

It was found that the surface carbon did not completely inhibit the chemisorption of oxygen, however, and indeed a few oxygen adsorption experiments were performed to test the apparatus. Attempts at sample cleaning using different beam densities and energies followed by anneals to different temperatures and heating in low partial pressures of oxygen were all unsuccessful, and although surface oxygen and sulphur could be readily and reproducibly removed, the carbon contamination remained. It was found that carbon segregated reversibly on heating and cooling, and that sulphur could also be segregated by heating the sample to about 900K for a few minutes. It was decided to conduct an investigation into the behaviour of the impurities in the sample, and this work is described in the rest of this chapter. To summarize this section then, we may say that although the original goal of the CO experiments was not achieved, the importance of carbon contamination in CO adsorption experiments on nickel has been demonstrated.

(4.8.3) Carbon and sulphur segregation in nickel: Previous work.

Mroz et al[31] have investigated the segregation of carbon and sulphur to nickel (111) and (100) surfaces. It was found that carbon segregated reversibly on both (111) and (100) faces, and that the surface carbon concentration decreased with temperature, disappearing at about 770K for (111) and 1070K for (100). In contrast to this, the surface sulphur concentration was found to increase with temperature, reaching a maximum at about 1070K to 1170K. Further heating was found to decrease the surface sulphur concentration, and Mroz et al attribute this to a reversible segregation of sulphur. Mroz et al have also observed that segregation of sulphur, even in sub-monolayer quantities inhibits the segregation of other impurities, including carbon. Indeed, more recently, Ramanathan and Quinlan[38] have found that sulphur coverages in excess of 0.25 monolayers will completely supress carbon segregation to Ni(001).

Blakely and co-workers[14,16,32,33] have conducted a systematic investigation into the segregation of carbon to various low index and vicinal surfaces of nickel, and reference[16] contains a useful summary of this work. Shelton et al[34] and Eizenberg and Blakely[16] have investigated the segregation of carbon to nickel (111) by using specially doped samples (about 0.1 atomic % of carbon). The heat of adsorption of carbon on the nickel surfaces was about 7eV per atom and the heat of segregation was found to be less than 1eV. Carbon monolayer formation was found to occur abruptly as the crystal temperature was raised, the transition temperature depending on the bulk carbon doping level. The carbon monolayer was found to assume the graphite structure, and was epitaxially orientated to the substrate. As well as this graphitic phase, two other phases were identified by Eizenberg and Blakely, a 'condensed monolayer' phase at temperatures greater than T_p (the preciptitation temperature of the graphitic phase) which is characterized

by a carbon coverage invariant with temperature, and at temperatures greater than T_s (the segregation temperature) the 'dilute carbon' phase which is characterized by a low but constant carbon coverage. T_p was found to be about 1000K for a bulk carbon doping level of about 0.15 atomic %, and in the condensed monolayer phase, between T_s and T_p, the carbon coverage was found correspond to 1 monolayer of graphite within the experimental error . The transitions between each phase were found to be quite sharp.

Thapliyal and Blakely[14] have investigated two stepped surfaces in the $[1\bar{1}0]$ zone vicinal to the (111) plane, the (111)5°$[1\bar{1}0]$ plane and the (111)10°$[1\bar{1}0]$ plane. The notation means that the planes are vicinal to the (111) plane and are 5 and 10 degrees respectively from the plane about a $[1\bar{1}0]$ axis (see section 4.6). In the dilute carbon phase, both surfaces exhibited the spot splitting characteristic of monatomically stepped surfaces, but on cooling to the condensed monolayer phase both surfaces were observed to facet to {111} and {110} planes the size of the facets being about 100Å. In the graphite precipitation region, the facets were found to become even more clearly defined. Eizenberg and Blakely have also investigated the segregation of carbon to the (110) face of nickel; the results were very similar to those for Ni(111), and there was no evidence of faceting on slow cooling. Facets of {111} and {513} could be generated if the surface was rapidly quenched to room temperature from the condensed phase, however, and this may be evidence for the existence of facets at high temperatures. Eizenberg and Blakely also found that the segregation of carbon to Ni{110} could not be modeled by a Langmuir isostere.

In the $[01\bar{1}]$ zone, the two vicinals studied by Thapliyal and Blakely were (111)6°$[01\bar{1}]$ and (111)9°$[01\bar{1}]$ and these were found to behave similarly to their counterparts in the $[1\bar{1}0]$ zone. Monatomic steps were observed in the low coverage region with faceting to {111} and {113} in the condensed phase.

In the low coverage region, Eizenberg and Blakely have found that the (113) face is stable, but on cooling to the condensed phase there is evidence for faceting to (111) and (001) and then to (111) only on further graphite deposition. Isett[32,33] has investigated carbon segregation to Ni(100) at low carbon doping levels (about 0.02 atomic % C) and has found in contrast to the Ni(111) work, a steady increase of carbon coverage with decreasing temperature which could be fitted to a Langmuir isostere derived for non interacting atoms restricted to a monolayer, with a saturation coverage of 1 carbon atom to every 4 nickel atoms. Eizenberg and Blakely have also investigated segregation to (100) using a more heavily doped sample, and their results are in good agreement with Isett in the low coverage region.

Several authors have observed a morphological phase transition occuring on clean and carbon contaminated nickel vicinal surfaces. Thapliyal and Blakely[14] report a change in step height and spacing at 360°C and 400°C for Ni(111)10°[1$\bar{1}$0] and Ni(111)5°[1$\bar{1}$0] respectively. Above the transition temperature both surfaces exhibit monatomic steps whilst below the transition temperature the 5° surface exhibits polyatomic steps with a step height distribution centred on 4 to 5 atoms with 100Å terraces. In contrast to this, the 10° surface exhibited diatomic steps. This morphological transition of the clean surface was found to be reversible with temperature, and Thapliyal and Blakely suggest that this phase transition is related to an attractive interaction between steps. Equation (4.3) expresses Herring's[35] criterion for the stability of a vicinal surface to faceting.

$$\gamma(\alpha) = \gamma_s \cos\alpha + \left[\frac{\epsilon}{d_o}\right] |\sin|\alpha| + 1 \qquad (4.3)$$

γ is the surface tension of the vicinal, ϵ_s is the surface tension of the low index plane comprising the terraces, d_o is the step height, γ is the excess free energy per

unit length of the step (which includes the configurational entropy of a set of ledges each with its own distribution of defects), and I is the contribution from the mutual interaction among ledges. Thapliyal and Blakely propose that below the transition temperature there is a strong attractive interaction between the step ledges causing coalescence of the steps whilst above the transition temperature, the attractive force weakens due to the tendency of the distribution of steps to maximize their configurational entropy. On increasing the temperature, the repulsion between steps will drive the surface to a simple unreconstructed monatomically stepped surface described by the simple TLK model. Carbon adsorption tends to increase the attractive interaction between steps and so the surface facets. Eizenberg has found that adsorbed sulphur prevents step coalescence and so it would seem that sulphur adsorption increases the repulsive interaction between steps stabilizing a simple monatomically stepped surface. Jach and Hamilton[15] have also observed this temperature dependent reconstruction of 'clean' nickel (111)5°[01$\bar{1}$] and (111)10°[01$\bar{1}$] surfaces (carbon coverage less than about 0.1 monolayers), and relate it to the paramagnetic/ferromagnetic transition at the Curie temperature (554°C). They do not, however, report such a large reconstruction of the surfaces as do Eisenberg and Blakely, and they describe only small changes in step height and terrace width at the transition temperature. Jach and Hamilton have also performed carbon segregation experiments on the vicinals and on a Ni(111) sample and they find that segregation also occurs at the Curie temperature. As Jach and Hamilton's samples were cut from Marz grade nickel, their bulk carbon concentration was much lower than Eizenberg and Blakely's samples and consequently they did not observe the precipitation of graphite at any temperature. As the segregation temperature of carbon in nickel is known to vary with bulk carbon concentration[16,14,32,33,34], it may be simply fortuitous that in Jach and Hamilton's case segregation happens to occur at the Curie temperature.

By fitting a Langmuir model to the data for the (111) plane and comparing results with those of Eizenberg and Blakely, Jach and Hamilton predict that the heat of segregation to the (111) face is negative below the Curie point and that the change in heat of segregation at the Curie temperature is greater than 0.2eV per atom.

Cinti et al[13] have investigated two stepped surfaces of nickel in the vicinity of the (001) plane; the Ni(S)[5(001)x(111)] and the Ni(S)[3(001)x(111)] surfaces. They find that the [3(001)x(111)] surface reconstructs on slow cooling from 300°C to a morphology similar to that of the unreconstructed surface, except that the periodicity of the steps is doubled. They ascribe this to a two dimensional faceting of the steps in the direction parallel to the step edges. The [5(001)x(111)] surface was observed to show a certain amount of residual disorder on cooling from 300°C, and Cinti et al attribute this to a similar two dimensional step faceting where the facets are uncorrelated between steps. They emphasise that the phase transitions observed could be correlated with neither carbon segregation nor the Curie temperature, and suggest that the driving force for the reconstruction arises from the relaxation of surface electronic states caused by faceting. Whilst it is not possible to prove this hypothesis about the relaxation of surface electronic states, it does seem that surface reconstructions on nickel are not necessarily associated with either carbon segregation or the Curie temperature, although Eizenberg and Blakely have clear evidence that high surface carbon concentrations do indeed lead to extensive faceting. Cinti et al also investigated the behaviour of the vicinals under sulphur adsorption, and in common with other authors, found a stabilization of the 'ideal' TLK morphology.

To summarize this section then, it can be seen that the segregation of carbon to nickel surfaces is associated with several interesting morphological phase transitions. At high temperatures in the dilute carbon phase (low carbon coverage), the surfaces vicinal to (111) may be expected to exhibit their 'ideal' morphology as predicted by the TLK

model. On cooling and precipitating graphite, nickel surfaces facet to (110) and (111) for surfaces in the [1$\bar{1}$0] zone and to (111) and (113) (which may further facet to (001) and (111)) in the [01$\bar{1}$] zone. Clean nickel (111) vicinals in both zones undergo a reversible morphological phase transition close to the Curie temperature which involves a reconstruction to a surface with wide terraces and multiple height steps. Carbon segregation has a tendency to enhance faceting of (111) vicinals, whilst sulphur segregation seems to have a stabilizing effect on monatomic steps. The (110), (113), (001) and (111) surfaces all seem to be stable under carbon segregation but evidence of faceting on quenching (110) and (113) samples from high temperatures may suggest that at high temperatures some faceting does occur. Sulphur segregation on (111) and (001) is found to occur at about 900°C and is found to inhibit the segregation of other bulk impurities. Clean nickel vicinals to the (111) and (001) planes undergo complicated reconstructions on raising the temperature, and it is not at present clear what the driving force for this phenomenon is.

(4.8.4) Carbon segregation in nickel: Experimental procedure.

The carbon segregation work conducted on the cylindrical single crystal of nickel comprised of two distinctly different types of measurement. Thermodynamic measurements were made on the (001) plane of the sample of the variation of the carbon 272eV Auger spectrum peak-to-peak height with temperature, and anisotropy measurements were made of the variation of the carbon Auger signal peak-to-peak height with surface orientation at a given temperature. The sample was cleaned prior to every experiment by a combination of argon ion bombardment for 40 minutes at a beam energy of 5kV and a beam density of about 2 μAcm^2, followed by a brief anneal to about 1000K. The crystal was continuously rotated by hand during the course of the bombardment at a rate of about 30 degrees/

model. On cooling and precipitating graphite, nickel surfaces facet to (110) and (111) for surfaces in the [1$\bar{1}$0] zone and to (111) and (113) (which may further facet to (001) and (111)) in the [01$\bar{1}$] zone. Clean nickel (111) vicinals in both zones undergo a reversible morphological phase transition close to the Curie temperature which involves a reconstruction to a surface with wide terraces and multiple height steps. Carbon segregation has a tendency to enhance faceting of (111) vicinals, whilst sulphur segregation seems to have a stabilizing effect on monatomic steps. The (110), (113), (001) and (111) surfaces all seem to be stable under carbon segregation but evidence of faceting on quenching (110) and (113) samples from high temperatures may suggest that at high temperatures some faceting does occur. Sulphur segregation on (111) and (001) is found to occur at about 900°C and is found to inhibit the segregation of other bulk impurities. Clean nickel vicinals to the (111) and (001) planes undergo complicated reconstructions on raising the temperature, and it is not at present clear what the driving force for this phenomenon is.

(4.8.4) Carbon segregation in nickel: Experimental procedure.

The carbon segregation work conducted on the cylindrical single crystal of nickel comprised of two distinctly different types of measurement. Thermodynamic measurements were made on the (001) plane of the sample of the variation of the carbon 272eV Auger spectrum peak-to-peak height with temperature, and anisotropy measurements were made of the variation of the carbon Auger signal peak-to-peak height with surface orientation at a given temperature. The sample was cleaned prior to every experiment by a combination of argon ion bombardment for 40 minutes at a beam energy of 5kV and a beam density of about 2 μAcm^2, followed by a brief anneal to about 1000K. The crystal was continuously rotated by hand during the course of the bombardment at a rate of about 30 degrees/

minute in order to ensure uniform cleaning. This procedure was found to reproducibly produce a surface on which the only detectable impurity was carbon.

In the thermodynamic experiments, the carbon Auger peak-to-peak height was recorded on the (001) plane of the sample as a function of temperature. Temperatures were measured using a chromel alumel thermocouple spot welded to the top face of the sample, and temperatures were controlled by manually adjusting the stabilized current supplied to the axial sample filament. The thermocouple was clamped between the sample holder and the sample, and so it is suspected that there was a small systematic error in the temperatures measured due to conduction of heat away from the thermocouple by the sample holder. However, it is estimated that the temperatures quoted are accurate to within ±10K. The (001) plane of the sample was located by an examination of the crystal symmetries in the sample current, and it is estimated that the sample was orientated to within ±3° of arc of this plane.

Between measurements of the carbon 272eV Auger peak-to-peak height (of the differentiated spectrum) the sample was held at temperature for a sufficient length of time to allow thermodynamic equilibrium to be attained between the surface and the bulk carbon. The equilibration of the sample was judged to be complete when the carbon signal had reached a constant peak-to-peak height. The time necessary to reach thermodynamic equilibrium varied from a few minutes at the highest temperatures to nearly three hours at the lowest temperature and although the equilibrium between the surface and bulk carbon at a given temperature is reached asymptotically, the Author estimates that all thermodynamic measurements were made at surface coverages within 10% or better of the true equilibrium coverage. The usual methodology for the thermodynamic experiments was to first increase the sample temperature in slow stages whilst measuring the carbon 272eV peak-to-peak heights, and then to repeat the measurements with the sample being slowly

cooled. Coincidence of the two data sets showed that segregation was indeed occuring reversibly. Because of the long times needed to equilibrate at some temperatures, great care had to be taken in order to maintain constant beam currents throughout the course of an experiment.

For an anisotropy experiment, the sample was first cleaned, allowed to equilibrate at the chosen temperature and then the carbon 272eV peak-to-peak heights were recorded at 10° intervals of arc around the sample circumference starting at the (001) plane. As each non-equivalent region of the sample embraces only 90° of arc, this angular sampling frequency is, in fact, rather low. It was decided to measure Auger peak-to-peak heights every 10° of rotation as this was found to give the best compromise between angular resolution, signal to noise ratio and experimental time.

Anisotropy in the segregation of sulphur to the surface was investigated in a similar manner, except that measurements of peak heights were taken every 5° of arc.

The reader should note that the data presented in this chapter were collected manually as the experiments were performed prior to the computerization of the apparatus. Thus, the angular resolution is poorer and the noise level greater than that of the data presented in the later chapters. Also, because of the very long experimental times involved in the anisotropy experiments, no attempt has been made to record simultaneously one of the substrate peaks for normalization purposes.

(4.8.5) Results and discussion.

Fig. 4.4a shows the variation in carbon 272eV peak-to-peak heights measured on the (001) plane (±3°) as a function of temperature. The hollow circles show the data obtained on heating the sample, whilst the filled circles are the data obtained on sample cooling. The carbon peaks recorded throughout this work were noted to have carbidic lineshapes

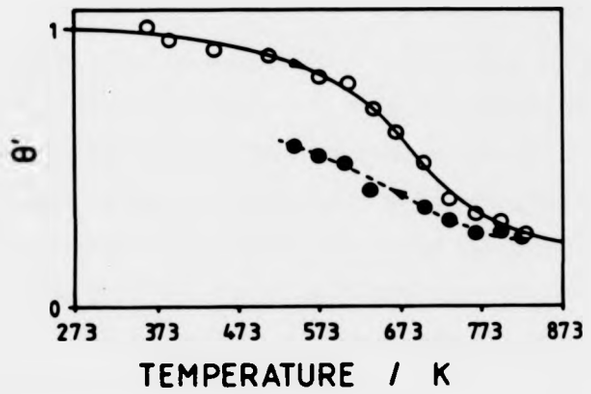

(a)

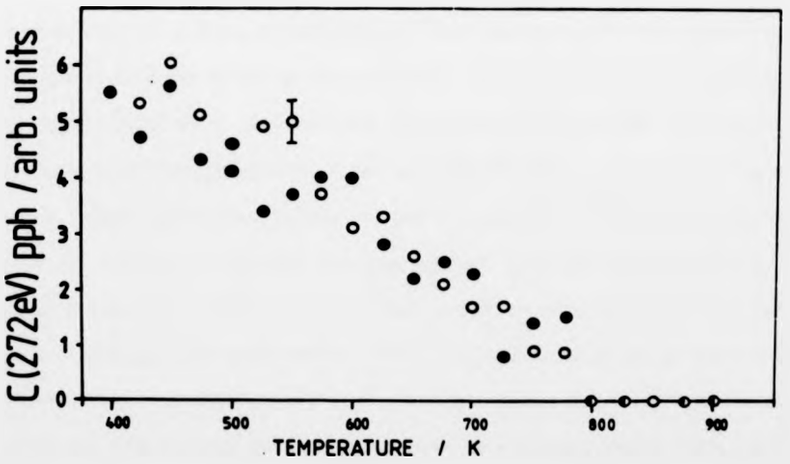

(b)

Fig. 4.4a This figure shows the variation in the carbon (272eV) peak-to-peak height measured on the (001) plane as the sample was first slowly heated (hollow circles), and the slowly cooled (filled circles). The sample was held at 900K for 15 to 20 minutes before being allowed to cool. The 'hysteresis' between the two curves is attributed to site blocking by sulphur which was segregated to the surface whilst the sample was held at 900K. The data have been normalized where $\theta' = \theta/\theta_{sat}$ and θ_{sat} is thought to correspond to 1 monolayer of graphite.

Fig. 4.4b This figure shows the variation in the carbon (272eV) peak-to-peak heights on rapidly heating (hollow circles) and then cooling (filled circles) the sample. Under these conditions (no surface sulphur) the segregation of carbon to the surface is seen to be reversible within the experimental error.

at high temperatures (low coverages) which changed to a characteristically graphitic shape at temperatures less than about 500K. Using the published solubility data for carbon which has been extrapolated to these low temperatures by Isett[32], the bulk carbon concentration must be less than 0.001 atomic %. Comparing the current data with Isett's data for carbon segregation on Ni(001), the Author concludes that high temperatures correspond to what Isett refers to as the dilute carbon phase, whilst at low temperatures the system has made the transition to the condensed monolayer phase where the surface carbon is graphitic in nature.

It can be seen from fig. 4.4a that there is a large 'hysteresis' between the curve corresponding to sample cooling and that corresponding to sample heating. This effect was generated by holding the sample at about 900K for 15 to 20 minutes in order to segregate sulphur to the surface. The difference between the two curves shows clear evidence for the inhibition of carbon segregation by the presence of surface sulphur, and is in good agreement with previous observations[31,36,38]. If the experiment was performed quickly so that no sulphur was segregated, then the segregation of carbon was found to be reversible within the experimental error. Fig. 4.4b shows the results of two 'quick' carbon segregation experiments, and it can be seen that the hysteresis effect is no longer present in the data. Cycling the crystal between high and low temperatures was found to reduce the carbon coverage attained at a given temperature by a small amount as sulphur was segregated to the surface and presumably reduced the number of adsorption sites available to the carbon atoms.

Isett[32,33] has shown that for coverages of less than 1 carbon atom / 4 nickel atoms, the segregation of carbon to Ni(001) can be accurately described by simple Langmuir kinetics. The data of fig. 4.4a have been normalized to the maximum peak-to-peak height observed, and because of the lineshape and the trend of the data (which suggests a

saturation phenomenon at high coverages), the Author concludes that this actually corresponds to approximately 1 monolayer of graphite. The lineshapes of the carbon (272eV) peaks recorded during these thermodynamic experiments clearly indicated a phase change from graphitic to carbidic carbon on raising the temperature. For this reason initial attempts to plot a Langmuir isostere for this experiment were abandoned. Equipment malfunctions prevented the repetition of this experiment at higher temperatures at which the Langmuir isostere could have been applied. The Author feels that a high temperature experiment would have been rather inconclusive anyway, due to the problem of sulphur segregation.

Fig. 4.5 shows the anisotropy in the carbon Auger peak-to-peak heights which have been recorded around the sample circumference at 10° intervals of arc. The data have been normalized at the average peak-to-peak height on the (001) plane at a given temperature to the solid curve drawn through the data of fig. 4.4a.

It can be seen that at low temperatures (T<450K) the carbon coverage is isotropic to within the experimental error. This is consistent with a graphitic monolayer on the faceted surfaces. At higher temperatures, the carbon coverage becomes increasingly anisotropic, exhibiting maxima on the (001) plane and minima in the region of the (110) plane. This suggests that under the conditions of the present work, the (001) plane exhibits a slightly higher heat of segregation for carbon than any of the other planes. The (110) plane would seem to have the lowest heat of segregation. The minima on the (110) planes are rather broad and seem to extend as far as the adjacent (111) planes. The amount of carbon present then seems to increase in an almost linear fashion between (111) and (001) to a maximum on (001), and this is observed to be true even at the highest temperatures where the surfaces can be expected to exhibit their 'ideal' morphologies.

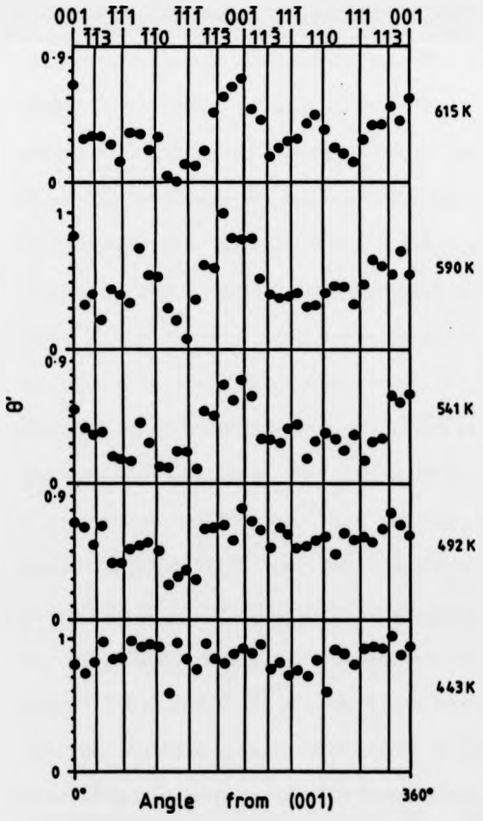

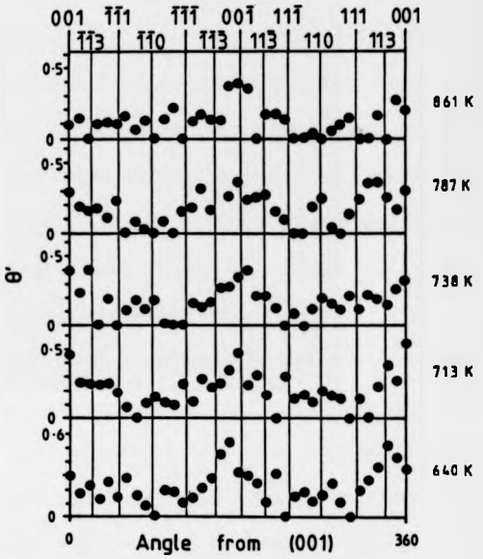

Fig. 4.5 This figure shows the anisotropy in the carbon (272eV) Auger peak-to-peak heights which have been recorded around the sample circumference at 10° intervals of arc. The data have been normalized to the largest carbon peak observed which is thought to correspond to approximately 1 monolayer of surface graphite.

The heat of segregation to nickel surfaces can thus be related to the amount of (001) type surface present in the particular plane under investigation. The Author would like to see further data on carbon segregation to cylindrical single crystal surfaces to test the above conclusion. The difference in heats of segregation which causes the anisotropy in the data is only small (Isett[32] finds (001) and (111) to have heats of segregation similar to within about $1 kJmol^{-1}$), and this shows that studies on cylindrical crystal surfaces provide a sensitive probe for differences heats of segregation.

Fig. 4.6 shows the sulphur 152eV peak-to-peak heights recorded every 5° of arc around the sample circumference. The sulphur was segregated by holding the sample at 1100K for between 10 and 15 minutes, and the data of fig. 4.6 were recorded at this temperature. The carbon coverage at such high temperatures was essentially zero (less than 0.01 monolayers), and sulphur was the only contaminant found on the surface. The experiment was repeated several times at lower temperatures, but there was no noticible change in the sulphur coverage even when carbon began to be precipitated at around 900K. It can be seen that a single smooth oscillation is impressed on the data of fig. 4.6, and this was due to a movement of the sample in the sample holder after many cycles of heating and cooling, which caused it to move off axis and rotate eccentrically. This phenomenon has been discussed in section 3.11, and in no way detracts from the data.

It can be seen from fig. 4.6 that the sulphur coverage is characterized by local maxima on the (110) and (113) planes, with local minima on (001), and somewhat lower minima on (111). The sulphur coverage is seen to vary linearly (within the experimental error) between maxima on the atomically 'rough' (110) and (113) planes to minima on the smooth (001) and (111) planes. There seems also to be some structure on the vicinal planes, but the features are of such a size as to be attributable to the crystallographic incident beam effects known to occur in these experiments.

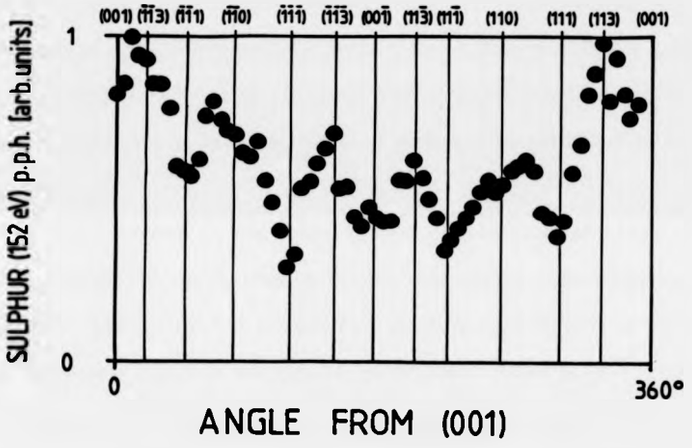

Fig. 4.6 This figure shows the crystallographic variation in the sulphur (152eV) peak-to-peak heights. The peak-to-peak heights were measured around the sample circumference at 5° intervals of arc and the data were normalized to the largest recorded peak-to-peak height. The sulphur was segregated to the surface of the nickel sample by holding the sample at about 1100K for between 10 and 15 minutes.

Rowlands and Woodruff[37] have shown that in the initial stages of segregation, the surface coverage will be limited by the rate of mass transport in the bulk, and so should be independent of crystallographic orientation. Thus, anisotropy such as that seen in the data implies that the surface and bulk sulphur must be very close to thermodynamic equilibrium with eachother. The Author concludes that the anisotropy seen in the data of fig. 4.6 is the result of the equilibration of surface and bulk sulphur, and hence reflects the differing heats of segregation exhibited by sulphur on the various orientations.

All the evidence in the literature suggests that at these high temperatures and with this amount of segregated sulphur, that all the orientations exhibited by the <110> axis cylinder will exhibit a simple TLK morphology. If this is the case, then the step density will vary linearly between adjacent low index planes from maxima on (110) and (113) to minima on (001) and (111) in approximately the same manner as the surface sulphur concentration. Thus it is possible to say that the heat of segregation of sulphur to nickel surfaces varies approximately linearly with step density between (001) and (113), (113) and (111), and between (111) and (110). The heats of segregation of sulphur to the various low index planes planes of nickel may be put in the following decreasing order:

$$(110) \geq (113) > (001) > (111)$$

(4.8.6) Conclusions.

(1) The nickel sample used in the current investigation contained large amounts of carbon which inhibited the adsorption of CO.

(2) The carbon impurity in the sample segregated reversibly to the surface going from the 'condensed monolayer' phase at low temperatures to the 'dilute carbon' phase at high temperatures.

(3) Surface sulphur had an inhibiting effect on carbon segregation on the (001) plane suggesting site competition between the two species.

(4) Carbon exhibits marked anisotropy in its segregation to different crystal planes at temperatures below the precipitation temperature of graphite. The (001) plane seems to have the highest heat of segregation, whilst the (110) plane exhibits the lowest. The vicinals exhibit heats of segregation which vary approximately linearly between these two planes.

(5) Sulphur segregates anisotropically to nickel surfaces at 1000K. The low index planes (110) and (113) have similar heats of segregation, which are also the largest, whilst the (111) plane has the lowest heat of segregation. The (001) plane has a heat of segregation which is intermediate between that of the (110) and (113) planes and that of the (111) plane.

(6) Between adjacent low index planes, the vicinal surfaces exhibit a heat of segregation for sulphur which varies approximately linearly with step density.

(7) Studies on cylindrical single crystals provide a sensitive probe for small differences in heats of segregation.

Chapter 4..... References

(1) Gwathmey A.T., Cunningham R.E., *Advan. Catal.* 9 (1957) p.25.

(2) Armitage A.F., Ph.d thesis, University of Warwick, 1982.

(3) Kossell W., *Nach. Ges. Wiss Gottingen,* (1957) p.135.

(4) Liu H.T., Armitage A.F., Woodruff D.P., *Surf. Sci.* 114 (1982) p.414-430..

(5) Armitage A.F., Woodruff D.P., Vacuum 31 (1981) p.519.

(6) Wagner H., "Springer Tracts in Modern Physics" vol.85 "Solid Surface Physics", Springer-Verlag Berlin, Heidelberg, New York 1979.

(7) Lang B., Joyner R.W., Somorjai G.W., *Surf. Sci.* 30 (1972) p.440.

(8) Lang B., Joyner R.W., Somorjai G.W., *Surf. Sci.* 30 (1972) p.454.

(9) Blakely D.W., Somorjai G.W., *Surf. Sci.* 65 (1977) p.419.

(10) Baetzold R.C., *Surf. Sci.* 95 (1980) p.286-298.

(11) Moison J.M., Domange J.L., *Surf. Sci.* 97 (1980) 1-15.

(12) Domange J.L., Oudar J., *Surf. Sci.* 11 (1968) p.124.

(13) Cinti R.C., Nguyen T.T.A., Capiomont Y., Kennou S., *Surf. Sci.* 134 (1983) p.755-768.

(14) Thapliyal H.V., Blakely J.M., *J. Vac. Sci. Tech.* 15 no.2 (1978) p.600-605.

(15) Jach T., Hamilton J.C., *Phys. Rev. B.* 26 no.7 (1/Oct./82) p.3766.

(16) Eizenberg M., Blakely J.M., *Surf. Sci.* 82 (1979) p.228.

(17) Mc Donnell L., Woodruff D.P., *Surf. Sci.* 46 (1974) p.505.

(18) Armitage A.F., Woodruff D.P., Johnson P.D., *Surf. Sci.* 100 (1980) L483-L490.

(19) Chang C.C., *Appl. Phys. Lett.* 31 (1971) p.181c.

(20) Gardiner T.M., Kramer H.M., Bauer E., *Surf. Sci.* 121 (1982) p.231.

(21) Araki M., Ponec V., *J. Catalysis* (1976) p.439.

(22) Christman K., Schober O., Ertl G., *J. Chem. Phys.* 60 (1974) p.4719.

(23) Erley W., Wagner H., Ibach H., *Surf. Sci.* 80 (1979) p.616-619.

(24) Tracey J.C., *J. Chem. Phys.* 56 (1972) p.2736.

(25) Madden H.H., Ertl G., *Surf. Sci.* 35 (1973) 211.

(26) Onchi M., Farnsworth H.E., *Surf. Sci.* 11 (1968) p.203.

(27) Joyner R.W., Roberts M.W., *J. Chem. Soc.* Faraday Trans. I10 (1974) p.1819.

(28) Eastman D.E., Demuth J.E., Baker J.M., *J. Vac. Sci. Tech.* 11 (1974) p.273.

(29) Erley W., Wagner H., *Surf. Sci.* 74 (1978) p.333-341.

(30) Erley W., Ibach H., Lehwald S., Wagner H., *Surf. Sci.* 83 (1979) p.585-598.

(31) Mroz S., Koziol C., Kolckiewics, *Vacuum* 26 (2) (1976) p.61.

(32) Isett L.C., Ph.d Thesis Cornell University (1975).

(33) Isett L.C., Blakely J.M., *Surf. Sci.* 58 (1976) p.397.

(34) Shelton J.C., Patil H.R., Blakely J.M., *Surf. Sci.* 43 (1974) p.493.

(35) Herring C., Nichols M.H., *Rev. Mod. Phys.* 21 (1949) p.185.

(36) Sickafus E.N., *Surf. Sci.* 19 (1970) p.181.

(37) Rowlands G., Woodruff D.P., *Philosophical Magazine A* (1979) vol.40 no.4 p.459-476.

(38) Ramanathan R., Quinlan M., Wise H., *Chem. Phys. Lett.* 106 no.1,2 (1984) p.87.

(39) Stranski I., *Z. Phys. Chem.* 136 (1928) p.259.

Chapter 5

THE INTERACTION OF OXYGEN AND NITROUS OXIDE WITH COPPER SINGLE CRYSTAL PLANES

Chapter 5..... Contents

(5.1) Introduction to chapter 5.

(5.2) Oxygen adsorption on copper: Previous work.

(5.3) Oxygen adsorption on Cu(111).

(5.4) Oxygen adsorption on Cu(110).

(5.5) Oxygen adsorption on Cu(100).

(5.6) Oxygen adsorption on copper vicinal surfaces.

(5.7) Previous work on oxygen adsorption on the copper cylindrical single crystal.

(5.8) The diffusion free model.

(5.9) The fast diffusion model.

(5.10) Oxygen adsorption on copper cylindrical single crystals: Experimental procedure.

(5.11) Results and discussion.

(5.12) The decomposition of nitrous oxide on copper surfaces: Previous work.

(5.13) Nitrous oxide adsorption on Cu(111).

(5.14) Nitrous oxide adsorption on Cu(110).

(5.15) Nitrous oxide adsorption on Cu(100).

(5.16) Nitrous oxide adsorption on copper: Experimental procedure.

(5.17) Results and discussion.

(5.1) Introduction to chapter 5.

This chapter will describe some experimental work on oxygen adsorption and nitrous oxide decomposition on the copper surfaces made available by the <110> axis cylinder. The oxygen adsorption experiments are essentially a repetition of those conducted by Armitage et al[1,2] and were felt to be necessary as the computerized Auger spectrometer used in this investigation was able to produce data which were markedly superior to anything produced previously on this system. In particular, the scatter on the current data is much less than that of Armitage's data, and also the data have been normalized to a substrate peak which allows quantification. This improved data on oxygen adsorption on the copper cylinder allows the re-evaluation of two models proposed by Armitage and Woodruff[1] for oxygen adsorption on copper vicinals and allows much firmer conclusions to be reached. Indeed, the oxygen adsorption data collected in this work justifies the application of one of the models to a study of CO oxidation over copper which is described in chapter 6.

For the first time, results on the oxidation of the copper cylinder by nitrous oxide are presented and differences between the N_2O/Cu and O_2/Cu reactions are discussed. A simple model is presented which describes the intial reaction probability for the N_2O/Cu reaction. The previous work on the adsorption of oxygen on copper will be reviewed, with a particular emphasis on the expected surface crystallography of the cylinder under oxygen adsorption.

(5.2) Oxygen adsorption on copper: Previous work.

There has been much work done on the copper/oxygen system, particularly on the low index planes, and this work will be summarized in the next few sections.

Habraken et al[3..6] have conducted a systematic investigation into oxygen adsorption on the three low index planes Cu(111), (001) and (110), and this work will be particularly emphasized as it provides a good basis for comparison with the results obtained on the three low index planes in the present work. Armitage[1,2] has also conducted oxygen adsorption experiments on the <110> axis cylinder used in the present investigation, and this work will also be described.

(5.3) Oxygen on Cu(111).

Oxygen adsorption on copper (111) has been studied by many workers; (1..3, 8..11, 53), and this list is by no means exhaustive.

At room temperature Habraken[3] quotes an initial sticking coefficient, s_o, of about 10^{-2}, and this agrees well with values in the range 10^{-2} to 10^{-3} quoted by other workers. The sticking factor was found to be constant up to about half of the saturation coverage of 0.5 monolayers, and could be fitted by the equation of Khort and Gomer[7] for dissociative adsorption requiring a pair of free nearest neighbour sites, and proceeding via a precursor state. The saturation coverage of 0.5 monolayers strongly suggests that the adsorbed oxygen atoms are mobile or else a proportion of the nearest neighbour free sites would be blocked.

LEED investigations show no ordered overlayers on this face for oxygen exposures less than $5x10^4$ Langmuirs[3,8..10], and room temperature adsorption causes no measurable work function change[3]. The lack of a work function change has been attributed by Habraken to the incorporation of oxygen into the bulk. Niehus and Comsa[11] however, have shown by low-energy He^+ ion scattering (LEIS), that no appreciable incorporation into the bulk occurs, and that the surface copper atoms are displaced by 0.3Å with the oxygen atoms probably situated in the surface layer. EELS data by Dubois[53] suggests

that the oxygen atoms occupy the 3-fold hollow sites on the surface.

Habraken[3] has obtained activation energies for the reaction, and finds that the activation energy is about 0.4 kJ/mol for temperatures less than about 230°C increasing to about 1 kJ/mol at temperatures between 230 and 400°C. The initial sticking probability was found to increase with temperature. Armitage[1,2] has found that the initial oxidation kinetics of the (111) face can be quite accurately fitted by a simple zeroth order equation;

$$\theta \propto Es_o \qquad (5.1)$$

where θ is the coverage, E is the exposure and s_o is the initial sticking probability.

(5.4) Oxygen on Cu(110).

The adsorption of oxygen on Cu(110) has been the subject of a large number of investigations using a variety of techniques[1, 2, 4, 12..19]. It is well known that for exposures between 10 and 1000L the (110) surface exhibits a (2x1) LEED pattern, and this is thought to correspond to a coverage of 0.5 monolayers[4,12,13]. Further exposure to oxygen in excess of 1000L gives rise to a c(6x2) LEED pattern which is thought to correspond to the incorporation of oxygen into the lattice and the initial stage of oxidation.

Bronckers and DeWit[14] have investigated oxygen adsorption on Cu(110) using low energy ion scattering, and report that the (2x1) surface is reconstructed and that the reconstruction can be described by the 'missing row' model whereby every row adjacent to an oxygen containing row is missing. In this model the oxygen atoms are thought to occupy the bridge sites in the surface row. Helium beam scattering experiments by Lapujoulade et al[15] also show a reconstructed (2x1) surface which agrees with the missing row model adopted by Bronkers. Lapujoulade also suggests that the adsorption proceeds

by the growth of p(2x1) islands. Feidenhans'l and Stensgaard[16], in a recent high energy ion scattering (HEIS) investigation, find that the best model for the reconstructed (2x1) surface is a 'buckled' (110) surface (a shifted row model) where every second <001> row is shifted outwards from its bulk like position by 0.27±0.05Å, with the remaining <001> surface rows shifted insignificantly inwards by 0.02±0.03Å and the second layer displaced outwards by 0.06±0.03Å. Feidenhans'l and Stensgaard state that although the calculations favour a buckled (110) surface, there may also be a missing row structure which would fit the data. Neihus and Comsa[17] have used impact-collision alkali ion scattering to investigate the reconstructed Cu(110) surface, and have evaluated the missing row model of Bronkers, a shifted row model suggested by Feidenhans'l and Stensgaard and a saw-tooth model. Of the three, Neihus and Comsa state that missing row model is correct.

Dobler et al[18] have recently identified the adsorption site for oxygen on reconstructed (2x1) Cu(110) using surface extended x-ray adsorption fine structure spectroscopy (SEXAFS). The atomic oxygen is found to occupy the low symmetry twofold bridge site in the <001> direction 0.35Å above the first Cu layer. Sesselmann et al[19] in an investigation into the local density of states of copper (110) by the de-excitation of noble gas atoms also provide evidence to support this conclusion. This adsorption site for oxygen is consistent with both the missing row and the shifted row models.

Feidenhans'l and Stensgaard find that the (2x1) structure indicates an absolute coverage of 0.51±0.06 monolayers and that the c(6x2) pattern corresponds to a coverage of 0.90±0.07 and both values are in excellent agreement with those of Habraken[4].

Habraken finds that the formation of the (2x1) structure is accompanied by an increase in work function of between 370 and 420meV depending on the sample temperature. The work function then decreases by about 80meV on forming the c(6x2) structure which may imply incorporation of the oxygen atoms into the surface. The initial sticking factor

for oxygen is about 0.17, and the rate of adsorption is independent of temperature up to coverages of about 0.5 monolayers. Habraken also finds that the kinetics may be described by Langmuir kinetics in which dissociative adsorption occurs into empty nearest neighbour site pairs, and there is an attractive interaction in the adsorbed layer in the <001> direction. Armitage[1,2] has found that Habraken's data may be fitted rather accurately by the simple second order equation;

$$s_0 = \frac{\theta}{cE(0.5-\theta)} \qquad (5.2)$$

where s_0 is the initial sticking coefficient, E is the exposure, θ is the coverage, and c is a constant.

(5.5) Oxygen adsorption on Cu(100).

Oxygen adsorption on Cu(100) is known to progress via a c(2x2) structure at low exposures (which is often referred to as a (√2x√2)R45° structure) to a (√2x2√2)R45° pattern at exposures greater than about 1000L (5). The c(2x2) structure has been analysed by LEED (Onuferko and Woodruff[20]) and the bridge site position was suggested for the oxygen. Kono et al[21-23] however, have determined that the oxygen atom is located in the fourfold hollow (FFH) site with a spacing, d, of zero Å between the oxygen atoms and the first copper layer. A recent normal photoelectron diffraction (NPD) study by Tobin et al[24] favours the fourfold hollow site also, with a d spacing of 0.8Å. Angle resolved secondary ion mass spectroscopy (ARSIMS) studies by Holland et al[25] also favour the fourfold hollow site, but with a d spacing of 1.2 to 1.5Å.

Richter and Gerhart[26] have investigated the c(2x2) structure on spherical copper crystals to obtain a perfect (100) orientation, and conclude from the shape of the LEED

spots that the oxygen actually sits in the bridge site as suggested by Onuferko and Woodruff. However, LEED intensity measurements by Yang et al[27] were found to favour a coplanar FFH site and ab initio cluster calculations by Barker and Batra[28] also favour a FFH site but with a d spacing of 0.9Å. Dobler et al[29] have recently determined the adsorption site using SEXAFS, and find a FFH site with a d spacing of 0.70Å to be the most favourable. In summary then, most recent investigations favour the FFH site with the d spacing of 0.70Å determined by SEXAFS being perhaps the most reliable.

With regard to the (√2x2√2)R45° structure, Tobin et al[24] have evidence that the oxygen atoms also sit in the fourfold hollow site.

Habraken[4] has found the initial sticking coefficient of oxygen on copper (100) to be about 0.01 at room temperature, and has also found that the kinetics of the reaction may be described by Langmuir kinetics where dissociative adsorption occurs into nearest neighbour adsorption sites and the saturation coverage is approximately 0.5. This saturation coverage suggests some mobility of the adsorbed oxygen atoms. The variation of sticking factor with coverage may be described by;

$$s(\theta) = s_0(1-\theta)^2 \qquad (5.3)$$

Armitage[1,2] also finds this relationship to be true, except that the s_0 term must be replaced by a cs_0 term in order to correct for small differences in the initial sticking factor as determined by the two workers.

(5.6) Oxygen adsorption on copper vicinal surfaces.

Gwathmey[30] and co-workers have investigated the oxidation of copper single crystal surfaces in all regions of the stereographic triangle by using spherical copper samples. Copper spheres with (001), (111) and (110) facets were also used so that the behaviour of the low index surfaces could be accurately compared with that of the vicinals. Ellipsometry was used as the analytic technique and film thicknesses could be measured to an accuracy of ±5Å. Because of this limitation, Gwathmey's work could not be extended into the sub-monolayer region and work by Armitage[1,2] and the current work focus on the sub-monolayer regime which was inaccessible to Gwathmey.

Milne[31] has more recently used LEED to investigate clean copper vicinal surfaces 8° and 5° off (110) along [1$\bar{1}$0] and [001] respectively and also a surface 8° off (110) which was 52° from [001]. All surfaces were found to exhibit the simple TLK morphology. Perdereau and Rhead[32] have investigated three surfaces in the [001] zone (all of which exhibit fully kinked steps) 10°,15° and 20° from the (100) pole and has found that all the surfaces facet to (410) after as little as 60L of oxygen at room temperature. This agrees well with the observations of Bernt[33]. Perdereau and Rhead conclude that "*adsorption takes place preferentially at steps, and that the rate of adsorption increases with step density*".

Moison and Domange[34] have investigated all copper vicinals 4° off (100) and (111) under oxygen adsorption and have found that the ~(111) surfaces are stable at room temperature and on annealing. The ~(001) surfaces were also found to be stable at room temperature, and oxygen coverages of up to 1 monolayer. Heating to 400K caused a kink migration and a faceting to (12,1,0) which has fully kinked <100> type steps. Moison and Domange suggest that the driving force for this faceting is the excellent meshing of the superstructure and substrate which is found for (n4,1,0) type surfaces, where n is an integer. Surfaces in the [1$\bar{1}$0] zone (step edges parallel to <110> and zero kink density)

were found to be stable to such faceting.

Baetzold[35] has investigated two stepped surfaces close to (113), the Cu[5(111)x(100)] and the Cu[2(111)x(100)] surfaces. The 2(111) surface was found to be stable to oxygen adsorption up to exposures of 6000L, whilst the 5(111) surface began to facet at around 1000L, and developed into a surface with wide (111) terraces with non regular polyatomic steps at exposures greater than 6000L.

Boulliard et al[51] have used high energy ion channeling to investigate the Cu(16,1,1) surface clean and under oxygen adsorption. The surface was saturated by heating to 300°C in 10^{-5} torr of oxygen, and this caused faceting to a structure exhibiting approximately equal areas of (410) and (100) domains. Boulliard found the saturation coverage to be 0.5 which is in disagreement with all other workers who report a saturation coverage of about 0.75 after only 1000L exposure at room temperature. Boulliard attributes this discrepancy to the faceting of the surface, and points out that if the average of the saturation coverages of (001) and (410) is taken, it is indeed close to the value of 0.5 observed for the vicinal. This result suggests that any faceting of oxygen covered (100) vicinals on heating should manifest itself as a change in surface coverage. It should be noted here that this result is particularly relevant to the work described in chapter 6, where the oxygen covered cylinder is heated to high temperatures prior to reaction with CO.

Lapujoulade et al[52] have recently used helium atom scattering to investigate the effect of temperature on the surface structure of Cu(111), (100), (110), (113), (115) and (117), and have found tentative evidence for a thermal roughening transition at temperatures between 300 and 500K for (110), (113) and the vicinal surfaces. Lapujoulade suggests that this roughening may be attributable to an increase in kink density and to the generation of adatoms on the terraces.

In summary, the Author concludes that the evidence in the literature suggests that for oxygen exposures below 1000L and coverages less than about 0.5 monolayers, all surfaces in the <110> zone will exhibit their simple TLK morphology. This was also the conclusion of Armitage[1,2]. At coverages greater than about 1 monolayer, various faceting phenomena begin to appear, especially for surfaces in the [001] zone with kinked steps. The fully kinked steps in this zone are observed to be particularly susceptible to faceting to (n4,1,0) structures. At much higher oxygen exposures and substrate temperatures, in the oxidation regime, Gwathmey has shown that all copper surfaces facet to combinations of (001) and (111).

As the present work is essentially a repetition under superior experimental conditions of that of Armitage, the previous work on oxygen adsorption on the copper cylinder will now be summarized.

(5.7) Previous work on oxygen adsorption on the copper cylindrical single crystal.

Armitage[1,2] has previously studied oxygen adsorption on the copper cylindrical single crystal used for the present work, in the coverage range 0 to 0.5 monolayers. The most important aspect of Armitage's work, as far as the current investigation is concerned, was the proposal of two models describing the kinetics of oxygen adsorption on the copper vicinal surfaces presented by the [$\bar{1}$10] axis cylinder. Indeed, a major aim of the current work on oxygen adsorption was to re-evaluate these models.

According to Armitage, the vicinal surfaces between two adjacent low index planes in the <110> zone may be thought of as being composed of sections of the adjacent low index planes. The ridged (110) and (113) surfaces are atomically 'rough' surfaces whilst the (001) and (111) planes are atomically 'smooth'. Thus a vicinal surface in the <110>

zone may be thought of as being composed of sections of atomically rough and smooth surface.

Such vicinal surfaces may be viewed in terms of the TLK model as having a step density which varies with misorientation from a low index plane, or, they may equally well be viewed as being composed of low index microfacets. The available evidence in the literature tends to support the TLK interpretation however.

The fraction of a given low index plane A, Ψ_A, in a surface in the <110> zone which is vicinal to A and to another low index plane B, also in the <110> zone is given by:

$$\Psi_A = \frac{(\Phi-\alpha)}{\Phi} \tag{5.4}$$

where α is the misorientation from A about the <110> axis, and Φ is the angle between the two low index planes. Similarly, the fraction of the vicinal surface which is composed of plane B, Ψ_B, is given by:

$$\Psi_B = \frac{(\Phi-\beta)}{\Phi} = 1-\Psi_A \tag{5.5}$$

where β is the misorientation from plane B, and $\alpha+\beta=\Phi$. If A is a rough (110) or (113) surface, then the parameter Ψ_A or $(1-\Psi_B)$, is a measure of the surface roughness, and is linearly related to the step density.

Given this deconvolution of vicinal surfaces into rough and smooth regions, it can immediately be seen that there are two possible extremes of behaviour of the surfaces under adsorption:

(a) The rough and smooth regions of the vicinal (steps and terraces) interact with oxygen completely independently of eachother. In this case the fractional coverage of a given vicinal will be the weighted average of the fractional coverages of its rough and smooth components.

(b) The rough and smooth regions of the vicinal interact completely, with adsorbates from one region rapidly diffusing to the other. This will mean that the sticking factor of a vicinal will be the weighted average of the sticking factors of its rough and smooth components.

Armitage has shown that these two extremes of behavior give rise to two very different models for oxygen adsorption on the copper cylinder. The two models proposed by Armitage, the *fast diffusion* and the *diffusion-free* model will now be described in some detail.

(5.8) The diffusion-free model.

Of the two models proposed by Armitage, the diffusion-free model is by far the simplest. The rough and smooth regions of the vicinal (steps and terraces) are assumed to behave completely independently, and so the coverage of a given vicinal is simply the weighted average of the coverages of its component parts. Thus for a vicinal V between two low index planes A and B, the coverage of the vicinal after an exposure E , $\theta_V(E)$ may be written as ;

$$\theta_V(E) = \Psi_A\theta_A(E) + \Psi_B\theta_B(E) \qquad (5.6)$$

Where Ψ_A and Ψ_B have been defined in the previous section and $\theta_A(E)$ and $\theta_B(E)$ are the coverages of planes A and B respectively after an exposure to oxygen, E. Coverage

has its usual meaning; the ratio of the number of adsorbate atoms to the number of substrate atoms in the plane in question. Armitage has been able to fit Habraken's data for the (110) and (001) planes by simple second order equations of the form,

$$\theta = 0.5 - \frac{0.5}{(KE+1)} \qquad (5.7)$$

The symbol K represents a constant term $c_i s_{oi}$ in Armitage's notation, where s_{oi} is the initial sticking coefficient of the ith plane in question and the constant c_i is chosen so that the exposure E may be in Langmuirs. The constant also improves the fit between Armitage's simplified second order equations and Habraken's data. The values of K and s_{oi} for the low index planes (001), (110), (111) and (113) are given in table 5.1.

Unfortunately, Habraken presents no data for the (113) face, and so Armitage assumed that this face behaves similarly to (110) except that it's initial sticking coefficient s_o, is reduced by the ratio of the ridge densities on the (113) and (110) planes. Armitage found that this assumption gave an excellent fit to data he had obtained for the (113) face, and so was validated. A comparison of the coverages calculated using the above model with data collected in the current work also shows good agreement between the expected and actual behavior of the (113) face. The (111) face obeys simple zeroth order kinetics (for coverages less than 0.3 monolayers), and so the coverage of the (111) face is given by;

$$\theta = KE \qquad (5.8)$$

Where the value of K is given in table 5.1.

Table 5.1 T=298K		
FACE	$s_{o,i}$	K
(110)	0.165	0.571
(113)		0.487
(001)	0.0104	0.0094
(111)	0.00130	0.00034

Table 5.1 This table gives the values of the initial sticking probability, $s_{o,i}$, from Habraken[3..6] and the K values of Armitage[2] for the four low index faces. The K values are used in the fast diffusion and the diffusion free models of Armitage, and the $s_{o,i}$ value for the (113) face is unknown.

(5.9) The fast diffusion model.

In this model it is assumed that surface diffusion occurs instantaneously, and so all parts of the vicinal interact completely. The sticking factor of a vicinal $s_V(\theta)$ is thus given by the weighted average of the sticking factors of its two component low index planes, $s_A(\theta)$ and $s_B(\theta)$:

$$s_V(\theta) = s_A(\theta)\frac{(\Phi-\alpha)}{\Phi} + s_B(\theta)\frac{\alpha}{\Phi} = \Psi_A s_A(\theta) + \Psi_B s_B(\theta) \qquad (5.9)$$

Where the symbols all have their usual meanings.

If the equations for the variation of sticking factor with coverage are integrated (Armitage[2]), then the equation describing the variation with exposure of the coverage of all surfaces except (111) may be written as follows:

$$\theta = \frac{0.5KE}{(KE+1)} \qquad (5.10)$$

Where

$K = c_{(110)}s_{o,(110)}$ for the (110) plane

$K = c_{(113)}s_{o,(113)}$ for the (113) plane

$K = c_{(001)}s_{o,(001)}$ for the (001) plane

$K = \Psi_{(001)}c_{(001)}s_{o,(001)} + [1-\Psi_{(001)}]c_{(113)}s_{o,(113)}$ for vicinals between (001) and (113)

$K = \Psi_{(001)}c_{(001)}s_{o,(001)}$ for vicinals between (001) and (111)

$K = \Psi_{(110)}c_{(110)}s_{o,(110)}$ for vicinals between (110) and (111)

It can be seen that the last two equations are only approximate as no contribution is included from the (111) components. Armitage has found the error introduced by this

to be acceptably small, however, as the (110) and (001) planes have much greater initial sticking coefficients than (111). The (111) plane approximates to zeroth order behaviour at coverages less than about 0.3 monolayers, as described previously (see equation 5.8).

(5.10) Oxygen adsorption on copper cylindrical single crystals:

Experimental procedure.

All the experiments on the oxygen/copper system were performed on the computerized apparatus described in chapter 3. This allowed a decrease in experimental time and, simultaneously, a decrease in the noise in the data which allowed a clarification of the preliminary results of Armitage.

Prior to oxygen adsorption, the copper cylinder was cleaned by argon ion bombardment and annealing. The sample was bombarded with 1keV argon ions for 30 to 40 minutes with a beam density at the sample of about $4\mu Acm^{-2}$. During bombardment the sample was rotated continuously at a rate of about 2 revolutions per minute to ensure even cleaning. Reordering of the surface was accomplished by a brief anneal to about 1000K. This procedure was found to produce clean copper surfaces as judged by AES, but it was found that prolonged annealing at 1000K could segregate small amounts of sulphur to the surface. The ordering of the surface was judged from the sharpness of the crystallographic features seen in a plot of crystal current vs. rotation of the sample (Armitage[36]). This technique will certainly show up gross disordering of the surface, for example after prolonged sputtering.

After annealing, the crystal was allowed to cool to about 50°C prior to oxygen adsorption. Due to the large thermal mass of the sample, cooling to room temperature could take as long as 2½ hours, and so was generally considered to be impractical. Cooling to 50°C could be achieved in about 1¾ hours, and it was found that the sample could

be left in the residual vacuum for well over five hours before any surface impurities began to be detectable. Specimen gas dosing was conducted with the sample rotating to minimize the effect of any directional anisotropies in the influx of gas, and so ensure an equal exposure for all faces.

After sample dosing, the electron gun supplies were adjusted to give a beam current of between 3 and 4μA at the sample at 1.5kV, (the spot size being about 0.25mm^2) and then left for about 20 to 30 minutes in order to stabilize prior to data collection. During this time, the beam was rastered over an area of about 6cm^2 in order to reduce the beam density at the sample and so prevent electron beam damage to the overlayer.

Data collection was performed under computer control by one of the ASPEC programs written specifically for that purpose. Because of noise problems in the spectrometer, quite long time constants had to be used in order to achieve a reasonable signal to noise ratio. Typically, the oxygen peaks were recorded at a rate of 3 seconds/point with 30 points being collected over the whole peak. A high energy copper peak (920eV) could be recorded at the much higher rate of 3ms/point with again, 30 points being recorded over each Auger spectrum. For a complete rotation of the sample, with oxygen peaks being recorded at 5° intervals of arc from 0 to 365°, the data collection time was about 2 hours. Each spectrum was smoothed using a 5 point Savitsky-Golay extended sliding least squares fit (section 3.14), and the peak-to-peak height recorded by the GEC4080 computer. Although it was certainly possible, complete Auger spectra were generally not saved to the cartridge drives in order to conserve space. Habraken has shown that the ratio of the oxygen (503eV) Auger spectrum peak-to-peak height to that of the copper (920eV) spectrum is directly proportional to the surface coverage for coverages below 0.5 monolayers and so no purpose was served by saving the complete Auger spectra.

Each Auger spectrum was displayed on the VDU after digitization so that the operator could check for changes in peak shape or errors in recording. After the recording of the oxygen peak-to-peak heights around the sample circumference, the Cu(920eV) peak-to-peak heights were recorded in a similar manner. Because the simple algorithm used to calculate peak-to-peak heights could not distinguish between an Auger peak and a sloping background, it was found necessary to do a 'clean surface' experiment in which the background in the region of the oxygen peak was recorded around the sample in exactly the same way as the oxygen peaks had been recorded. Both the oxygen peak-to-peak heights and the spurious background were normalized to the orientational average of the Cu(920eV) peak-to-peak heights and the background was subtracted. It was found that the normalization of oxygen and copper peaks on a one to one basis only served to impress the substrate crystallographic incident beam effects on the adsorbate signal (section 4.7), and so normalization to the orientational average of the copper signal was considered to be more appropriate.

(5.11) Results and discussion.

Fig. 5.1 shows the oxygen peak-to-peak heights measured at 5° intervals around the crystal circumference with the background subtracted and normalized to the orientational average of the Cu(920eV) peak. The data have been normalized to a saturation coverage of 0.5 as estimated from fig. 5.2a which is a plot of the variation of normalized oxygen Auger peak-to-peak heights vs. exposure for the four low index planes (001), (111), (110) and (113). These data have been extracted from fig. 5.1 and the average value of the normalized peak-to-peak heights taken at each exposure. This averaging uses the redundancy in the data to good effect, and improves the statistics of the extracted kinetics.

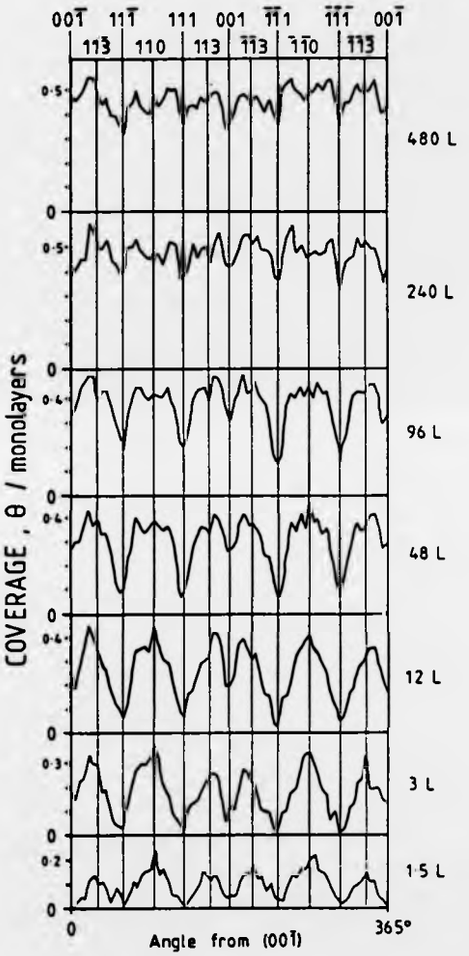

Fig. 5.1 This figure shows the variation with exposure of the oxygen (503eV) peak-to-peak heights recorded at 5° intervals of arc around the sample circumference. These data have been normalized to the orientational average of the peak-to-peak heights of similarly recorded Cu(920eV) peaks at each exposure, and then renormalized to the saturation value at 0.5 monolayers estimated from fig. 5.2a. This normalization procedure is more fully described in section 5.10 p.101.

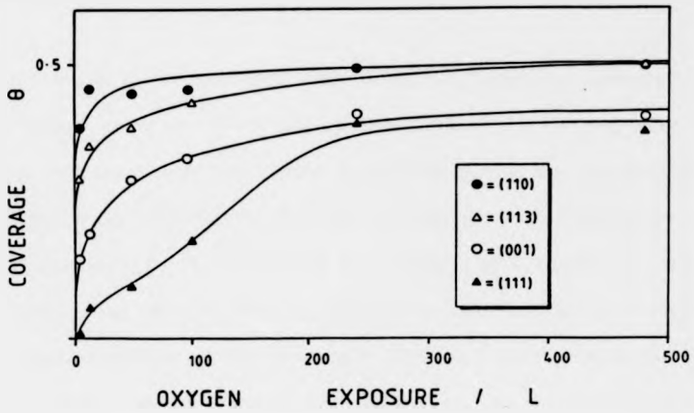

(a)

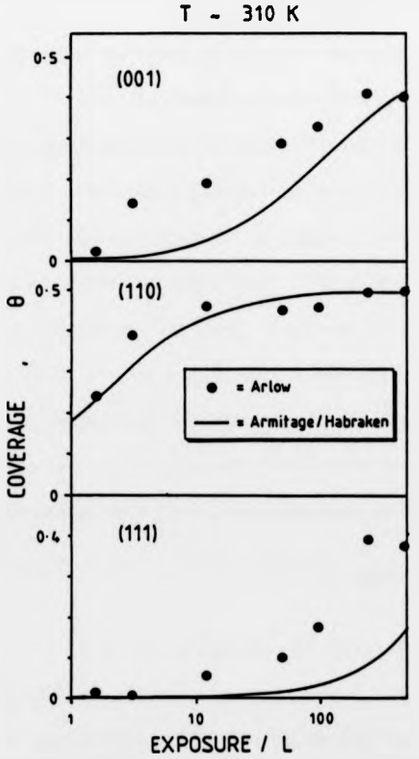

(b)

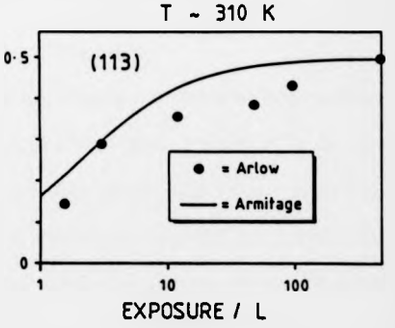

Fig. 5.2a This figure shows the variation in normalized oxygen (503eV) peak-to-peak heights with exposure on each of the 4 low index planes. The data have been renormalized to saturation at θ=0.5 monolayers.
Fig. 5.2b This figure shows the same data as Fig. 5.2a plotted on a logarithmic scale and compared with coverages calculated using the equations of Armitage[2].

Fig. 5.2b shows these same data plotted against log(θ), and compared to Habraken's data as regenerated from the equations of Armitage. It can be seen that the agreement is excellent for the (110) and (113) faces, but rather poorer for the (111) and (001) faces. This result is quite understandable if it is remembered that because of the relatively low angular sampling rate, it is possible to be misorientated by as much as 2.5° from a given low index plane. As the kinetics of the vicinals to (111) and (001) will tend to be dominated by the amount of active 'rough' surface present, any slight misorientation from these planes will have quite a drastic effect on the observed adsorption kinetics. Armitage has previously located all low index planes accurately on the cylinder and has obtained coverage vs. exposure plots in good agreement with Habraken.

Fig. 5.1 clearly shows the large anisotropy in the adsorption kinetics of the various crystallographies available around the circumference of the [$\bar{1}$10] axis cylinder, and the data are wholly consistent with those of Armitage and Habraken; the 'rough' (110) and (113) planes exhibit the highest reactivity whilst the atomically 'smooth' (111) and (001) planes are relatively inert. It should be remembered here, before any further interpretation is placed on the data, that variations in the Auger signal of less than about 15% may not be due to variations in coverage at all, but may be a result of the crystallographic incident beam effects which have been described in section 4.7. The four low index planes may be put in the following decreasing order of reactivity to oxygen adsorption as may be easily seen from a consideration of fig. 5.1 and 5.2a:

(110) > (113) > (001) > (111)

Fig. 5.3 compares the data of fig. 5.1 with the predictions of the fast diffusion and the diffusion free models. It can be seen that whilst both models behave similarly at low exposures, exhibiting an approximately linear variation of coverage with step density

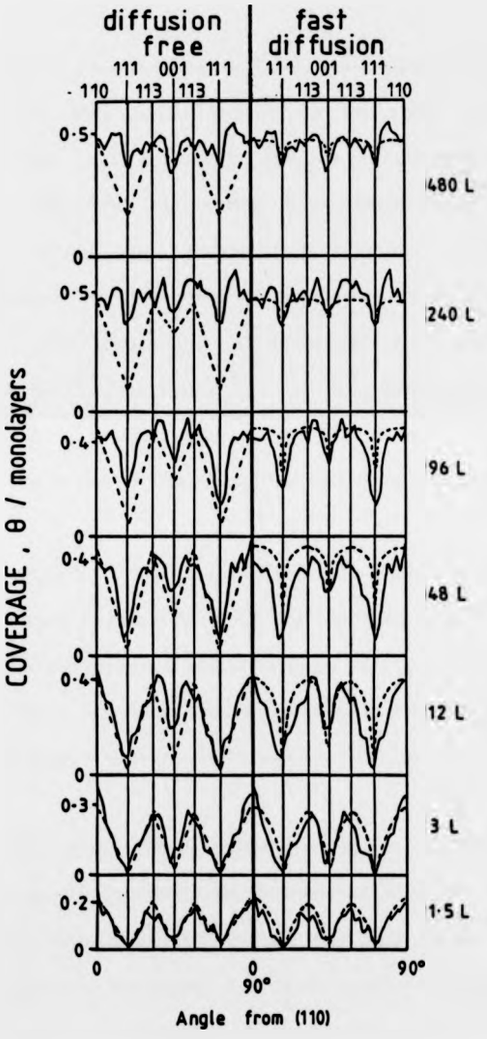

Fig. 5.3 This figure compares the data of fig. 5.1 (solid lines) with the predictions of the fast diffusion and the diffusion free models (dotted lines) of Armitage and Woodruff[1,2]. It can be clearly seen from this figure that at high exposures the fast diffusion model gives the best fit to the experimental data.

in both cases, at higher coverages the fast diffusion model rapidly begins to develop 'cusps' on the smooth (001) and (111) planes whilst the diffusion free model maintains a linear variation between local maxima on the rough (110) and (113) surfaces and local minima on the smooth (001) and (111) surfaces. It should be noted that any cusps in the data will be rounded somewhat, as the angular sampling rate of the data (5° of arc) is substantially greater than the predicted angular width of these features.

The data are in good agreement with both models at coverages less than about 12L, and this is not surprising as there is little divergence between the models at such low exposures. At exposures greater than about 48L however, the fast diffusion model becomes increasingly superior as the data clearly begins to exhibit some cusping at the low index planes.

Examination of fig. 5.1 shows a local maximum developing between the (001) and (113) faces in the exposure range 3 to 480L. This feature is of such a size that it may be attributed to a crystallographic incident beam effect which is known to occur in this region. Although this maximum obscures the data between (001) and (113) somewhat, there still seems to be some evidence of surface diffusion on the (113)/(001) vicinals at high exposures.

It can also be seen from fig. 5.3 that the cusping in the calculated coverages for the fast diffusion model begins to be pronounced at much lower exposures than is the case in the actual data. This discrepancy may well be due to the fact that the model assumes infinitely fast diffusion. Diffusion on the real surfaces will occur at a finite rate, with perhaps some localization of the adsorbate at the active step sites. With regard to the observed surface diffusion, it is unclear whether the diffusing species is actually fully accommodated chemisorbed atomic oxygen, or the 'hot' excited species formed immediately after dissociation of the molecular species.

(5.12) The decomposition of nitrous oxide on copper surfaces:

Previous work.

In contrast to the large amount of work which has been done on the copper/oxygen system, the interaction of nitrous oxide with copper surfaces has received relatively little attention. Spitzer and Luth[41] have used LEED, UPS, XPS, AES and work function measurements to investigate N_2O adsorption on the three low index planes at low temperatures and find that no dissociation or adsorption can be detected on the (100) and (111) planes in the temperature range 90 to 300K. On (110) at 90K, however, N_2O is found to adsorb dissociatively at first, leaving atomic oxygen on the surface. For oxygen coverages above 0.25 monolayers, molecular N_2O is observed on the surface with its molecular axis oriented along the surface normal.

At or above room temperature, Simmons et al[37] and Scholten and Konvalinka[38] have found that N_2O decomposes on adsorption on copper surfaces with the formation of a chemisorbed oxygen atom and a molecule of nitrogen which is desorbed. The LEED patterns of the oxygen overlayers so produced were identical to those produced by the dissociative chemisorption of molecular oxygen[3-6,37-40].

The decomposition of nitrous oxide on copper is found to be very slow on all planes at room temperature, and the process is found to be strongly activated. Even with copper powders, no oxidation of the metal is found to occur at temperatures less than about 120°C, but above this temperature oxidation has been shown to occur at pressures of between 200 and 600 torr (38,40). Ertl[13] has conducted a systematic investigation into the interaction of N_2O with Cu(111), (100) and (110) as has Habraken[3-6]. Habraken's work on the interaction of N_2O with copper (111), (100) and (110) was carried out in conjunction with his work on oxygen adsorption which has been described previously in this chapter.

Habraken's work provided the impetus for the present investigation, and so, because of its great relevance, it will be briefly summarized.

(5.13) Nitrous oxide adsorption on Cu(111).

Habraken et al[3-6] define a reaction probability s(θ) for N_2O decomposition on copper which is analogous to a conventional sticking probability:

$$s(\theta) = \frac{\text{No. adsorbed O atoms}}{\text{No. incident } N_2O \text{ molecules}} \qquad (5.11)$$

For all copper surfaces, the surface reaction is;

$$N_2O \rightarrow O_{ad} + N_2\uparrow \qquad (5.12)$$

Habraken[3] finds that on the (111) plane the reaction kinetics may be fitted by a simple precursor state model where adsorption is to a single site and the reflection probability is independent of coverage (Khort and Gomer[7]). Thus, if $\theta'=\theta/\theta_{sat}$, then;

$$s(\theta') = \frac{s_o}{[1+K_1\theta'.(1-\theta')^{-1}]} \qquad (5.13)$$

where $K_1=P'_d/(P_a+P_d)$ where P_a is the probability of chemisorption and P_d and P'_d, the probabilities for desorption of the precursor state from empty and filled sites respectively. An Arrhenius plot of s_o vs. 1/T gave an activation energy of 43.5 kJ/mol and a pre-exponential factor, A, of 0.09 over the temperature range of 250 to 400°C.

Habraken found that dissociative adsorption of N_2O led to a saturation oxygen coverage of about 0.5 monolayers, and that the initial reaction probability was about

10^{-5} over the temperature range 250 to 400°C. Extrapolated to room temperature, the initial reaction probability is about 10^{-9}. Habraken also found that the reaction probability increased with temperature.

(5.14) Nitrous oxide adsorption on Cu(110).

Habraken et al[4] have found for this plane an initial reaction probability s_0=0.15 (at room temperature) which decreased linearly with coverage to a value close to zero at a coverage of about 0.36. A saturation coverage of about 0.5 monolayers was reached after an exposure of about 10^5L and at temperatures up to 400°C.

The initial reaction probability was found to decrease slightly with temperature, suggesting the presence of a precursor state. The initial activation energy was found to be 8 kJ/mol with a pre-exponential factor of about 0.006, and this activation energy was found to increase with coverage.

Habraken has pointed out that if the decomposition is brought about by the capture of an electron from the substrate as suggested by Lunsford[42] and Gagarin[48], then the activation energy may be related to the work function. Habraken found that the difference in activation energy between the (110) and (111) faces (58 kJ/mol) is approximately equal to the difference in work function between the two faces (52 kJ/mol). A correlation between work function and activation energy is also consistent with the increase in activation energy with coverage, as oxygen adsorption increases the work function of the surfaces.

(5.15) Nitrous oxide adsorption on Cu(100).

At room temperature, Habraken[4] finds an initial reaction probability for the decomposition of N_2O on Cu(100) of 10^{-5}. An apparent activation energy of 13 kJ/mol was found for s_0, and a pre-exponential factor of about 0.001. The reaction probability was found to decrease exponentially with coverage, and the apparent activation energy was

found to increase. Habraken suggests on the basis of this, that a precursor state model is also appropriate to describe the kinetics of the (001) face. Habraken also suggests that the increase in activation energy with coverage is brought about by the increase in work function of the surface.

Engell[43] and Hauffe[44] have derived an equation for the sticking coefficient as a function of coverage for cases where charge transfer over an increasing potential barrier is rate-limiting. Habraken points out that the exponential decrease in sticking factor with coverage observed on the (100) plane is entirely consistent with such a model.

(5.16) Nitrous oxide on copper: Experimental procedure.

The experimental procedure for the nitrous oxide experiments was identical to that used for the oxygen on copper experiments except for the greater pressures (10^{-6} to 10^{-4} torr) used during gas dosing. After the N_2O pressure was established in the chamber (which was continually pumped), the ionization gauge was turned off as it is known[45] that exposure of N_2O to hot filaments leads to the production of NO. The pressure was checked periodically and maintained as accurately as possible over the 5 to 15 minutes taken for the exposures. All exposures were made at temperatures as near to room temperature as was considered practical, typically at about 40 to 50°C.

(5.17) Results and discussion.

Fig. 5.4 shows the variation in the oxygen (503eV) Auger peak-to-peak heights recorded around the sample circumference, which have been normalized to the orientational average of the Cu(920eV) peak, and the 'background' subtracted as described in section 5.10. The saturation coverage of 0.5 monolayers was estimated from fig. 5.5a, which shows the variation in normalized oxygen peak-to-peak heights with exposure for the 4 low index faces, (001), (111), (110) and (113). Once again, the data of fig. 5.5a are the average

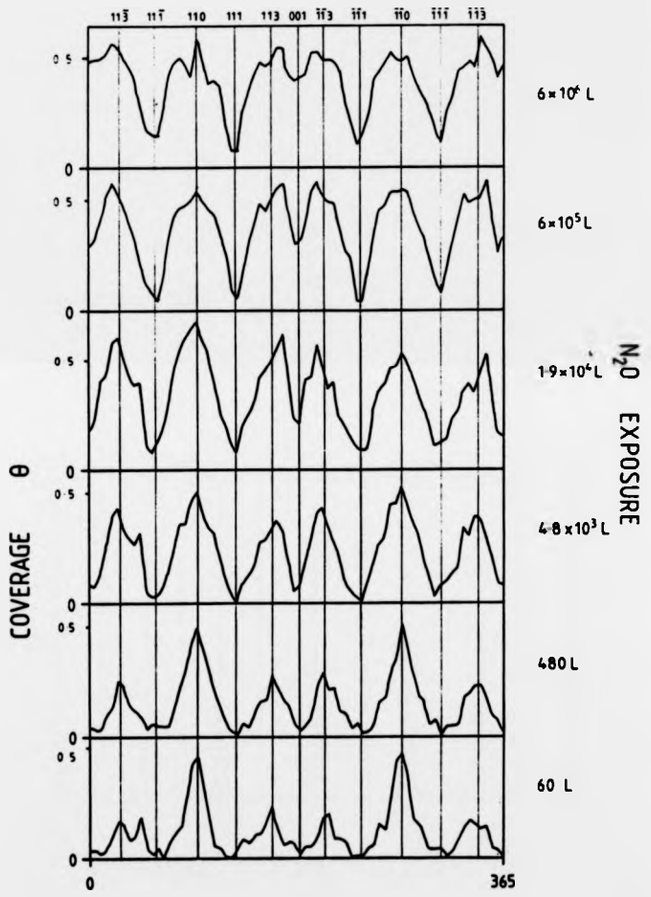

Fig. 5.4 This figure shows the normalized oxygen (503eV) peak-to-peak heights recorded at 5° intervals of arc around the sample circumference as a function of N_2O exposure. The saturation coverage of 0.5 monolayers has been estimated from fig. 5.3a. It can be seen that there is a great similarity between the anisotropy in these data and the anisotropy in the oxygen adsorption data of fig. 5.1 (p.104).

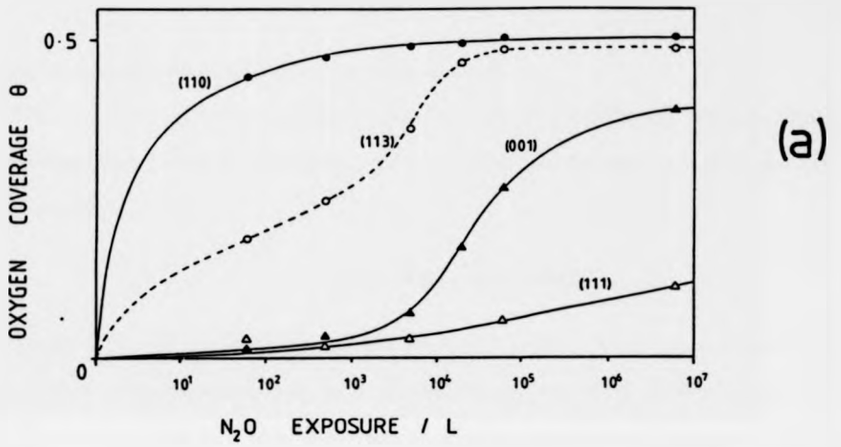

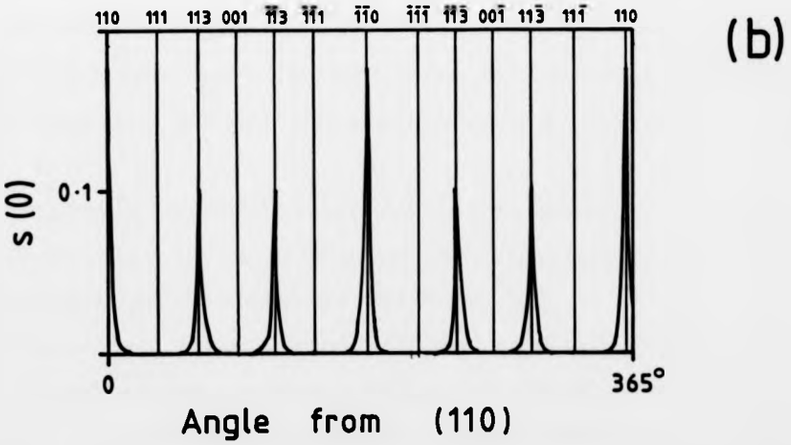

Fig. 5.5a This figure shows the variation of the average normalized Auger peak-to-peak heights on each of the four low index planes with N_2O exposure. This is the first time that kinetic data has been presented for N_2O decomposition on the (113) face of copper.
Fig. 5.5b This figure shows the results of a calculation of the orientational dependence of the initial reaction probability for N_2O decomposition on copper surfaces. The simple 'work function' model used for this calculation is described fully in section 5.17 (p.112).

coverages on a given low index face at a given exposure.

The data of fig. 5.4 once again show a large anisotropy in oxygen coverage at all exposures. The order of reactivity of the faces is the same as that observed for oxygen adsorption;

$$(110) > (113) > (001) > (111)$$

The difference in reactivity between the various faces is much more pronounced than in the case of oxygen adsorption, and indeed, whilst the (110) face is almost saturated at exposures as low as 60L, the (111) face is almost completely inert even at the highest exposure of $6x10^6$L. It is entirely possible that because of the intrinsic angular error of about ±2.5° caused by sampling only every 5° of arc, that the observed reactivity of the (111) plane at room temperature (which seems to be somewhat greater than that predicted by Habraken) is determined by a small step density due to a slight misorientation from (111).

The data of fig. 5.4 and 5.5a include for the first time data on the decomposition of N_2O on Cu(113) and it can be seen that the (113) face exhibits a reactivity which is intermediate between that of the (110) and (001) planes.

If the data of fig. 5.4 are compared with the oxygen anisotropy data (fig. 5.1), it can be seen that there is a great similarity overall, with the activity of the crystal planes decreasing from 'rough' to 'smooth' in the same order in both cases. Closer examination of the N_2O data shows a broadening of the peaks at exposures greater than about $4.8x10^3$L, and this is indicative of surface diffusion. The evidence for surface diffusion is once again somewhat obscured in the region of (001) due to the presence of crystallographic incident beam effects which were seen also in the oxygen adsorption data.

This evidence for surface diffusion in the N_2O data is perhaps to be expected, as the adsorbed oxygen species is the same as that generated by oxygen adsorption. Again it is not clear whether the diffusion occurs for oxygen atoms which are fully accommodated to the surface or whether diffusion is of the 'hot' atoms immediately following dissociation and prior to complete accommodation. If the latter is true, then it can be concluded that the dissociation of either molecule leaves the oxygen sufficiently excited for diffusion to occur.

Comparing the oxygen and N_2O anisotropy data (fig. 5.1 and 5.4), it can be seen that for N_2O decomposition the ratio of the initial reactivity of the (113) face to that of the (110) face is approximately 0.5, whereas in the case of oxygen adsorption, the ratio of the initial reactivities is close to 0.8, the ratio of the ridge densities. This implies that whilst the initial sticking coefficient is obviously dependent on ridge density, the dependence is no longer linear as was found in the case of oxygen adsorption.

Examination of fig. 5.4 clearly shows that at exposures less than about 500L, the maxima in the data are narrower than either the fast diffusion or the zero diffusion models would predict. This 'inverse cusping' of the data would seem to indicate a 'step blocking' rather than a step feeding mechanism, or more appropriately, suggests that the steps are actually less reactive at large separations than when they converge to form a (110) or (113) face. This effect is particularly noticeable in the region of (110), and is strong evidence for a non-linear dependence on step density of the initial rate of N_2O decomposition on the copper vicinals. In fact it is not uncommon for a stepped surface to exhibit a reactivity which has a non linear dependence on step density, and for example CO oxidation over stepped Pt(111) surfaces shows a dependence on step density which is exponential[46].

Habraken[6] has suggested that the activation energy for N_2O decomposition on copper surfaces is related to the work function of the surface as it is thought that the reaction proceeds via a rate determining electron capture from the substrate[42,47,48]. Habraken does indeed find a linear relationship between his calculated activation energies and measured work functions which strongly supports this hypothesis. Peralta et al[49] have measured the work function of a clean copper <110> axis cylinder similar to the one used in the current investigation, and have found that work function may be linearly related to step density, with minima in the work function on the rough (110) and (113) planes, and maxima on the smooth (001) and (111) planes. Peralta's data does exhibit some rounding of both the minima on the (113) planes and maxima on (001), but the effect is small and the variation is essentially linear. Given this information, it should be possible to calculate the variation in activation energy for the dissociation of nitrous oxide as a function of surface orientation, given the work functions of the (113), (110), (111) and (001) faces, and the linear relationships between work function, step density and activation energy. From these activation energies, the initial sticking coefficient may be calculated using Habraken's pre-exponential factors and an estimated pre-exponential for the (113) plane.

The calculation of activation energies directly from work function measurements was tried initially and abandoned as the agreement between published work functions for the low index faces of copper is poor. The Author has, however, constructed a model for the initial reaction coefficient of N_2O on the copper cylinder based on the following three assumptions:

(1) The variation of work function and hence activation energy is linear between two adjacent low index planes in the <110> zone. The activation energy of a vicinal plane E_V, which is between two low index planes A and B with activation energies

E_A and E_B respectively, is given by

$$E_V = \Psi_A E_A + \Psi_B E_B \qquad (5.14)$$

where Ψ_A is the fraction of surface A comprising the vicinal and Ψ_B is the fraction of surface B. The activation energy of a vicinal is thus seen to be the average of the activation energies of its low index components weighted by their respective contributions to the plane. This is an identical assumption to that made for the orientational dependence of coverage in the diffusion free model (section 5.8). The fraction Ψ_A is defined as previously as $\Psi_A = (\Phi-\alpha)/\Phi$ and similarly Ψ_B is defined as $(\Phi-\beta)/\Phi$ where α and β are the angles from faces A and B respectively, and Φ is the angle between the two adjacent low index planes.

(2) In order to construct a model for the initial reaction probability some assumption must be made about the orientational dependence of the pre-exponential factor. It will be assumed that the pre-exponential factor varies linearly in the same manner as the activation energy between any two adjacent low index planes.

(3) Unfortunatly, Habraken does not quote an activation energy or a pre-exponential factor for the (113) face and so some reasonable assumption must be made which will allow estimation of these parameters. In the previous oxygen adsorption work, the (113) face was shown to behave quite similarly to the (110) face, and so it will be assumed that the pre-exponential factors of the two faces are identical. Peralta et al[49] have shown that on both faces the steps exhibit a similar polarization, 2.81×10^6D/cm for (001) type ledges and 3.15×10^6D/cm for (111) type ledges, and so it will be assumed that the (113) face can be treated as a (110) face except that the ridge density is lower by a factor of 0.83. The activation energy to a first

approximation will be taken to be 0.83 times that of the (110) face. That this is a good approximation can be seen by comparing this fraction with the ratio of the work function of (113) face to that of the (110). Using the data of Peralta et al, this ratio of work functions is found to be 0.95, which is within 15% of our original approximation. Given that it is only the qualitative features of this model that are of interest, and that there is probably a much larger error in the pre-exponential factor, it matters little which ratio is used. It was found however, that the ratio of the ridge densities gave better agreement with the experimental data.

Given the calculated activation energies, it it thus possible to calculate an initial reaction probability s_o, where

$$s_o = A\exp\left[\frac{E_a}{kT}\right] \qquad (5.15)$$

where A is the pre-exponential factor, E_a is the activation energy for the face in question, k is Boltzmann's constant and T is the absolute temperature.

Fig. 5.5b shows the result of such a calculation of the orientational dependence of initial reaction probability at a temperature of 298K. The model predicts a marked 'terrace retardation' effect where vicinals to the low index faces exhibit an initial reaction probability which is much lower than that predicted by either the fast diffusion or diffusion free models. A feature of both the fast and zero diffusion models was the clear distinction in terms of adsorption kinetics of the rough and smooth regions of the vicinal surfaces. Unfortunately, with a model based on activation energies, no account is taken of the separate steps and terraces, and the vicinal is viewed as having an initial reaction probability determined by its activation energy which is in some way determined by its

surface structure. This 'averaged' behaviour of the vicinals may be reconciled with the terrace feeding which is believed to be occuring at high coverages if it is remembered that the polarization of the steps will lower the electrostatic potential experienced by the precursor molecule and hence the activation energy to dissociative adsorption. The fact that such a simple 'work function' model successfully predicts a terrace retardation effect is good supporting evidence for Habraken's hypothesis that activation energy depends on work function for N_2O decomposition on copper. It is clear, however, that far more information on the N_2O dissociation reaction is needed in order to understand this terrace retardation phenomenon properly.

Chapter 5..... References

(1) Armitage A.F., Woodruff D.P., *Surf. Sci.* 114 (1982) 414-430

(2) Armitage A.F., Ph.D. thesis, University of Warwick 1982.

(3) Habraken F.P.H.M., Kieffer E.Ph., Bootsma G.A., *Surf. Sci.* 83 (1979) p.45.

(4) Habraken F.P.H.M., Bootsma G.A., *Surf. Sci.* 87 (1979) p.333.

(5) Habraken F.P.H.M., Bootsma G.A., Hofman P., Hachicha S., Bradshaw A.M., *Surf. Sci.* 88 (1979) p.285.

(6) Habraken F.P.H.M., Ph.D. thesis, Rijksuniversitest, Utrecht, 1980..

(7) Khort C., Gomer R., *J. Chem. Phys.* 52 (1970) p.3283.

(8) Ertl G., Kuppers J., *Surf. Sci.* 24 (1971) p.104.

(9) Simmons G.W., Mitchell D.F., Lawless K.R., *Surf. Sci.* 8 (1967) p.130.

(10) Mc.Donnell L., Woodruff D.P., *Surf. Sci.* 46 (1974) p.505.

(11) Niehus H., Comsa G., *Surf. Sci.* 140 (1984) p.18-30.

(12) DeWit A.G.J., Bronkers R.P.N., Hupkens T.M., Fluit J.M., *Surf. Sci.* 90 (1979) (2) p.676-687.

(13) Ertl G., *Surf. Sci.* 6 (1967) p.208.

(14) Bronkers R.P.N., DeWit A.G.J., *Surf. Sci.* 112 (1981) p.133-152.

(15) Lapujoulade J., Le Cruer Y., Lefort M., Lejay Y., Maurel E., *Surf. Sci.* 118 (1982) p.103-120.

(16) Feidenhans'l R., Stensgaard I., *Surf. Sci.* 133 (2-3) (1983) p.453-468.

(17) Neihus H., Comsa G., *Surf. Sci.* 140 (1984) p.18-30.

(18) Dobler U., Baberschke K., Haase J., Puschmann A., *Phys. Rev. Lett.* vol.52 no.16 (1984) p.1437.

(19) Sesselmann W., Conrad H., Ertl G., Kuppers J., Woratschek B., Haberland H., *Phys. Rev. Lett.* vol.50 p.446 (1983).

(20) Onuferko J.H., Woodruff D.P., *Surf. Sci.* 95 (1980) p.555.

(21) Kono S., Goldberg S.M., Hall N.F.T., Fadley C.S., *Phys. Rev. Lett.* vol.41 p.1831 (1978).

(22) Kono S., Goldberg S.M., Hall N.F.T., Fadley C.S., *Phys. Rev. B*, vol.22 p.6085 (1980).

(23) Kono S., Fadley C.S., Hall N.F.T., Hussain Z., *Phys. Rev. Lett.*, vol.41 p.117 (1978).

(24) Tobin J.G., Klebanoff L.E., Rosenblatt D.H., Davis R.F., Umbach E., Baca A.G., Shirley D.A, Huang Y., Kang W.M., Tong S.Y., *Phys. Rev. B*, vol.26 p.7076 (1982).

(25) Holland S.P., Garrison B.J., Winograd N., *Phys. Rev. Lett.*, vol.43 p.220 (1979).

(26) Richter H., Gerhart U., *Phys. Rev. Lett.* 51, p.1570 (1983).

(27) Yang W.S., Jona F., Marcus P.M., *Phys. Rev. B* 27, p.1394 (1983).

(28) Barker J.A., Batra I.P., *Phys. Rev. B* 27, p.3138 (1983).

(29) Dobler U., Baberschke K., Haase J., Puschmann A., *Phys. Rev. Lett.* 52, p.16 (1984).

(30) Gwathmey A.T., Cunningham R.E., *Advan. Catalysis* 10 p.57 (1958). This reference contains a useful summary of Gwathmey's work on spherical and faceted single crystals.

(31) Milne R.H., *Surf. Sci.* 112 no.3 (1982) p.474-490.

(32) Perdereau J., Rhead G.E., *Surf. Sci.* 24 (1971) p.555.

(33) Berndt W., *Z.Naturforsch 22a*, (1967) p.1655.

(34) Moison J.M., Domange J.L., *Surf. Sci.* 97 no.1 (1980) p.1-15.

(35) Baetzold R.C. *Surf. Sci.* 95 (1980) p.286-298.

(36) Armitage A.F., Johnson P.D., Woodruff D.P., *Surf. Sci.* 100 (1980) L483-490.

(37) Simmons G.W., Mitchell D.F., Lawless K.R., *Surf. Sci.* 8 (1967) p.130.

(38) Scholten J.J.F., Konvalinka J.A., *Trans. Faraday Soc.* 65 (1969) p.2465.

(39) Dell R.M., Stone F.S., Tiley F.P., *Trans. Faraday Soc.* 49 (1953) p.195.

(40) Osinga Th., Linsen B.G., van Beek W.P., *J. Catalysis* 7 (1967) p.277.

(41) Spitzer A., Luth H., *Phys. Rev. B* vol.30 no.6 Sept. 1984.

(42) Lunsford J.H., *Catalysis Rev.* 8 (1973) p.135.

(43) Engell H.G., Hauffe K., *Z. Elektrochem* 57 (1953) p.762.

(44) Hauffe K., *Advan. Catalysis* (1955) p.232.

(45) Ku R., Gjostein N.A., Bonzel H.P., *Surf. Sci.* 64 (1977) p.465.

(46) Hopster H., Ibach H., Comsa G., *J. Catal.* 46 (1977) p.37.

(47) Cunningham J., Kelly J.J., Penny A.L., *J. Phys. Chem* 74 (1970).

(48) Gagarin S.G., Kolbanovskii, Yu. A, *Kinetics and Catalysis* 18 (1977) p.744.

(49) Peralta L., Berthier Y., Oudar J., "Surface Physics and Chemistry, gas-solid and liquid-solid interfaces" (1978) Antibes.

(50) Didio R.A., Zehner D.M., Plummer E.W., *J. Vac. Sci. Technol. A* (1984) 2(pt2) p.852-5.

(51) Boulliard J.C., Cohen C., Domange J.L., Drigo A.V., L'Hoir A., Moulin J., Sotto M., *Phys. Rev. B*, 30 no.5 (1984).

(52) Lapujoulade J., Perreau J., Kara A., *Surf. Sci.* 129 (1983) p.59-78.

(53) Dubois L.H., *Surf. Sci.* 119 (1982) p.399.

Chapter 6

THE OXIDATION OF HYDROGEN AND CARBON MONOXIDE BY OXYGEN CHEMISORBED ON COPPER.

Chapter 6..... Contents

(6.1) Introduction to chapter 6.

(6.2) CO adsorption on copper surfaces.

(6.3) Oxygen adsorption on copper: The thermal stability of chemisorbed oxygen films.

(6.4) The oxidation of carbon monoxide by oxygen chemisorbed on copper single crystal surfaces.

(6.5) The oxidation of CO by oxygen chemisorbed on Cu(111).

(6.6) The oxidation of CO by oxygen chemisorbed on Cu(110).

(6.7) The oxidation of CO by oxygen chemisorbed on Cu(100).

(6.8) CO oxidation by oxygen adsorbed on copper single crystal planes: Experimental procedure.

(6.9) Results and discussion.

(6.10) The oxidation of CO in a CO/oxygen gas mixture over copper single crystal surfaces.

(6.11) Results and discussion.

(6.12) The oxidation of hydrogen by oxygen chemisorbed on copper surfaces.

(6.13) Hydrogen adsorption on copper surfaces.

(6.14) The oxidation of hydrogen by oxygen chemisorbed on Cu(110).

(6.15) The oxidation of hydrogen by oxygen chemisorbed on copper surfaces: Experimental procedure.

(6.16) Results and discussion.

(6.1) Introduction to chapter 6.

This chapter describes an investigation into the oxidation of carbon monoxide by oxygen which has been preadsorbed on copper surfaces. This is the first time that this reaction has been studied on cylindrical single crystals, and the reaction is seen to have a crystallographic anisotropy which has not been noted by previous workers. By using the fast diffusion model for oxygen adsorption (described in section 5.9) and empirical equations describing the kinetics of the CO oxidation reaction, the data are extrapolated to describe the crystallographic dependance of the rate of oxidation of CO in a CO/ O_2 gas mixture when copper surfaces are present as a catalyst. The final part of the chapter describes the oxidation of hydrogen by oxygen preadsorbed on copper, and this reaction is compared and contrasted with the previous CO oxidation experiments.

(6.2) CO adsorption on copper surfaces

There has been much work done on the adsorption of CO on copper low index planes and this work will now be briefly summarized.

CO absorbs only very weakly on all copper surfaces at room temperature, and the activation energy for the process is found to be in the range 2 to 4 kJ/mol (Pritchard[1], Conrad et al[2], Kessler and Thieme[3]). At temperatures less than about 200K, various CO superstructures form on the low index copper planes which have been investigated by LEED. On Cu(100) at temperatures of about 80K, a ($\sqrt{2}$x$\sqrt{2}$)R45° structure (usually referred to as a c(2x2) structure) forms at low coverages which develops into a compression structure at higher exposures (Andersson[4,5], Chesters and Pritchard[6], Tracey[7]).

On all crystal planes of copper, infra-red spectroscopy shows that the CO molecule is bonded via the carbon atom, and on the (100) face this bond is to a 'hill site' directly above a Cu atom[5]. Chesters and Pritchard[6] and Andersson and Pendry[5] have found evidence

for the occupation of another site (possibly a bridge site) in the compression phase. At low coverages, CO tends to bond at terminal sites rather than bridge sites on all copper surfaces.

CO adsorption on Cu(111) gives rise to a (√3x√3)R30° structure which is thought to correspond to a coverage of 0.3 and the surface is found to saturate at a coverage of about 0.45 (Lindgren et al[9]).

Woodruff and Bradshaw[10] have investigated CO adsorption on copper (110) and find in common with Horn et al[11] that a c(2x1) pattern is initially produced which compresses at higher exposures to a structure which is approximately c(1.3x2). CO bonds terminally to copper surfaces with it's molecular axis parallel to the surface normal, and this bond is thought to comprise of a strong CO-Cu σ bond which is strengthened by $2\pi^*$ back-bonding from the metal (Blyholder[12]). This backbonding gives rise to a chemical shift in infra-red (IR) absorption spectra, but this effect is complicated by dipole coupling between adsobed CO molecules and also between the molecules and their images in the metal surface[10]. Lindgren et al[9] and McConville et al[13] have investigated this phenomenon on copper (111) and (100) respectively, using photoemission, and find good evidence for the population of the $2\pi^*$ state by back donation from the metal.

Hollins and Pritchard[14] have investigated the adsorption of CO on Cu(111)-O$\begin{vmatrix} \frac{3}{2} & -\frac{1}{2} \\ \end{vmatrix}$, Cu(110)-O(2x1) and Cu(110)-Oc(6x2), and find that in all cases, the heat of adsorption (as inferred from thermal desorption experiments) is lowered. They suggest that for the (111) surface, the CO molecules are bonded to copper atoms which are not bonded directly to oxygen, whilst on the (110) surfaces, the CO molecules bond to copper atoms which are perturbed by bonded oxygen. Hollins and Pritchard also state that CO molecules bonded at step sites exhibit a vibrational frequency which is a few wavenumbers higher than that of molecules at normal sites. It is difficult to say whether this is due to an increased

binding energy at step sites, as the situation is complicated by dipole-dipole interactions.

(6.3) Oxygen adsorption on copper: The thermal stability of chemisorbed oxygen films.

There has been a great deal of work done on the dissociative chemisorption of oxygen on copper surfaces, and this work has been thoroughly reviewed in sections (5.2) to (5.9) of this thesis. With regard to the thermal stability of the resultant oxygen films, it seems that very little work has been done and yet is is necessary for the Author to address this problem as the CO and hydrogen oxidation by chemisorbed oxygen, which is described later in this chapter, occurs only at temperatures greater than about 500K.

Boulliard et al[15] have found that the Cu(16,1,1) surface facets at high oxygen exposures (>100,000L) at 300°C, and that this faceting to regions of (100) and (410) modifies the saturation coverage of the surface. Any change in the surface morphology on heating the oxygen saturated copper cylinder may therefore be expected to be manifest as a change in the observed anisotropy in the oxygen coverage. The Author has investigated this effect by giving the copper cylinder various oxygen exposures up to saturation at θ=0.5 at about 50°C, and then heating the sample. It was found that the chemisorbed oxygen films remained unchanged on annealing to temperatures as high as 1000K. No loss of oxygen or change in the oxygen coverage was observed. On heating to temperatures a few hundred degrees in excess of 1000K, however, it was noticed that oxygen was indeed lost from the surface. After loss of oxygen at high temperatures, the anisotropy in the surface coverage strongly resembled that produced when CO or hydrogen is oxidised by chemisorbed oxygen on copper (section 6.9) and so the oxygen loss was attributed to reduction of the surface by the residual vacuum, which would certainly contain both of these gases.

The Author has also investigated the oxidation of the copper cylinder by N_2O at temperatures up to about 650K. In all cases the anisotropy in the surface oxygen coverage was found to be very similar to that produced at room temperature, and this strongly suggests that no facating had occured.

Lapujoulade et al[16] have some tentative evidence for a thermal roughening transition on copper vicinals at about 500K which results in a non-zero kink density for surfaces in the <110> zone. This thermal roughening may not be a large effect however, and it seems likely that the simple TLK model will be applicable to oxygen covered surfaces undergoing reduction at 600K providing that the surface coverage is only about 0.5 monolayers.

(6.4) The oxidation of carbon monoxide by oxygen chemisorbed on copper single crystal surfaces.

Jones and Taylor[17] have pointed out that copper metal is a very active catalyst for the oxidation of CO to CO_2, a reaction which has some importance in pollution control. The overall reaction is:

$$CO + O_{ad} \rightarrow CO_2\uparrow \qquad (6.1)$$

There has been some work conducted on the oxidation of CO by various types of copper catalyst (Jones[17], Garner et al[18], Smith[19], van der Meijden[20]), but the investigation of the oxidation of CO by oxygen chemisorbed on well defined copper low index planes has recieved relatively little attention.

Ertl[21] has conducted a LEED investigation of the reaction on copper (110), (111) and (100), and this has been followed by a much more detailed LEED, AES and ellipsometry

study by Habraken et al[22,23,24,25]. Habraken's results, which are wholly consistent with those of Ertl, once again form the basis of this investigation. Habraken's results for the oxidation of CO by preadsorbed oxygen on the three low index planes will be summarized in the next sections.

(6.5) The oxidation of CO by oxygen chemisorbed on Cu(111).

Both Habraken[22] and Ertl[21] have found the oxidation of CO by preadsorbed oxygen to be largely non-plane specific on the three low index faces investigated. Thus, the behaviour of the (111) plane is almost identical to that of the other two planes. Habraken has found that chemisorbed oxygen films on copper (111) may be reduced by CO exposures in the 10^4L regime at CO partial pressures of between $5x10^{-5}$ and $5x10^{-4}$ torr and substrate temperatures of 200 to 460°C. The overall reaction (which is the same on all crystal planes) was found to be:

$$CO + O_{ad} \rightarrow CO_2\uparrow \qquad (6.2)$$

where the product, CO_2, was desorbed and was not found to react in any way with the surface. Habraken has found that CO exposures of up to 10^5L produced no adsorption or dissociation on the surface and so it can be seen that the reaction may be monitored by following the surface oxygen coverage either by AES or ellipsometry.

It was also found by Habraken that it was never possible to completely remove all of the surface oxygen by reduction and the final oxygen coverage was estimated to be no less than about 0.004 monolayers. This final coverage was found to increase with many cycles of oxidation and reduction and suggests either oxygen contamination of the CO or the presence of some more strongly bound oxygen species on the surface

which exhibits a resistance to reduction.

Habraken has defined a reaction probability p(θ) for the reaction at coverage θ, where p(θ) is given by

$$p(\theta) = \frac{\text{rate of removal of } O_{ad}}{\text{rate of impingement of CO}} \qquad (6.3)$$

The maximum reaction probability was found to be about 4×10^{-5} at 250°C, and the reaction was found to obey Langmuir-Hinshelwood kinetics with the rate of the reaction being proportional to the CO partial pressure.

Given the assumption of Langmuir-Hinshelwood kinetics, the reaction may be broken down into the following stages.

(1) $O_2 \rightarrow 2O_{ad}$

(2) $CO \rightleftharpoons CO_{ad}$

(3) $CO_{ad} + O_{ad} \rightarrow CO_2\uparrow$ (6.4)

Habraken finds that the activation energy for the overall reaction is 33kJ/mol and given Ertl's value of 42 to 51 kJ/mol for the heat of adsorption of CO on copper (111) (step 2), a value of 75 to 84 kJ/mol was obtained for the activation energy of reaction 3, the oxidation of chemisorbed CO by preadsorbed oxygen.

(6.6) The oxidation of CO by oxygen chemisorbed on Cu(110)

The oxidation of CO by oxygen chemisorbed on copper (110) has been investigated by Habraken[23] over the temperature range 230 to 410°C with an initial oxygen coverage of 0.5. CO partial pressures were between 5×10^{-5} and 5×10^{-4} torr, and exposures in the region of 10,000L were used. Once again it was found to be impossible to completely remove

all traces of oxygen from the surface by reduction with CO. The rate of reaction was found to be proportional to the CO partial pressure, and the reaction was found to obey Langmuir-Hinshelwood kinetics. The maximum reaction probability at 250°C was approximately $3x10^{-5}$, and this corresponded to an oxygen coverage of 0.25 monolayers. Habraken found that the activation energy for the overall reaction was 26kJ/mol and by using Ertl's heat of adsorption for CO (54kJ/mol), an activation energy of 80kJ/mol was obtained for the oxidation of adsorbed CO by adsorbed oxygen.

The similarity in the maximum reaction probabilities at 250°C and the activation energies for the reaction on the (111) and (110) faces illustrates clearly the relative structural insensitivity of this reaction as compared with oxygen adsorption or nitrous oxide decomposition on these surfaces.

(6.7) The oxidation of CO by oxygen chemisorbed on Cu(100).

This reaction has also been studied by Habraken[24], who finds that surfaces with various oxygen coverages may be reduced by exposures to CO in the 10,000L regime at crystal temperatures of between 200 and 400°C and CO partial pressures in the 2 to $8x10^{-4}$ torr range.

As was the case with (111) and (110) a small amount of adsorbed oxygen remained on the surface after reduction by CO. The reaction followed Langmuir-Hinshelwood kinetics with a maximum reaction probability in the 10^{-6} to 10^{-5} range at temperatures between 200 and 400°C.

The activation energy for the overall reaction was found to be about 29kJ/mol, and given Ertl's value of between 42 and 54 kJ/mol for the activation energy for the adsorption of CO on Cu(100), a value of 71 to 83 kJ/mol may be estimated for the activation energy of the oxidation of adsorbed CO by adsorbed oxygen. This reaction (reaction 3,

equations 6.4) is thought by Habraken to be the rate determining step on all faces.

(6.8) CO oxidation by oxygen adsorbed on copper single crystal planes:

Experimental procedure.

The sample was cleaned by the usual method of argon ion bombardment with 1kV argon ions at a beam desity of about $4\mu Acm^{-2}$ for 40 minutes continuous rotation, followed by a brief anneal to about 900K.

After cooling to about 40-50°C, the sample was given an oxygen exposure of about 480L which produced an essentially isotropic oxygen coverage on all faces which was previously found to correspond to about 0.5 monolayers (see section 5.7). The oxygen peak-to-peak heights were recorded around the sample circumference at 5° intervals of arc, and normalized to the orientational average of the Cu(920eV) peak-to-peak heights which were similarly recorded. The spurious 'background' generated by the simple detection algorithm was subtracted, and the data renormalised to a saturation coverage of 0.5 monolayers. This procedure has been described in more detail in section 5.10.

The oxygen saturated sample was then raised to the reaction temperature (570, 610 or 700K) and subjected to increasing exposures of carbon monoxide. The CO exposures were made at pressures of between 10^{-6} and 10^{-5} torr in increments of approximately 12000L up to a maximum exposure of about 90000L.

As up to 9 different exposures were investigated at a given temperature, and the experimental time for each anisotropy experiment was about 2½ hours, it was not possible to investigate all nine exposures by successive CO doses after one initial oxygen saturation. If, for example, CO exposures of 6, 12, 18, 24, 30, 36, 48, 60 and 84L were required, then the data would be obtained in two experiments. The first experiment would be arranged to give cumulative exposures of 6, 18, 30, 48, and 84L whilst the second experiment would

be arranged to give cumulative exposures of 12, 24, 36, and 60L. As the sample was cleaned and re-saturated with oxygen between the experiments the sucessful interleaving of the two separate sets of experimental data was a good test for the reproducability of both the data and the CO exposures. Between each sucessive CO exposure, the oxygen peak-to-peak heights were recorded around the sample and normalized to the orientational average of similarly recorded Cu(920eV) peak-to-peak heights as described previously. During each CO exposure, the required gas pressure was established in the chamber and the ionization gauge turned off. This was a necessary precaution as Habraken has found that the presence of a hot ionization gauge filament can increase the rate of CO oxidation by a factor of two. The gas pressure was checked periodically and carefully maintained throughout the course of each exposure.

(6.9) Results and discussion.

Fig. 6.1a, b and c show the variation in the oxygen coverage around the circumference of the <110> axis cylinder as a function of angle and hence crystallographic orientation after a series of CO exposures ranging from 6000L to 9000L at the three crystal temperatures of 570, 610 and 700K respectively.

It can be clearly be seen from each of these plots, that the oxygen coverage, which was initially isotropic (the small variations may be assigned to crystallographic incident beam effects), rapidly begins to develop marked anisotropy as the different crystal planes express their differing acitvities to reduction by CO.

Consideration of fig. 6.1a, b and c shows that the initial reaction rate increases with temperature as found by Habraken. At 570K, the data exhibits no marked anisotropy for CO exposures less than about 24×10^3L, whilst at the higher temperatures of 610 and 698K, the anisotropy begins to be noticeable at exposures of 12000L at 610K and at rather

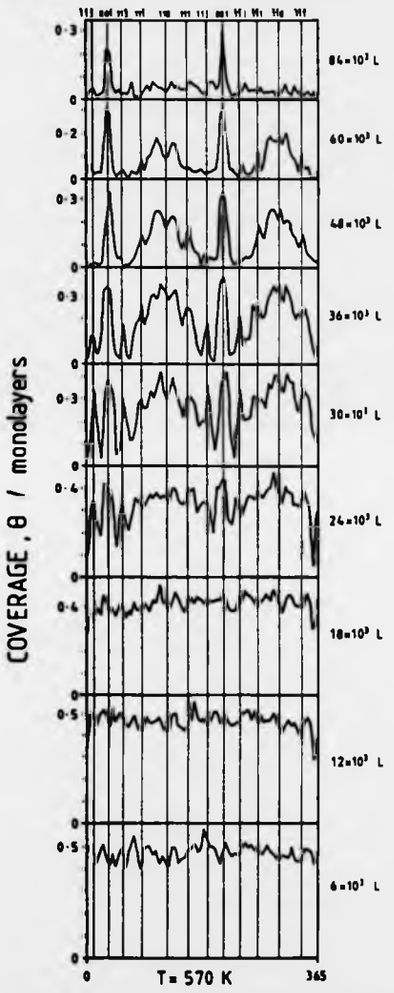

(a)

Fig. 6.1a, b, and c show the variation in the oxygen coverage around the circumference of the <110> axis cylinder as a function of crystallographic orientation after a series of CO exposures ranging from 6,000L to 90,000L at the three crystal temperatures of 570, 610 and 700K respectively. Auger spectra were recorded every 5° of arc around the circumference of the cylinder and their peak-to-peak heights normalized to the peak-to-peak heights of similarly recorded Cu(920eV) peaks. The data were then renormalized to the saturation coverage of 0.5 monolayers. This procedure is more fully described in section 6.8 (p.132).

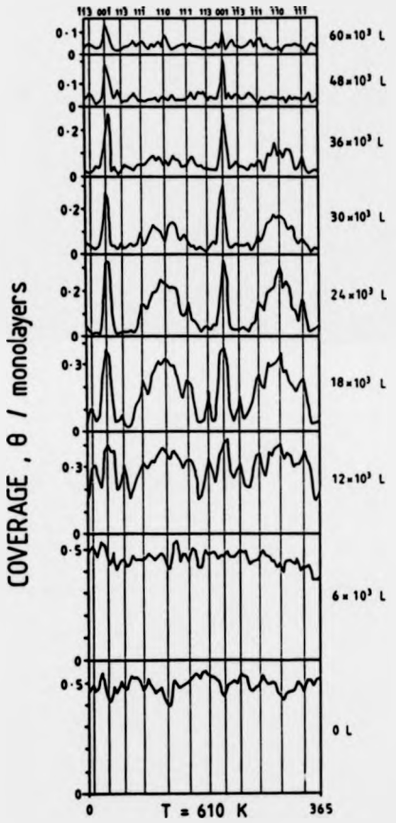
COVERAGE , θ / monolayers
60×10³ L
48×10³ L
36×10³ L
30×10³ L
24×10³ L
18×10³ L
12×10³ L
6×10³ L
0 L
T = 610 K
0
365

(b)

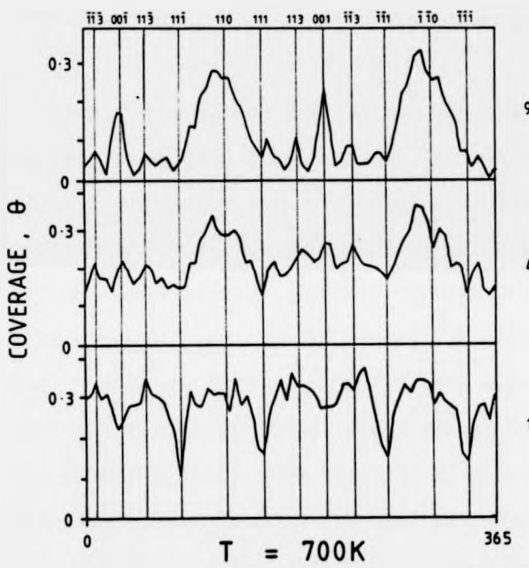
$\bar{1}\bar{1}\bar{3}$ 00$\bar{1}$ 11$\bar{3}$ 11$\bar{1}$ 110 111 113 001 $\bar{1}\bar{1}$3 $\bar{1}\bar{1}$1 $\bar{1}\bar{1}$0 $\bar{1}\bar{1}\bar{1}$
0·3
0
0·3
0
0·3
0
COVERAGE , θ
90 × 10^3 L
45 × 10^3 L
12 × 10^3 L
0
365
T = 700K

(c)

less than 12000L at 700K which was the highest temperature investigated. As these temperatures were accurately maintained by a temperature control unit throughout the course of the exposures, the absolute error in the quoted temperatures is estimated to be about ±5K.

For all temperatures, the anisotropic data are characterized by broad local maxima in the region of (110), sharp local maxima on the (001) planes and rather sharper local maxima on the (113) planes. In contrast to the oxygen adsorption and N_2O decomposition data, maxima in these data indicate a slow, rather than a fast, rate of reaction. Vicinals to (113) roughly midway between (113) and (001) and between (113) and (111) exhibit sharp local minima which indicate a fast rate of reaction. As these vicinal surfaces exhibit an especially high reactivity to reduction by CO, they will be henceforth be referred to as the (113)/(111) and the (113)/(001) planes. Such enhanced reactivity seems to be largely absent from (110) vicinals, although there do seem to be some local minima roughly midway between (110) and (111) at 570 and 610K. These features are so small that they cannot be readily distinguished from crystallographic incident beam effects however.

It can be seen from the data, that although the initial reaction rate increases with temperature, the overall reaction rate increases from 570 to 610K and then decreases markedly at 700K. This is evidenced by the fact that at 700K the surface of the cylinder still has an appreciable oxygen coverage even after a CO exposure of 90,000L. Habraken has investigated the CO oxidation reaction at temperatures up to 730K, and finds that the rate of reduction increases with increasing temperature on all three low index planes. In light of this, it is not clear to the Author why the present data should indicate a ***decrease*** in the overall rate of reaction on raising the temperature from 610 to 700K rather than an increase as expected from the work of Habraken. The 700K data presented here are of noticeably lower quality than the data at either 570 or 610K, and the Author

feels that much more data are neccessary at 700K and higher temperatures before this apparently anomalous temperature dependence can be discussed in detail.

In order to investigate the 'special' vicinals in the region of the (113) face and also to make clearer the relative rates of reaction on different planes at the different temperatures, kinetic data in the form of oxygen coverage vs. CO exposure plots have been extracted from the anisotropy data. These plots for the experiments at 570, 610 and 700K are shown in fig. 6.2. It is clearly seen from this figure that at all temperatures the reaction follows Langmuir-Hinshelwood kinetics as evidenced by the low initial rate of reaction, which is then seen to pass through a maximum before decreasing. Eley-Rideal kinetics would be characterized by a decreasing rate of reaction with decreasing coverage where the inital rate of reaction was the maximum rate. With regard to the Eley-Rideal mechanism, Norton[26] has pointed out that the interaction time in the direct collision of an incident gas molecule with an adsorbed species is too short for product formation to be likely, and it is far more reasonable to envisage the Eley-Rideal mechanism as involving two species on the surface, at least one of which is not in a fully accommodated chemisorbed state. At this point, the distinction between the two processes is far more diffuse. What the current data (and that of earlier studies) shows is that the state in which the CO interacts with the chemisorbed oxygen requires the availability of metal surface sites which are not blocked by the adsorbed oxygen. This would certainly be true of fully accommodated CO, although in view of the fact that CO is only weakly bound to copper surfaces (desorbing in ultra-high-vacuum conditions at around 250K), even this species is highly transient on the surface at the reaction temperatures studied.

In agreement with Habraken, it can be seen that all surfaces still exhibit a small oxygen coverage (about 0.02 monolayers) after the reduction. At all three crystal temperatures studied, the various surface crystallographies may be placed in the following

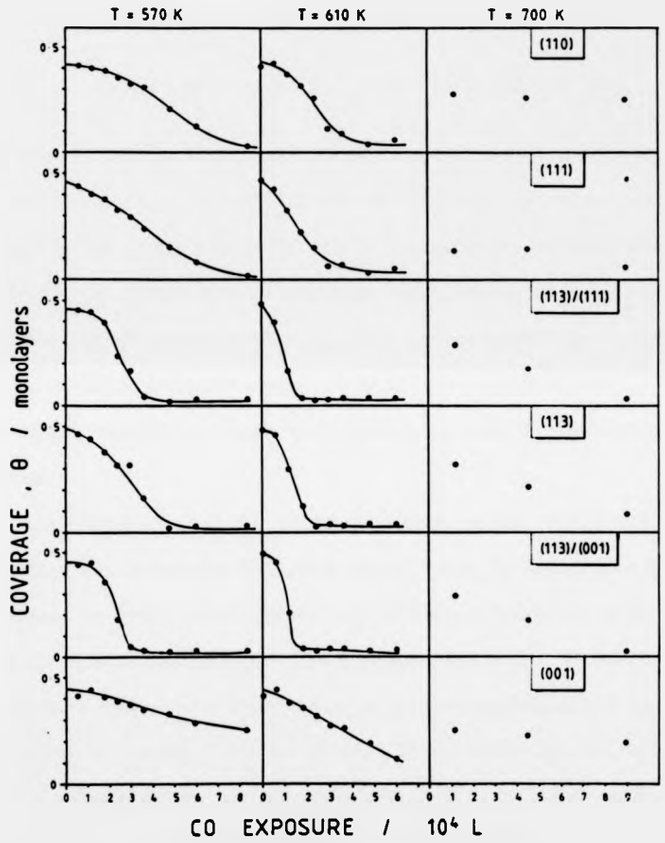

Fig. 6.2 This figure shows coverage vs. exposure plots for the (110), (111), (113)/(111), (113), (113)/(001) and (001) faces. The data have been extracted from the anisotropy data of fig. 6.1 by taking the average coverage for each face at each exposure and temperature. The solid lines drawn through the data at 570 and 610K were drawn by eye and later used to manually digitize the data in order to provide points at equal exposure intervals which allowed the application of a differentiating Savitsky-Golay digital smoothing filter (see fig. 6.3 p.145).

decreasing order of reactivity to reduction by CO:

(113)/(001) > (113)/(111) > (113) > (111) > (110) > (001)

From this it can be seen that the previous correlation of reactivity with surface roughness, which was so sucessful in the description of oxygen adsorption and N_2O decomposition, is no longer valid for the CO oxidation reaction. Indeed, it is now the (113) vicinals which exhibit an approximately equal amount of 'rough' and 'smooth' surface which have the highest reactivity. This leads to two conclusions about the requirements for a high rate of CO oxidation on copper surfaces in the <110> zone:

(a) Roughly equal regions of rough and smooth surface are required ie. both steps and terraces.

(b) Steps of a type found on (113) but not on (110) increase the rate of reduction.

Obviously, the available data are insufficient to allow the establishment of a reaction mechanism which accounts for all of this structural sensitivity. Nevertheless, much is known about chemisorbed CO and atomic oxygen on the low index faces of copper which supplements the data presented here. In particular, CO is known to prefer top sites on all three low index faces (with the CO perpendicular to the surface and bonded through the carbon end of the molecule) except at very high coverages. In general, atomic oxygen adsorbed on metal surfaces seems to adopt the highest available coordination sites; four fold hollow for Cu(001), threefold hollow for Cu(111) and a long bridge site for the reconstructed Cu(110) (see section 5.3-5.5).

In view of the preference which oxygen seems to display for high coordination sites, it seems likely that on a surface containing both steps and terraces, the chemisorbed oxygen would preferentially adopt the high coordination sites available at the bottom of the steps. By contrast, the adsorbed CO molecule might be expected to preferentially

adopt the top sites at the top of the steps and indeed Pritchard[1,8] has found a shift in vibrational frequency in the IR spectra of CO on (110) vicinals, (211) and (311), (755) and also on defect sites on (111) which is associated with step sites and which may be due to an increase in the binding energy of the molecule (see section 6.2). This leads one to the rather attractive, if simplistic, picture of the formation of the linear CO_2 species at step sites with the CO and O atoms approaching eachother in the appropriate geometry. Moreover, this picture only works if there are at least small terraces between the steps; if the (110) face is regarded as a "fully stepped" surface, it can be seen that the steps have become so close together that the oxygen atoms can no longer sit in the hollows, and in fact, sit above the hollows in the long bridge sites. Indeed, it is possible that the greater reactivity of the (113) face relative to the (110) face is in this case due to the larger ridge spacing which allows the oxygen atoms to fit down into the hollows. Another reason for the particularly low reactivity of the (110) surfaces however, may be the oxygen induced reconstruction of these surfaces which may well kinetically hinder the oxidation reaction. Moreover, if the widely accepted missing row reconstruction model for the Cu(110)(2x1)-O structure is considered, the rows of oxygen atoms above the top rows of copper atoms are separated by rows in which the top copper atoms are removed, leaving only sites well below the oxygen atoms for possible CO accommodation.

A similar argument can be seen to be applicable to the "buckled surface" model as the oxygen atoms also occupy the 2 fold bridge sites which are situated above the possible adsorption sites for CO. Insofar as the simple geometrical argument which has been applied to step sites is of value, it can be seen that the geometry offered by the reconstructed (110) surface is particularly unsuitable for the formation of carbon dioxide.

(6.10) The oxidation of CO in a CO/oxygen gas mixture over copper single crystal surfaces.

When CO is to be catalytically oxidised to CO_2 in industry, a mixture of CO and oxygen is exposed to a copper catalyst. The overall reaction is;

$$CO + \tfrac{1}{2}O_2 \rightarrow CO_2\uparrow \qquad (6.5)$$

When a CO/O_2 gas mixture is oxidised over copper single crystal surfaces, then the above reaction may be broken down into several more fundamental steps as described in section 6.5.

(1) $\tfrac{1}{2}O_2 \rightarrow O_{ad}$

(2) $CO(g) \rightleftharpoons CO_{ad}$

(3) $CO_{ad} + O_{ad} \rightarrow CO_2(g)\uparrow$ (6.6)

Step 3 assumes Langmuir-Hinshelwood kinetics. If both gases are in great excess, then the above series of reactions will rapidly reach a steady state where the rate of adsorption of oxygen is equal to it's rate of removal by CO, and the surface oxygen coverage remains constant. Whilst such a reaction is obviously of interest, its investigation is experimentally difficult, especially so on cylindrical single crystals.

Fortunately, this 'steady state' reaction may be investigated theoretically by extrapolating the data previously obtained for oxygen adsorption on copper and the oxidation of CO by chemisorbed oxygen films. If $d\theta/dt$ vs. θ curves are obtained from both sets of data, then assuming the CO molecules do not block the oxygen atoms (and there is no evidence that they do), the intersection of the two curves will give both the stationary oxygen coverage and the corresponding rate of reaction. Thus both the

important parameters of the steady state reaction may be calculated.

Consider the kinetic data of fig. 6.2 at 570 and 610K. Smooth curves have been drawn through the experimental points by eye, and the curves manually digitized and then differentiated with respect to exposure by using a Savitzky-Golay extended sliding least squares fit adjusted to differentiate as it smooths. It should be remembered that these differentiated curves may be expressed in terms of $d\theta/dt$ rather than $d\theta/dE$ by using the definition of exposure, E:

$$E = P.t \tag{6.7}$$

and,

$$dE = Pdt \tag{6.8}$$

If the pressure P, is in μtorr ($1\mu torr = 10^{-6} torr$), the exposure E, is in Langmuirs ($1L = 10^{-6}$ torr for 1 second) and the time t, is in seconds, then division of $d\theta/dE$ by the pressure in μtorr will give the rate of reaction ($d\theta/dt$) in monolayers s^{-1} at that pressure.

The differentiated data were modeled by third order polynomials, fitted by the method of least squares, in order to obtain simple analytic forms which described the data rather accurately. A single equation may then be written which, with different coefficients, describes the rate of removal of adsorbed oxygen, $-d\theta/dt$, on all faces.

$$-\frac{d\theta}{dt} = P(a\theta^3 + b\theta^2 + c\theta + d) \tag{6.9}$$

Where once again, P is in μtorr, and a, b, c and d are the coefficients of the polynomial as determined from the least squares fit.

Fig.6.3 shows the smoothed and differentiated experimental data (black circles) along with the fitted polynomials (smooth lines) for the (001), (111), (113), (110) low index faces and the (113)/(001) and (113)/(111) vicinals at the two temperatures, 570 and 610K. The coefficients of the polynomials which describe the kinetics of the various faces are given in table 6.1, along with the coefficient of correlation of the fit in each case. It can be seen that the fits are good even for the worst case of the (001) plane at 610K. It can also be seen that the errors introduced by this procedure are small compared to the experimental errors. The data at 700K were not treated in this manner however, as they are noticeably inferior to those collected at the lower temperatures.

No data are available for oxygen adsorption on the <110> axis cylinder at 570 and 610K, but it has been shown in chapter 5 that the kinetics of adsorption on the cylinder may be approximated reasonably accurately by the 'fast diffusion' model of Armitage[27]. Habraken[22..25] has investigated the temperature dependence of the initial sticking coefficient of oxygen on the three low index faces (001), (111) and (110), and by assuming zero temperature dependence for the (113) face (behaviour similar to (110)), the model may be extrapolated to the temperatures of interest. Armitage's equations for the variation of surface coverage, θ, with exposure, E, for the (001), (113), (110) low index faces and the (113)/(001) and (113)/(111) vicinals may all be written as below.

$$\theta = \frac{0.5EK}{(EK+1)} \qquad (6.10)$$

For the (111) plane, the equation is different:

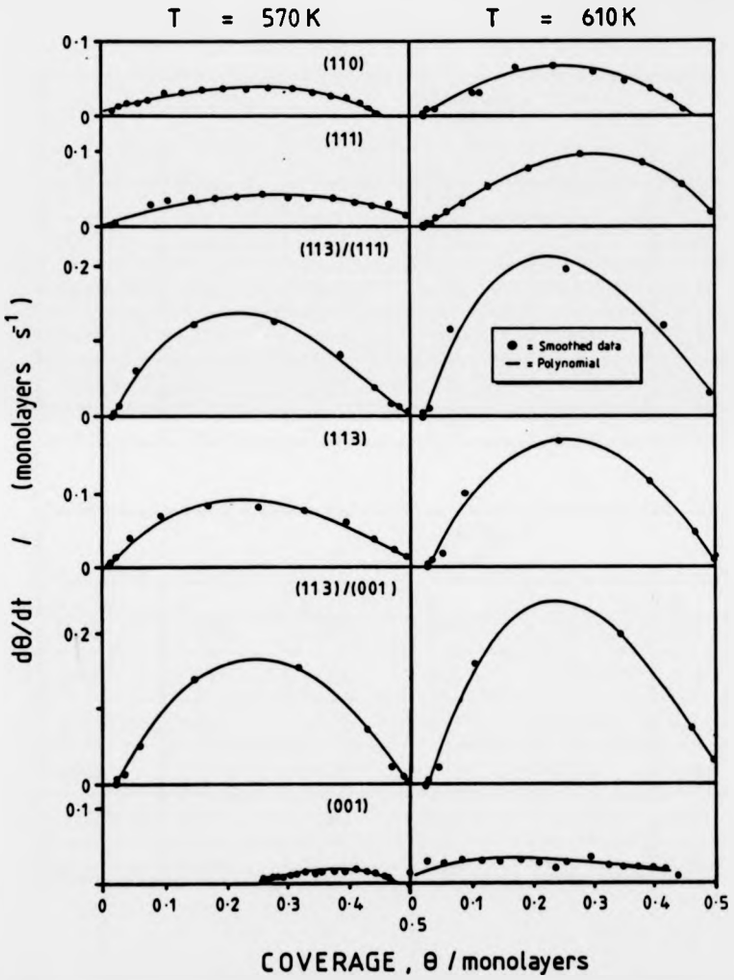

Fig. 6.3 This figure shows the smoothed and differentiated digitized experimental data (black circles) along with third order polynomials (smooth lines) which have been fitted by the method of least squares. The coefficients of the polynomials and the coefficient of correlation of the fit in each case are given in table 6.1. This procedure allows the differentiated experimental data to be accurately described by simple equations of the form:

$$d\theta/dt = a\theta^3 + b\theta^2 + c\theta + d$$

In this case dθ/dt refers to the rate of removal in monolayers/second of chemisorbed oxygen from the surface by CO.

Table 6.1 a 570K						
FACE	a	b	c	d	K	R
(110)	-0.790	-0.125	0.216	0.00563	0.59	0.99
(113)	1.81	-2.74	0.972	-0.0117	0.48	0.99
(001)/(113)	1.23	-3.90	1.73	-0.0399	0.255	0.99
(001)	-6.53	6.12	-1.78	0.168	0.030	0.85
(111)/(113)	3.70	-5.16	1.73	-0.0310	0.24	0.99
(111)	-0.146	-0.395	0.262	0.00218	0.0011	1.0

Table 6.1 b 610K						
FACE	a	b	c	d	K	R
(110)	-0.357	-1.01	0.576	-0.00109	0.59	0.97
(113)	1.57	-4.22	1.85	-0.0505	0.48	0.99
(001)/(113)	4.84	-7.92	2.97	-0.0802	0.26	0.99
(001)	1.34	-1.29	0.329	0.0088	0.033	0.79
(111)/(113)	5.64	-7.83	2.68	-0.0572	0.24	0.99
(111)	-1.96	0.0299	0.532	-0.0115	0.0012	1.0

Table 6.1 This table lists the coefficients of θ generated by a least squares fit of equation 6.9 to the differentiated dθ/dt experimental data at the two reaction temperatures of 570 and 610K. The parameter R, is the coefficient of correlation of the fit in each case.
Also presented in this table are the K values for equations 6.15 and 6.16 which have been extrapolated from the $c_i s_{o,i}$ values of Armitage[27] using the temperature dependence curves of Habraken[22..25].

$$\theta = KE \tag{6.11}$$

The K values are derived from combinations of Armitage's $c_i s_{o,j}$ values (see section 5.9) and it has been assumed that the (113)/(001) and (113)/(111) vicinals lie exactly midway between the adjacent low index planes.

These equations may readily be differentiated to give:

$$\frac{d\theta}{dE} = \frac{0.5K}{(KE+1)^2} \tag{6.12}$$

for all planes except (111) which is described by;

$$\frac{d\theta}{dE} = K \tag{6.13}$$

The equations must also be recast in terms of time rather than exposure. Using equation 6.8:

$$\frac{d\theta}{dt} = \frac{Px\ 0.5}{(EK+1)^2} \tag{6.14}$$

and;

$$\frac{d\theta}{dt} = PK \tag{6.15}$$

Where P is in μtorr. Finally, equation 6.14 may be recast in terms of coverage by using equation 6.10 which expresses the relationship between exposure and coverage

for all the planes except (111).

$$\frac{d\theta}{dt} = P(0.5K-2K\theta+2K\theta^2) \qquad (6.16)$$

The values of K for the various crystal planes at 570 and 610K have been calculated from Armitage's $c_i s_{o,i}$ values which have been extrapolated to the higher temperatures using temperature dependence curves from Habraken, and these values are given in table 6.1.

From Habraken it is known that the initial sticking coefficient on the (110) plane is constant up to the temperatures studied, and it is assumed that the (113) plane (for which there is no such data) behaves similarly.

As was stated earlier, the steady state reaction is characterized by a stationary oxygen coverage brought about by the rate of adsorption of oxygen (dθ/dt) being exactly equal to it's rate of removal by CO (-dθ/dt). At this point, the dθ/dt values from equations 6.16 and 6.9 are equal in magnitude, and so we may write,

$$P_O(0.5K-2K\theta+2K\theta^2) = P_{CO}(a\theta^3+b\theta^2+c\theta+d) \qquad (6.17)$$

Where P_O denotes the oxygen partial pressure, and P_{CO}, the CO partial pressure. Rearranging, this gives an expression for the variation of coverage with R, the ratio of oxygen to CO partial pressures:

$$R = \frac{P_O}{P_{CO}} = \frac{(a\theta^3+b\theta^2+c\theta+d)}{(0.5K-2K\theta+2K\theta^2)} \qquad (6.18)$$

Similarly for the (111) face:

$$R = \frac{P_O}{P_{CO}} = \frac{(a\theta^3+b\theta^2+c\theta+d)}{K} \qquad (6.19)$$

The above equations may be solved for the stationary oxygen coverage, θ, at any desired ratio of partial pressures. Using this coverage and equations 6.15 and 6.16, the rate of reaction may thus be calculated at any CO and oxygen partial pressures. The total gas pressure must be such that the gas mixture behaves as an ideal gas, or else the rate of reaction will no longer scale linearly with gas pressure.

(6.11) Results and discussion.

Fig. 6.4 shows plots of dθ/dt vs. θ for the two temperatures 570 and 610K which have been calculated from the equations derived above. The curves 1,2 and 4 show the rate of adsorption of oxygen on the various surfaces at oxygen partial pressures of 1, 2 and 4 μtorr respectively. The curves A,B and D are similar curves for the rate of removal of chemisorbed oxygen by CO at CO pressures of 1,2 and 4×10^4 μtorr of CO. The values of dθ/dt for oxygen adsorption and CO oxidation may be readily converted into sticking probabilities, s(θ), and reaction probabilities, r(θ), respectively as:

$$s(\theta) = \frac{\text{no. of molecules sticking}}{\text{no. impinging}} \qquad (6.20)$$

and

$$r(\theta) = \frac{\text{no. of molecules reacting}}{\text{no. impinging}} \qquad (6.21)$$

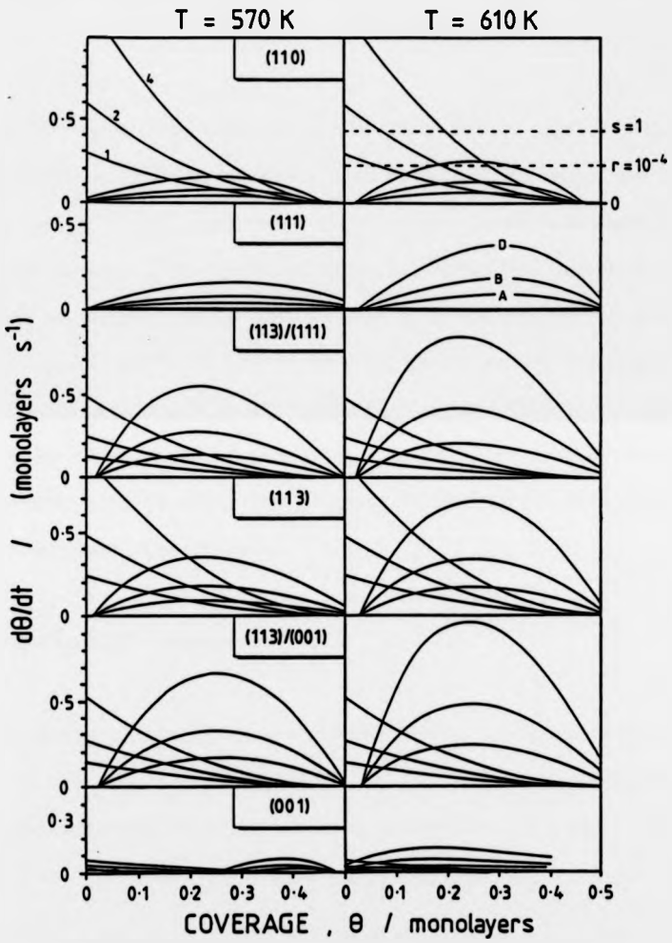

Fig. 6.4 Curves 1, 2 and 4 show the rate of oxygen adsorption as a function of coverage at oxygen partial pressures of 1, 2 and 4 µtorr respectively for the 6 faces studied at temperatures of 570 and 610K. The curves A, B and D show the rate of oxygen loss from the surfaces during reduction by CO at CO partial pressures of 1, 2 and $4x10^4$ µtorr respectively. The crossing points of the curves give the stationary surface oxygen coverage on a particular face at that particular temperature and partial pressures of CO and oxygen. The dotted lines indicate a sticking probability, s, of unity and a reaction probability, r, of 10^{-4} for an oxygen partial pressure of 1µtorr and a CO partial pressure of 10^4 µtorr (see page 151).

In order to make this conversion, the dθ/dt values must be expressed in terms of the bombardment rate in atoms/cm^2/s. This requires knowlege of the number of atoms/cm^2 on each crystal face in question. These values may be easily calculated for the low index faces and also for the vicinal surfaces although the situation is complicated by the presence of monatomic steps. The Author will, for simplicity, assume an average monolayer of about 1.5×10^{-15} atoms/cm^2 which is obtained from the average of the number of atoms/cm^2 on the three low index faces. Thus by dividing the rate of bombardment of the surface by the number of atoms/monolayer, it is possible to calculate the dθ/dt values corresponding to unity sticking coefficient or to unity reaction probability. The rate of bombardment, N, is given by:

$$N = 2.89 \times 10^{22} . p(MT)^{1/2} \text{ molecules cm}^{-2} \text{ s}^{-1} \qquad (6.22)$$

Where p is the partial pressure in torr of the gas in question, M is the molecular weight and T is the temperature in Kelvin. So, for oxygen dissociative adsorption, the dθ/dt value corresponding to unity sticking coefficient at 1 μtorr partial pressure is given by:

$$\left[\frac{d\theta}{dt}\right]_{max} = \frac{2N}{1.5 \times 10^{15}} \approx 0.3 \qquad (6.23)$$

Where the factor of 2 arises because the adsorption is dissociative. Similarly, for CO at a partial pressure of 10^4 μtorr,

$$\left[\frac{d\theta}{dt}\right]_{max} = \frac{N}{1.5x10^{15}} \approx 1.5x10^{3} \qquad (6.24)$$

It has been assumed in the above calculation that $M_O=M_{CO}=28$ and that T=590K.

The dotted lines in fig. 6.4 show unity sticking coefficient for an oxygen partial pressure of 1 μtorr and a reaction probability of $1x10^{-4}$ for a CO partial pressure of $1x10^{4}$ μtorr.

It can be seen that the maximum reaction probabilities exhibited by the three low index faces are all in the region of 10^{-5} as was previously observed by Habraken[22-25]. As stated previously, the crossing points of any of the numbered and lettered curves give the rate of reaction (dθ/dt) and oxygen coverage which will be observed at that temperature and oxygen and CO partial pressures. It can be seen from the curves, that at a constant CO partial pressure and high oxygen coverage, the various faces may be put in the same order of reactivity as was found for the CO oxidation experiments as the rate of CO oxidation is the rate determining step. ie.

(001)/(113) > (111)/(113) > (113) > (111) > (110) > (111)

rate decreasing →

The same order of reaction applies at both temperatures. Obviously, at very low oxygen partial pressures the dissociative chemisorption of oxygen will become rate limiting rather than the rate of removal of oxygen by CO.

Fig. 6.5 shows the rate of reaction plotted as a function of orientation for both temperatures, for ratios of O:CO ranging from $16:1x10^{4}$ to $1:8x10^{4}$ at a constant total pressure of 10^{4} μtorr (0.01 torr). It is immediately obvious from these ratios, that:

(a) CO must be in great excess for the reaction to proceed at any appreciable rate.

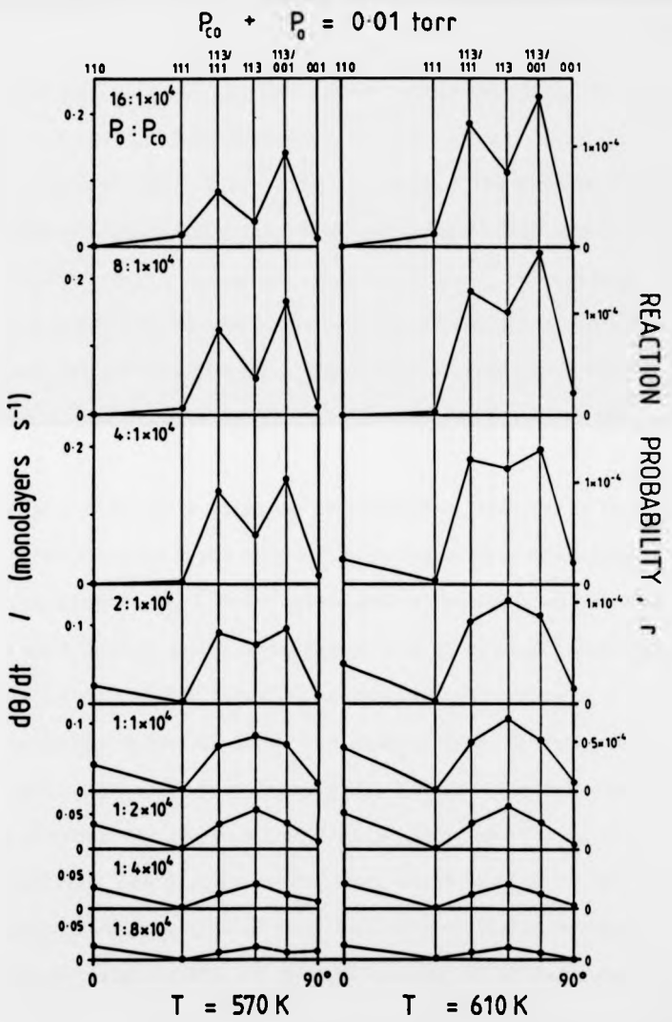

Fig. 6.5 This figure shows the rate of reaction and the reaction probability in the CO oxidation reaction as a function of crystallographic orientation for O_2:CO ratios ranging from 16:1x10^4 to 1:8x10^4 at a constant total gas pressure of 1x10^4 µtorr. These data have been obtained from the intersections of curves such as those shown in fig. 6.4 which describe the kinetics of oxygen loss and uptake by the surface, and have been normalized to a total gas pressure of 1x10^4 µtorr.

(b) The oxygen to CO ratio must be controlled rather carefully as the rate of reaction depends strongly on this parameter.

It can also be seen from this figure that whilst near the optimum O:CO ratios the faces exhibit the order of reactivity given above, at other ratios, the relative reactivities of the faces change. This is not at all surprising, as at ratios other than the optimum ratio the rate of oxygen dissociation begins to affect the overall rate of reaction. Indeed, at the lowest oxygen partial pressures, the faces may be put in roughly the same order of reactivity to CO oxidation as their order of reactivity to oxygen chemisorption (section 5.10).

Unfortunately, at these extremes of behaviour, the fits to the experimental data exhibit their greatest errors, and so it is impossible to be precise. Indeed, the only regime acessible to this model is that very regime where the O:CO ratio is such that the faces exhibit what is close to their maximum reactivity at a given total pressure.

It should be noted that for (001) at both temperatures the two sets of curves cross at the extremes of the CO data, and so the rates of reaction given in fig. 6.5 for this face are necessarily very inaccurate. Also, in fig. 6.5, the ratio of gases is never close to optimum for the reaction on the (111) face due to it's low reactivity to oxygen chemisorption. The oxygen to CO ratio would have to be increased by at least an order of magnitude in order for this face to express it's maximum reaction rate.

The reaction rates in fig. 6.5 will, of course, all scale linearly with total gas pressure until the pressure is such that the gas no longer behaves in an ideal manner.

Finally, fig. 6.6 shows the variation in the ratio, R, of O_2:CO partial pressures with surface coverage. As expected, for oxygen depleted mixtures (low values of R) the oxygen coverage is low , whilst for oxygen rich gas mixtures (high R values), the oxygen coverage is high.

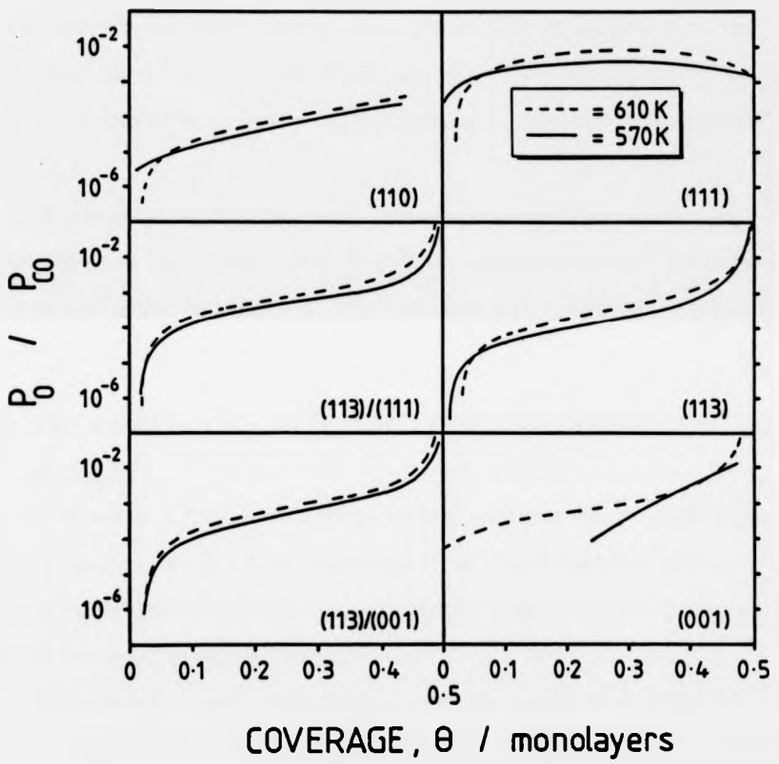

Fig. 6.6 This figure shows the vatiation in R, the ratio of O_2:CO partial pressures, with surface coveargе. These data have been calculated from equations 6.18 and 6.19. If these curves are used in conjunction with equations 6.15 and 6.16, then it is possible to calculate the rate of the 'steady state' reaction at either temperature and for any total gas pressure (within the constraints of ideal gas theory) and composition of reaction gas.

It can also be seen from the figure that at a given pressure ratio, the surface oxygen coverage is always less at 610K than at 570K by a significant amount. This clearly shows that the reaction probability for CO oxidation increases more quickly with temperature than the sticking probability of oxygen over the temperature range 570 to 610K.

By using these curves in conjunction with equations 6.15 and 6.16, it is possible to calculate the rate of the 'steady state' reaction at either temperature and for any pressure and any composition of reaction gas within the constraints of the ideal gas theory.

(6.12) The oxidation of hydrogen by oxygen chemisorbed on copper surfaces.

In chapter 5, the oxidation of copper surfaces was studied using two different oxidizing agents, O_2 and N_2O, whose reactivities were compared and contrasted. Similarly, in this chapter, the reduction of chemisorbed oxygen films on copper surfaces is studied using two different reducing agents, CO and H_2.

The oxidation of hydrogen by oxygen chemisorbed on well defined copper planes has, to the Author's knowledge, been the subject of only one previous investigation[29]. There has, however, been quite a lot of work done on the interaction of hydrogen with clean copper surfaces, and the results of this work, and the previous investigation into hydrogen oxidation, will now be summarized.

(6.13) Hydrogen adsorption on copper surfaces.

Hydrogen adsorbs dissociatively on metal surfaces and on most metals this is a fast process which is not observably activated. On copper however, the adsorption of hydrogen has been found to be activated (Balooch et al[30], Hayward and Trapnell[31], and

Alexander and Pritchard[32]) with an apparent activation energy of between 1 to 2 $kJmol^{-1}$.

The initial sticking factor is about 10^{-2} at room temperature, and according to Balooch et al[30], it is dependent on crystallographic orientation. A crystallographic dependence is also observed in the desorption kinetics (Balooch and Stickney[33]). Balooch et al have found in a molecular beam study of the dissociative adsorption of hydrogen on copper (110), (100) and (310), that the ledge sites and other surface defects are not the principle sites for H_2 dissociation[30]. This conclusion was reached as the (100) and the stepped (310) surface (which has fully kinked steps and (100) terraces) behaved similarly in the molecular beam experiments. This is to be contrasted with hydrogen adsorption on platinum surfaces where Bernasek et al[34] have found good evidence that the process is activated on (111) terraces, but not on the steps found on (111) vicinals. Indeed, steps were found to be necessary for any hydrogen adsorption at all to occur on Pt(111) at room temperature.

(6.14) The oxidation of hydrogen by oxygen chemisorbed on Cu(110).

Hachicha et al[29] have investigated the reaction between hydrogen and adsorbed oxygen on Cu(110) in the temperature range 625 to 800K and H_2 partial pressures of about 10^{-4} torr.

At temperatures less than 500K, the rate of reaction was reported to be immeasurably small, even at H_2 partial pressures as high as 10^{-3} torr. The oxygen overlayers initially corresponded to either the (2x1) (θ=0.5) or the c(6x2) structures, and Hachicha et al state that the reduction sequence was found to be independent of the the overlayer and the temperature at which it was formed.

The activation energy for the reaction was found to be 82$kJmol^{-1}$ and the reaction was found to be first order in hydrogen pressure at temperatures below 650K. At higher

Alexander and Pritchard[32] with an apparent activation energy of between 1 to 2 $kJmol^{-1}$.

The initial sticking factor is about 10^{-2} at room temperature, and according to Balooch et al[30], it is dependent on crystallographic orientation. A crystallographic dependence is also observed in the desorption kinetics (Balooch and Stickney[33]). Balooch et al have found in a molecular beam study of the dissociative adsorption of hydrogen on copper (110), (100) and (310), that the ledge sites and other surface defects are not the principle sites for H_2 dissociation[30]. This conclusion was reached as the (100) and the stepped (310) surface (which has fully kinked steps and (100) terraces) behaved similarly in the molecular beam experiments. This is to be contrasted with hydrogen adsorption on platinum surfaces where Bernasek et al[34] have found good evidence that the process is activated on (111) terraces, but not on the steps found on (111) vicinals. Indeed, steps were found to be necessary for any hydrogen adsorption at all to occur on Pt(111) at room temperature.

(6.14) The oxidation of hydrogen by oxygen chemisorbed on Cu(110).

Hachicha et al[29] have investigated the reaction between hydrogen and adsorbed oxygen on Cu(110) in the temperature range 625 to 800K and H_2 partial pressures of about 10^{-4} torr.

At temperatures less than 500K, the rate of reaction was reported to be immeasurably small, even at H_2 partial pressures as high as 10^{-3} torr. The oxygen overlayers initially corresponded to either the (2x1) (θ=0.5) or the c(6x2) structures, and Hachicha et al state that the reduction sequence was found to be independent of the the overlayer and the temperature at which it was formed.

The activation energy for the reaction was found to be $82kJmol^{-1}$ and the reaction was found to be first order in hydrogen pressure at temperatures below 650K. At higher

temperatures, the order in hydrogen pressure was found to be 0.8 to 0.9. It was found that the maximum reaction probability was in the range 10^{-7} to 10^{-5} over the temperature range 500-800K. Hachicha et al suggest that the reaction follows a Langmuir-Hinshelwood scheme which may be written as below:

(1) $O_{ad} + H_2(g) \rightleftharpoons O(ad) + 2H(ad)$

(2) $O(ad) + H(ad) \rightleftharpoons OH(ad)$

(3) $OH(ad) + H(ad) \rightleftharpoons H_2O\uparrow$ (6.25)

Hachicha suggests that the rate determining step is step 2, the reaction of adsorbed hydrogen atoms with adsorbed oxygen atoms.

(6.15) The oxidation of hydrogen by oxygen chemisorbed on copper surfaces: Experimental procedure.

The experimental procedure for the oxidation of hydrogen by chemisorbed oxygen films on the copper cylinder was essentially identical to that used for the CO oxidation experiments described in section 6.8. The cylinder was first cleaned by the usual method of argon ion bombardment and annealing, and then saturated with oxygen to an isotropic coverage corresponding to approximately 0.5 monolayers of oxygen. The oxygen coverage on the various crystal planes was recorded by measuring oxygen and copper peak-to-peak heights at 5° intervals around the sample circumference. The crystal was then heated to the reaction temperature (570 or 630K), and subjected to increasing exposures to hydrogen at a partial pressure of about 10^{-5} torr whilst being rotated.

After each exposure, the anisotropy in the surface oxygen coverage around the sample circumference was re-recorded. The resulting data were normalized to a saturation coverage of 0.5 monolayers of oxygen as described previously (section 6.8).

(6.16) Results and discussion.

Fig. 6.7 shows the anisotropy in the oxygen coverage recorded at 5° intervals of arc around the sample circumference at the two temperatures 570 and 630K, after H_2 exposures ranging from 6000 to 72000L.

These data may be profitably compared with the data of fig. 6.1a and b, which are data collected at similar temperatures with CO as the reducing gas.

Considering fig. 6.7, it can be seen that the oxygen coverage, which is initially isotropic, begins to show marked anisotropies after an exposure of about 36000L at both temperatures. Also, it can be seen that the data at the higher temperature (630K) show a significantly greater crystallographic anisotropy than do the data taken at 570K. At both temperatures, however, the reaction is seen to be rather less crystallographically dependent than is observed to be the case for the oxidation of CO by adsorbed oxygen.

As was found to be the case in the CO oxidation experiments, the data begin to develop minima (indicative of a high rate of reaction) on (113) vicinals roughly midway between (113) and (001), and between (113) and (111), at both temperatures. Considering the data from 48000L to 72000L at 570K, there is evidence for a special reactivity associated with (110) vicinals midway between (110) and (111) as minima in the data are seen to occur here also. This is in marked contrast to the CO oxidation data, where the (110) vicinals were not observed to be especially reactive. It is not clear from the data whether this special reactivity of (110) vicinals is manifest at the higher temperature however.

Fig. 6.8 shows kinetic data extracted from the anisotropy data at the two temperatures. Again, the coverage of a particular face at a given exposure is taken as the average coverage of all similar faces in order to take advantage of the redundancy in the data. From these plots it can be seen that the reaction follows Langmuir-Hinshelwood

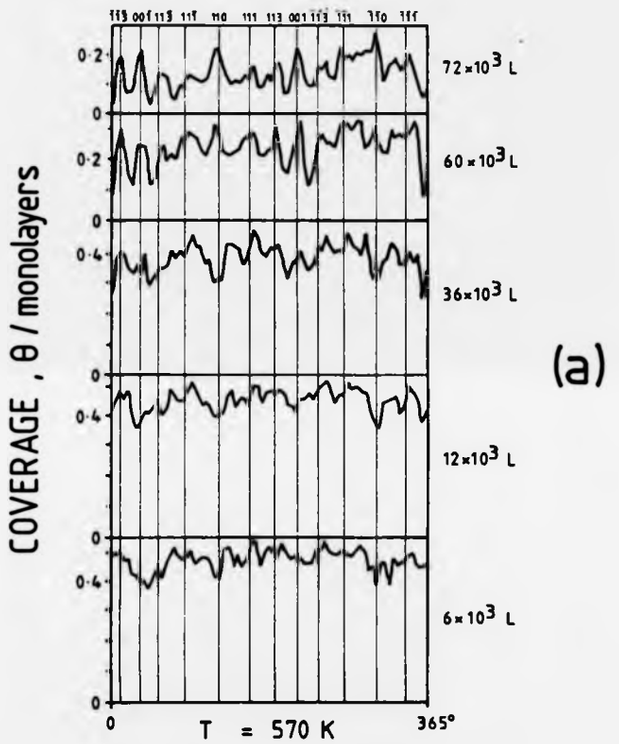

Fig. 6.7 This figure shows the anisotropy in the oxygen coverage recorded at 5° intervals of arc around the sample circumference at the two temperatures 570 and 630K, after H_2 exposures ranging from 6000L to 72000L. Fig 6.7a shows the data recorded at 570K and fig. 6.7b shows the data recorded at 630K. These data should be compared with the data of fig. 6.1a and b which are data collected at similar temperatures with CO as the reducing gas.

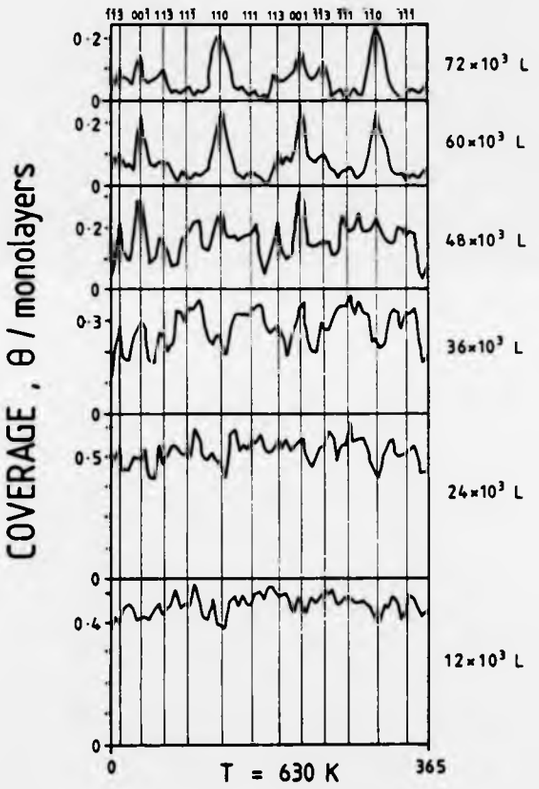
113 001 113 111 110 111 113 001 113 111 110 111
0·2
0
72×10³ L
0·2
0
60×10³ L
0·2
0
48×10³ L
0·3
0
36×10³ L
0·5
0
24×10³ L
0·4
0
12×10³ L
COVERAGE , θ / monolayers
0
T = 630 K
365

(b)

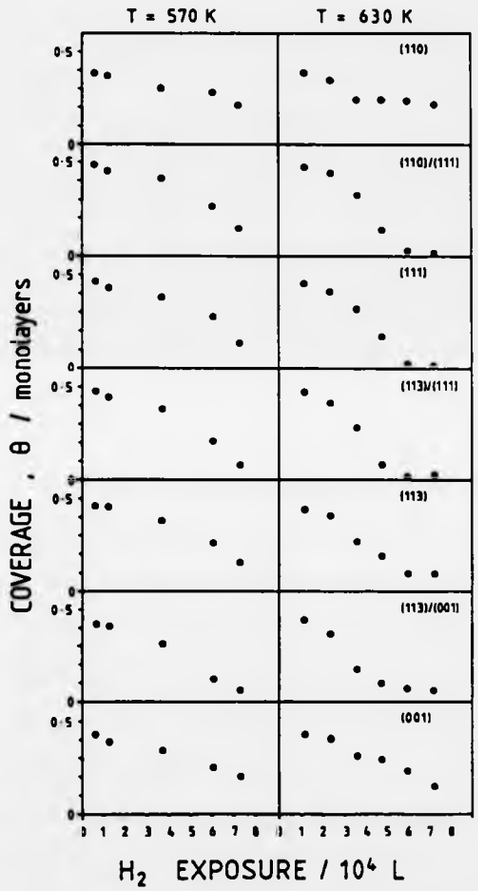

Fig. 6.8 This figure shows kinetic data extracted from the anisotropy data of fig. 6.7 at the two temperatures 570 and 630K. The coverage of a particular face at a given exposure is taken as the average coverage of all similar faces in order to take advantage of the redundancy in the data.

kinetics on all faces investigated. It can also be seen that the rate of reaction increases on raising the temperature from 570 to 630K, and that at the higher temperature the faces may be put in the following order of reactiviy:

$$(113)/(001) \approx (113)/(111) > (110)/(111) > (111) \approx (113) > (001) \approx (110)$$

This ordering is very similar to that found in the CO oxidation experiments, and once again, it is the (113) vicinals which exhibit the highest reactivity.

At 570K, the observed anisotropy is rather lower, and there is no clear ordering of the faces except that the (113) vicinals seem to be significantly more reactive than the other faces.

In section 6.9, a simple geometrical argument was used to explain the special reactivity of (113) vicinals and (113) itself to reduction by CO. Essentially, it was proposed that the chemisorbed oxygen atoms sat at the bottom of the steps in high coordination sites, and adsorbed CO approached from the top of the steps in exactly the right geometry to react and form the linear CO_2 molecule. Given these assumptions, only faces with an intermediate ridge density will be capable of accommodating this geometry, and hence the special reactivity of (113) and its vicinals.

It is thought that the rate determining step in the H_2 oxidation reaction is the formation of OH_{ad} from O_{ad} and H_{ad} (Hachicha et al[29]). If this is indeed the case, then it is not clear in what way this step could express any particularly stringent steric requirements, and indeed, this may well be the reason that the oxidation of hydrogen by oxygen chemisorbed on copper surfaces is relatively structurally insensitive. However, as the OH_{ad} species is probably linear and bonded via the oxygen atom to the surface, any transition state where the adsorbed hydrogen atoms approach adsorbed oxygen atoms from above has the greatest similarity to the final state species, and may, perhaps, be

expected to exhibit a slightly lower energy.

It can be seen then, that our previous geometric arguments may also be applicable to this reaction except that in this case the effect is obviously much smaller. If, on the other hand, the rate determining step is the formation of H_2O from OH(ad) and H(ad), then our geometric arguments are inadequate as in this latter case approach of H(ad) from the side would probably be a more energetically favourable situation than would approach from above, and the low index atomically smooth surfaces might be expected to exhibit the highest reactivity. Clearly, in order to understand this reaction more fully, much more information is needed about the mechanism of each stage of the reaction and also about the structure of the various intermediates.

Chapter 6..... References

(1) Pritchard J., *J. Vac. Sci. Technol.* 9 (1972) p.895.

(2) Conrad H., Ertl G., Kuppers J., Latta E.F., *Solid State Comm.* 17 (1975) p.613.

(3) Kessler J., Thieme F., *Surf. Sci.* 67 (1977) p.405.

(4) Andersson S., *Surf. Sci.* 89 (1979) p.477-485.

(5) Andersson S., Pendry J.B., *J. Phys. C: Solid State Phys.* 13 (1980) p.3547-61.

(6) Chesters M.A., Pritchard J., *Surf. Sci.* 28 (1971) p.460.

(7) Tracy J.C., *J. Chem. Phys.* 56 (1972) p.2748.

(8) Pritchard J., *Surf. Sci.* 79 (1979) p.231.

(9) Lindgren S.A., Paul J., Wallden L., *Chem. Phys. Lett.* 84 no.3.

(10) Woodruff D.P., Bradshaw A.M., *Surf. Sci.* 123 (1982) p.397-412.

(11) Horn K., Hussain M., Pritchard J., *Surf. Sci.* 63 (1977) p.244.

(12) Blyholder G., *J. Phys. Chem.* 68 (1964) p.2772.

(13) Mc.Conville C.F., Somerton C., Woodruff D.P., *Surf. Sci.* 139 (1984) p.75-86.

(14) Hollins P., Pritchard J., *Surf. Sci.* 134 (1983) 91-108.

(15) Boulliard J.C., Cohen C., Domange J.L., Drigo A.V., L'Hoir A., Moulin J., Sotto M., *Phys. Rev. B* 30 no.5 (1984) p.2740-2486.

(16) Lapujoulade J., Perreau J., Kara A., *Surf. Sci.* 129 (1983) p.59-78.

(17) Jones H.A., Taylor H.S., *J. Phys. Chem.* 27 (1923) p.623.

(18) Garner W.E., Stone F.S., Tiley P.F., *Proc. Royal Soc.* (London) A221 (1952) p.472.

(19) Smith A.W., *J. Catalysis* 4 (1965) p.172.

(20) van der Meijden J., Ph.d Thesis, University of Utrecht. (1980).

(21) Ertl G., *Surf. Sci.* 7 (1967) p.309.

(22) Habraken F.P.H.M., Keiffer E.Ph., Bootsma G.A., *Surf. Sci.* 83 (1979) p.45.

(23) Habraken F.P.H.M., Bootsma G.A., *Surf. Sci.* 87 (1979) p.333.

(24) Habraken F.P.H.M., Bootsma G.A., Hofman P., Hachicha S., Bradshaw A.M., *Surf. Sci.* 88 (1979) p.285.

(25) Habraken F.P.H.M., Ph.D. thesis, Rijksuniversitest, Utrecht, 1980.

(26) Norton P.R., Chapter 2, "The Chemical Physics of Solid Surfaces and Heterogeneous Catalysis vol.4", King D.A. and Woodruff D.P. Editors, Elsevier Amsterdam-Oxford-New York (1982).

(27) Armitage A.F., Ph.D. Thesis, The University of Warwick (1982).

(28) Prutton M., "Surface Physics", Clarendon Press Oxford (1975).

(29) Hachicha S., Hofmann P., Bradshaw A.M., "Proceedings of the 4th. International Conference on Solid Surfacs and the 3rd. European Conference on Surface Science vol.1" p.645, Cannes (1980).

(30) Balooch M., Cardillo M.J., Miller D.R., Stickney R.E., *Surf. Sci.* 46 (1974) p.358-392.

(31) Hayward D.O., Trapnell B.M.W., "Chemisorption", Butterworths, London (1964) p.75.

(32) Alexander C.S., Pritchard J., *J. Chem. Soc. Faraday Trans.* 68 (1972) p.202.

(33) Balooch M., Stickney R.E., *Surf. Sci.* 44 (1974) p.310.

(34) Bernasek S.L., Seikhaus W.J., Somorjai G.A., *Phys. Rev. Lett.* 30 (1973) p.1202.

Chapter 7

FINAL CONCLUSIONS AND FURTHER WORK

Chapter 7 ..... Contents

(7.1) Final Conclusions.

(7.2) Further work.

(7.1) Final Conclusions.

(a) Auger electron spectroscopy on cylindrical single crystals has been shown to provide an extremely sensitive probe for crystallographic differences in the reactivity of copper and nickel surfaces. The technique has been shown to facilitate the detailed investigation and comparison of many different crystal planes.

(b) Both carbon and sulphur segregation to nickel surfaces have been shown in chapter 4 to exhibit significant anisotropy in heats of segregation which may be correlated with surface crystallography. In particular, the equilibrium segregation of sulpur to nickel surfaces has been shown to occur with a heat of segregation which is approximately linearly dependent on the step density. Clear evidence has been found for the inhibition of carbon segregation by sulphur, which suggests site competition between the two species.

(c) In chapter 5, the reaction of oxygen and nitrous oxide with the copper cylinder has been studied and whilst the initial sticking coefficient seems to be linearly dependent on step density in the case of oxygen adsorption, in the case of N2O decomposition, an exponential dependence on step density is found to be more appropriate. Both sets of data show clear evidence for surface diffusion of oxygen on crystal planes between (110) and (113) at coverages approaching 0.5 monolayers. There is also some tentative evidence for surface diffusion on planes between (113) and (001). The two models proposed by Armitage which describe the adsorption kinetics of the cylindrical single crystal surface have been re-evaluated, and it is clear that the 'fast diffusion' model is the most accurate.

(d) In chapter 6, the reduction of chemisorbed oxygen films on copper surfaces was investigated using CO and hydrogen as reducing agents. In the case of the CO oxidations, the reaction was found to require a surface consisting of both steps

and terraces for a high reaction rate. Steps of a type found on (113) vicinals (but not on (110) vicinals) were found to be required for the highest rates of reaction. To the Author's knowledge, this is the first time that both steps *and* terraces have been found to be required for an enhanced reaction rate. A theoretical description of the steady state reaction between an oxygen/CO gas mixture and copper single crystal planes was also presented, and this allowed the calculation of the steady state oxygen coverage and rate of reaction on any crystal plane in the [1$\bar{1}$0] zone at arbitrary CO and oxygen partial pressures. Hydrogen oxidation has also been investigated, and this reaction was found to be much less crystallographically dependent than the CO oxidation reaction. A simple geometrical argument was proposed to explain the necessity of both steps and terraces in the CO and hydrogen oxidation reactions.

(7.2) Further work.

In principle, any system which exhibits crystallographically dependent adsorption or segregation properties may be investigated using AES and cylindrical single crystals. Also, many of the other techniques of surface science may be readily applied to cylindrical samples, in particular LEED, RHEED and photoemission. Such work would doubtless increase the understanding of the relationship between surface defects and the reactivity of surfaces.

The Author would like to take this opportunity to present some preliminary data on the interaction of chloroform with copper surfaces. Fig. 7.1 shows the chlorine peak-to-peak heights recorded around the sample circumference at 5° intervals of arc for 4 chloroform exposures of approximately 0.3, 0.6, 1.5 and 12L. As previously described for the oxygen data, the peak-to-peak heights have been normalized to the orientational

and terraces for a high reaction rate. Steps of a type found on (113) vicinals (but not on (110) vicinals) were found to be required for the highest rates of reaction. To the Author's knowledge, this is the first time that both steps *and* terraces have been found to be required for an enhanced reaction rate. A theoretical description of the steady state reaction between an oxygen/CO gas mixture and copper single crystal planes was also presented, and this allowed the calculation of the steady state oxygen coverage and rate of reaction on any crystal plane in the [1$\bar{1}$0] zone at arbitrary CO and oxygen partial pressures. Hydrogen oxidation has also been investigated, and this reaction was found to be much less crystallographically dependent than the CO oxidation reaction. A simple geometrical argument was proposed to explain the necessity of both steps and terraces in the CO and hydrogen oxidation reactions.

(7.2) Further work.

In principle, any system which exhibits crystallographically dependent adsorption or segregation properties may be investigated using AES and cylindrical single crystals. Also, many of the other techniques of surface science may be readily applied to cylindrical samples, in particular LEED, RHEED and photoemission. Such work would doubtless increase the understanding of the relationship between surface defects and the reactivity of surfaces.

The Author would like to take this opportunity to present some preliminary data on the interaction of chloroform with copper surfaces. Fig. 7.1 shows the chlorine peak-to-peak heights recorded around the sample circumference at 5° intervals of arc for 4 chloroform exposures of approximately 0.3, 0.6, 1.5 and 12L. As previously described for the oxygen data, the peak-to-peak heights have been normalized to the orientational

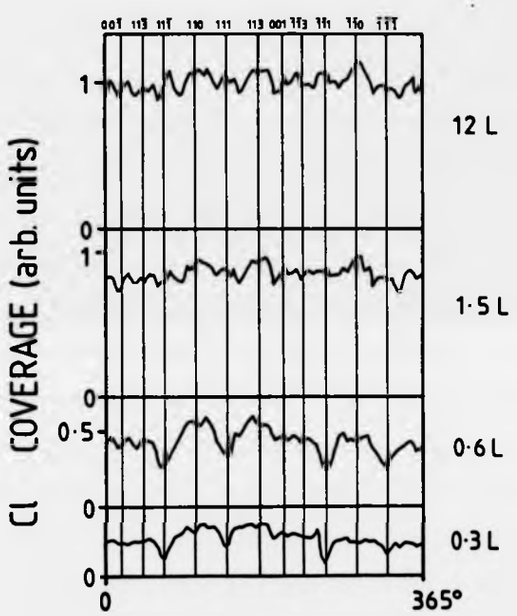

Fig. 7.1 This figure shows the variation in chlorine coverage around the circumference of the <i1i0> axis cylinder as a function of chloroform exposure. The Cl(181eV) peak-to-peak heights have been recorded around the sample circumference at 5° intervals of arc and then normalized to the orientational average of the similarly recorded Cu(920eV) peak-to-peak heights. The assumption is made that this parameter is proportional to the surface chlorine coverage.

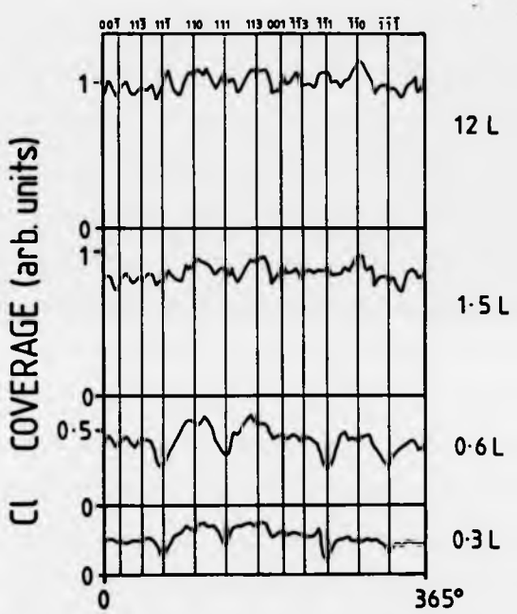

Fig. 7.1 This figure shows the variation in chlorine coverage around the circumference of the <i10> axis cylinder as a function of chloroform exposure. The Cl(181eV) peak-to-peak heights have been recorded around the sample circumference at 5° intervals of arc and then normalized to the orientational average of the similarly recorded Cu(920eV) peak-to-peak heights. The assumption is made that this parameter is proportional to the surface chlorine coverage.

average of the Cu(920) peak similarly recorded. Baetzold[1] has also studied this reaction on two (111) vicinals, Cu[2x(111)x(100)] and Cu[(5x(111)x(100)]. The Author finds in common with Baetzold that the rate of chlorine adsorption from the dissociation of $CHCl_3$ on the surface is indeed approximately linearly dependent on step density for vicinals close to (111). Also, no carbon could be detected in the Auger spectrum of the surface.

The data of fig. 7.1 have several interesting features. Firstly, it can be seen that the reaction exhibits a noticeable anisotropy at coverages less than about 1.5L (which corresponds to saturation). The (111) planes exhibit the lowest reactivity with all other planes being similarly reactive and there is no clear correlation between surface reactivity and step density. The surface coverage rises quite sharply on either side of a (111) plane and then remains essentially constant. This feature of the data is in sharp contrast to all other data collected on the copper cylinder where the observed anisotropy could always be correlated in some way with step density. In particular, the data are essentially isotropic between (113) and (001). This may possibly be due to adsorbate induced faceting in the region of (001). Also, it can be seen that the (110), (111) and (113) planes are significantly more reactive at exposures less than 1.5L than their counterparts $(\bar{1}\bar{1}0)$, $(\bar{1}\bar{1}1)$ and $(\bar{1}\bar{1}3)$. This is the first time that such an inequivalence has been observed on the cylindrical copper crystal. The feature was completely reproducible and suggests that in some way one side of the sample is significantly different from the other.

It is not clear what the cause of this difference is. Very small impurity levels, undetectable by AES, may be the cause, but this would seem to be unlikely as the effect is manifest as a single smooth oscillation in the Auger intensities and there seems to be no reason why random impurities should vary in such a regular manner. The fact that the oscillation is not present in the saturation data and in subsequent oxygen adsorption data effectively rules out an artefact due to eccentricity in sample rotation.

The Author feels that this effect may well be crystallographic in origin. As stated in chapter 3, the samples used in the current work were not perfectly cylindrical but had a very slight taper. This slight misorientation may well give rise to an appreciable density of kinks on one side of the sample but not on the other, and it is possible that the increased reactivity of one side of the sample could be due to the presence of kinks in the steps.

The above experiment immediately suggests three avenues for further research on the copper cylindrical single crystal.

(a) The complex relationship between step density and reactivity which has been found for chloroform adsorption on copper should be investigated and surface structural information obtained to see if the phenomenon may be correlated with adsorbate induced faceting.

(b) The kinetics of the reaction should be studied as in the previous oxygen adsorption experiments.

(c) The effect of kinks on chloroform adsorption on copper should be investigated.

Experiment *(c)* should be particularly stressed as it would entail the preparation of a cylindrical sample with surface orientations in a different zone of the stereographic triangle. All of the experiments conducted in this investigation could profitably be repeated on fully kinked surfaces and shaped surfaces where the kink density, rather than the step density, is the variable. A technique of surface crystallography would be mandatory for any investigations outside of the <110> zone however, as it is known that kinked copper surfaces have a tendency to facet under oxygen adsorption.

Chapter 7 ..... References

(1) Baetzold R.C., *Surf. Sci.*, 95 no.1 (1980) p.286.

APPENDIX

In surface physics and chemistry two units are still in common usage which are not S.I. units: The torr and the Langmuir.

For the reader's convenience, these units are now defined, and conversion factors are given to the appropriate S.I. units.

The torr

The torr is the commonly used unit of pressure in surface science.

$$1 \text{ torr} = 133.322 \text{ Pa}$$

$$1 \text{ Pa} = 1 \text{ Nm}^{-2}$$

The Langmuir

The Langmuir (L) is still the most commonly used unit of exposure in surface science. One Langmuir corresponds to an exposure to a partial pressure 10^{-6}torr of a given gas for 1 second.

$$1 \text{ L} = 10^{-6} \text{ torr s}^{-1} = 133.322 \times 10^{-6} \text{ Pa s}^{-1}$$